Flexible Electronics and Display Technology for Medical, Biological, and Life Science Applications

by

Joseph T. Smith

A Dissertation Presented in Partial Fulfillment
of the Requirements for the Degree
Doctor of Philosophy

Approved August 2014 by the
Graduate Supervisory Committee:

David Allee, Chair
Michael Goryll
Michael Kozicki
Jennifer Blain Christen
Aaron Couture

ARIZONA STATE UNIVERSITY

December 2014

ABSTRACT

This work explores how flexible electronics and display technology can be applied to develop new biomedical devices for medical, biological, and life science applications. It demonstrates how new biomedical devices can be manufactured by only modifying or personalizing the upper layers of a conventional thin film transistor (TFT) display process. This personalization was applied first to develop and demonstrate the world's largest flexible digital x-ray detector for medical and industrial imaging, and the world's first flexible ISFET pH biosensor using TFT technology. These new, flexible, digital x-ray detectors are more durable than conventional glass substrate x-ray detectors, and also can conform to the surface of the object being imaged. The new flexible ISFET pH biosensors are >10X less expensive to manufacture than comparable CMOS-based ISFETs and provide a sensing area that is orders of magnitude larger than CMOS-based ISFETs. This allows for easier integration with area intensive chemical and biological recognition material as well as allow for a larger number of unique recognition sites for low cost multiple disease and pathogen detection.

The flexible x-ray detector technology was then extended to demonstrate the viability of a new technique to seamlessly combine multiple smaller flexible x-ray detectors into a single very large, ultimately human sized, composite x-ray detector for new medical imaging applications such as single-exposure, low-dose, full-body digital radiography. Also explored, is a new approach to increase the sensitivity of digital x-ray detectors by selectively disabling rows in the active matrix array that are not part of the imaged region. It was then shown how high-resolution, flexible, organic light-emitting

diode display (OLED) technology can be used to selectively stimulate and/or silence small groups of neurons on the cortical surface or within the deep brain as a potential new tool to diagnose and treat, as well as understand, neurological diseases and conditions. This work also explored the viability of a new miniaturized high sensitivity fluorescence measurement-based lab-on-a-chip optical biosensor using OLED display and a-Si:H PiN photodiode active matrix array technology for point-of-care diagnosis of multiple disease or pathogen biomarkers in a low cost disposable configuration.

This dissertation is dedicated to the memory of my father,

John H. Smith

1933 – 1992

Who taught me the difference between the dumb and smart end of a hammer

ACKNOWLEDGMENTS

I wish to thank my advisor, Dr. David Allee, for his continued support, guidance, and patience putting up with such an obstinate student. I also would like to thank my committee members, starting with Dr. Michael Goryll for his help, which went above and beyond the call of duty; Dr. Jennifer Blain Christen for convincing an electrical engineer that he might be able to understand a little neuroscience and biochemistry; Dr. Aaron Couture of GE Global Research for answering my many questions and tactfully pointing out my (many) mistakes, as well as his invaluable support and guidance; and Dr. Michael Kozicki, for giving me the confidence to get started on this adventure. I especially want to thank John Stowell for his exceptional support building many of the prototypes. Special thanks to Dr. Ed Bawolek for his expert test-apparatus advice, and to Michael Marrs for his technical help, and especially for figuring out how to make thin-film devices that always seem to work right the first time. Of course, special thanks go to the rest of process engineering, manufacturing, and management team at the ASU Flexible Electronics and Display Center for the development and fabrication of the prototypes, and also for providing me with the opportunity to work there. I also would like to thank the Army Research Labs for sponsoring this work, Dr. Harvey Nathanson for bringing out the inventor hidden inside of me, and Dr. Dimitris Ioannou for originally inspiring me to get started on this journey long ago.

Finally, I thank my wife, MaryEllen Smith, who was the first to encourage me to move out of my comfort zone and look into new biomedical applications for flex technology. Plus, she's always been there for me – no matter what.

TABLE OF CONTENTS

CHAPTER Page

CHAPTER Page

LIST OF FIGURES

Figure Page

Figure Page

Figure Page

Figure Page

Figure Page

Figure Page

Figure Page

CHAPTER 1

INTRODUCTION

Flex electronics is a revolution, following in line with previous electronics industry innovations. It is a disruptive technology that will create, change and disturb markets.

Dr. Jennifer Ricklin, Chief Technologist, US Air Force Research Laboratory

Flexible electronics has been identified as one of the "emerging technologies that will change the world" (2013c). Flexibility adds value by offering lighter weight and improved durability, plus the ability to offer new, unusual, and improved form factors and functionality.

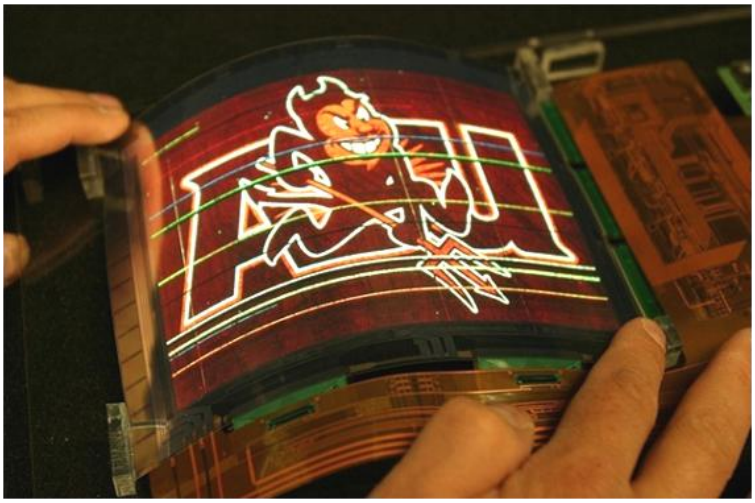

Figure 1. Flexible 7.4″ diagonal color organic light emitting diode (OLED) display for mobile applications developed and manufactured at the ASU Flexible Electronics and Display Center.

The added functionality from flexibility has the potential to disrupt much of the established brittle electronics industry, which is currently dominated by rigid printed circuit boards, fragile glass display substrates, and silicon wafers, as well as establish new

markets and industries in unexpected and unknown ways (Nathan et al. 2012). For example, flexible displays for mobile applications (Figure 1) are one rapidly emerging flexible electronics technology, which is expected to grow rapidly after 2015 and projected to account for up to 19% of all displays sold in 2020 (2013f).

Research Objective and Report Outline

Given these potential benefits, the objective of this research effort was to explore how flexible electronics and display technology can be applied to develop new and exciting applications for medical, biological and life science applications. Chapter 2 describes how flexible display technology was applied to make digital x-ray detectors for medical and industrial imaging more durable, as well as conformable. Chapter 3 describes how the flexible x-ray detectors from Chapter 2 can be tiled to create a single very large—ultimately human sized—x-ray detector. This new flexible x-ray tiling approach is designed to enable new medical and industrial imaging applications currently not possible using existing glass-substrate digital x-ray detectors. Chapter 4 presents a new approach to increase the sensitivity of digital x-ray detectors by reducing background noise. This technique was discovered during an investigation of the noise properties of the thin film transistors (TFTs) used in the flexible x-ray detectors described in Chapter 2. Chapter 5 demonstrates how flexible display technology was applied to manufacture the world's first flexible ISFET biosensor on a plastic substrate. These new flexible plastic ISFET biosensors are expected to be useful in diagnostic applications where low-cost, disposability, shatter resistance, and/or a large biosensing array area is valued. Chapter 6 presents a new biophotonic application for high-resolution, flexible,

organic, light-emitting-diode (OLED) display technology—to selectively stimulate and/or silence small groups of neurons on the cortical surface or within the deep brain. This new integration of flexible OLED display technology with human biological systems is designed to offer a viable future avenue for chronic *in vivo* implantation of the latest optogenetics therapies, which could lead to treatments for epilepsy, stroke, seizures, paralysis, depression, schizophrenia, Parkinson's disease, and/or Alzheimer's disease. Chapter 7 explores the viability of a new miniaturized fluorescence measurement-based lab-on-a-chip concept using OLED display and hydrogenated amorphous-silicon (a-Si:H) photodiode active matrix array technology point-of-care diagnosis of multiple disease or pathogen markers in a low cost disposable configuration. Conclusions and recommendations for future flexible electronics research follow in Chapter 8.

However, before discussing the above new biomedical applications for flex technology, a brief technical background on TFT-based flexible electronics and display technology is provided. The flex technology overview is followed by a short review of recent, related biomedical research – also using flexible substrates. Additional flexible electronics research as it relates specifically to the material in each of the chapters is included as technical background in each chapter.

Thin Film Transistor (TFT) Technology

At a fundamental level, the flexible electronics technology used for this research is essentially a flexible and thin transparent sheet of plastic, similar in look and feel to overhead transparency film, covered with a thin layer of extremely tiny on/off switches. The tiny on/off switches are called thin film transistors or TFTs, and are similar in size to

the diameter of a human hair. The TFTs are constructed using a combination of layering and patterning of thin films on the flexible plastic substrate—hence the term "thin-film transistor." An example of these patterned thin film layers is illustrated in the TFT cross-section in Figure 2. Biomedical functionality is then provided by only modifying or personalizing the upper layers of a conventional TFT process.

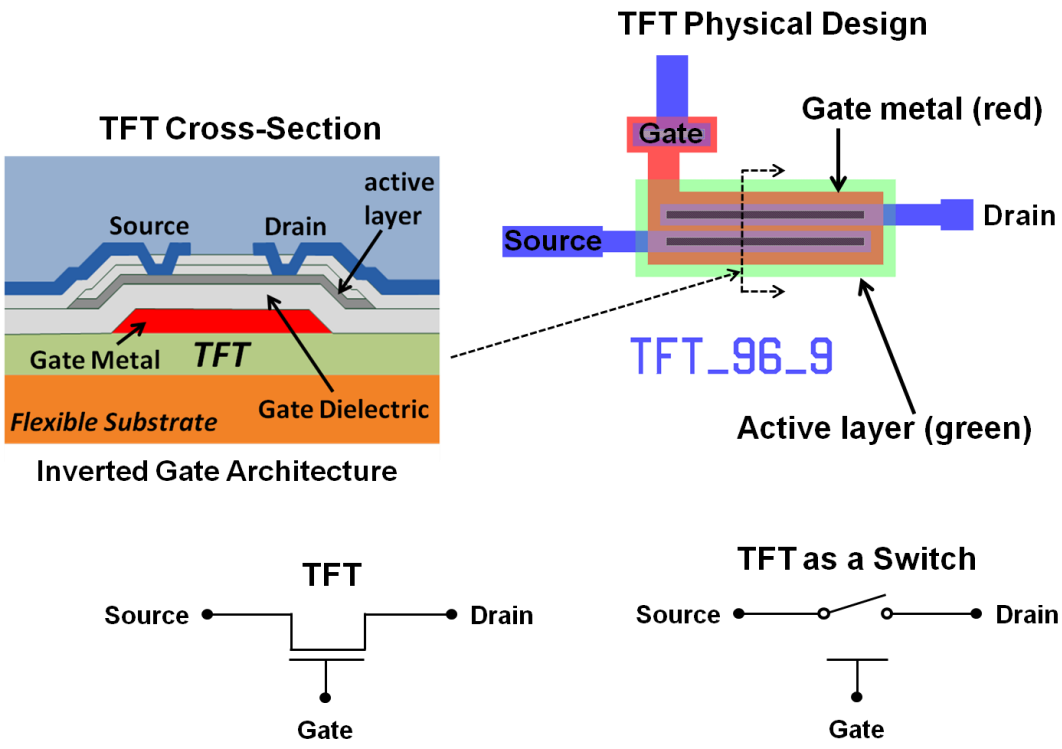

Figure 2. TFT device cross-section and physical design of a TFT with a device width of 96 µm and a length of 9 µm.

TFT Operation: To operate as a switch, a voltage is applied to the gate electrode of the TFT to turn it either on or off (Figure 2). To turn the TFT switch on, a positive voltage is applied to the gate electrode. This increases the concentration of electrons in the device active layer, reducing its resistance, which then allows current to flow between

the metal source and drain electrodes. This electrically connects the source and drain electrodes together through the active layer shown in Figure 2. To turn a TFT off, a negative voltage is applied to the gate electrode. This removes electrons from the active layer, which prevents current from flowing between the source and drain electrodes (Powell 1989).

Active Matrix TFT Array Technology

When used in display technology, the TFTs are configured as large arrays of identical elements, typically called pixels. Below is an array of pixels with two rows and two columns, where each pixel one TFT switch and one storage capacitor (Cs).

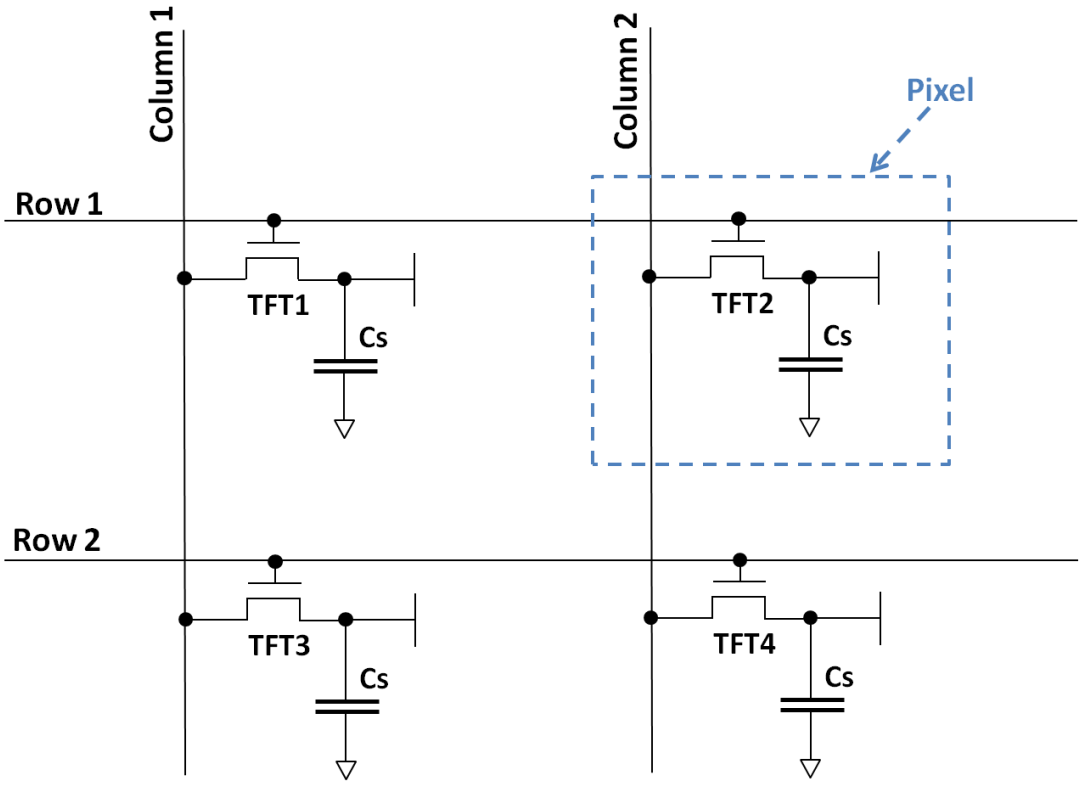

Figure 3. Active matrix TFT array with two rows and two columns.

The number of individual pixels in the array defines its resolution. For example, an XGA resolution display has 1024 columns and 768 rows of identical pixels for a total of 786,432 individual pixels. If each pixel in the array can be individually addressed, the term "active matrix array" is used to describe the device (Brody et al. 1975). In an active-matrix organic light emitting display (OLED) or liquid crystal display (LCD) array, the TFTs provide the individual addressability (turn on) function for each pixel (Sarma 2003). Typically, peripheral CMOS integrated circuits are used to activate and/or read out the individual rows or columns. For example, to read out the voltages stored on the pixel capacitors Cs in Figure 3, external address lines would turn on the TFTs in row 1 by applying a positive voltage to row 1, while simultaneously applying a negative voltage to row 2 to turn the TFTs off. External read out circuitry connected to column 1 and column 2 can then detect the stored Cs voltages on TFT1 and TFT2.

Flexible Substrate Technology

Conceptually, the approach used to make a TFT active matrix array flexible is straightforward. The flexible display TFT manufacturing process is essentially identical to the process used to manufacture flat-panel LCD displays on glass substrates. To make the device flexible, the starting glass substrate is replaced by a 125μm thick DuPont Teijin Films Teonex® polyethylene naphthalate (PEN) flexible plastic substrate temporarily bonded to a rigid alumina carrier (Haq et al. 2010, Raupp, O'Rourke, O'Brien, et al. 2007). After the TFT process steps are completed, the flexible plastic PEN

substrate with patterned TFT layers on top is just peeled off, similar to peeling off a Post-it® note, as illustrated in Figure 4.

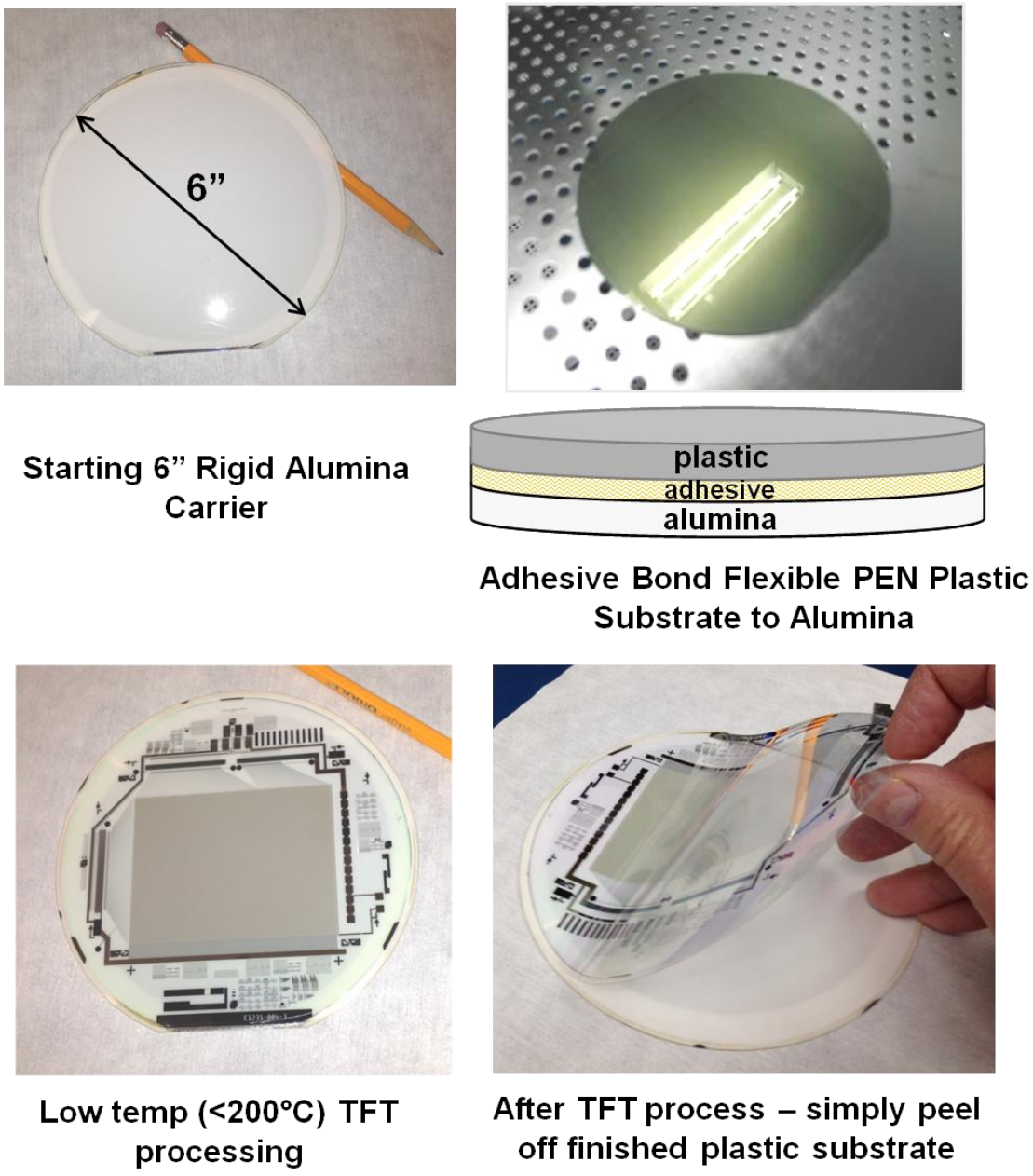

Figure 4. Flexible TFT plastic substrate manufactured using a temporary bond/de-bond process on a 6 inch rigid substrate.

The temporary rigid alumina carrier allows the flexible TFT active matrix array to be processing using unmodified, off-the-shelf, thin-film semiconductor process tooling, which can currently only handle rigid glass substrates or silicon wafers. However, to avoid exceeding the PEN plastic substrate transition temperature (i.e., avoid melting it), the maximum processing temperature throughout the entire flexible electronics process sequence is limited to a maximum of ~180°C, while typical glass substrate TFT or silicon wafer processing is >300°C (Wong and Salleo 2009). In addition to 6″ (150 mm diameter) flexible display substrates, the same temporary bond/de-bond process using PEN plastic substrates has also been successfully demonstrated on much larger, 370 mm x 470 mm, gen2 flexible display substrates (O'Brien et al. 2013).

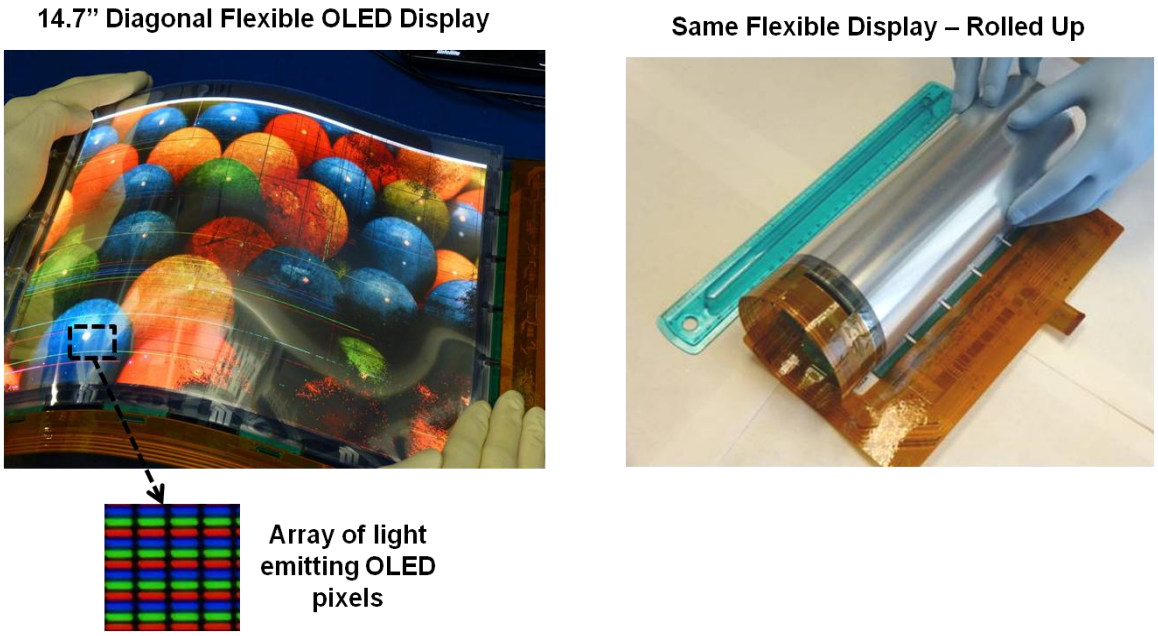

Figure 5. 14.7″ diagonal flexible color OLED display on a PEN plastic substrate manufactured at the ASU Flexible Electronics and Display Center.

The flexible (on plastic) TFT active matrix array backplane technology was then applied to develop and manufacture on a gen2 sized substrate, the 14.7" diagonal, flexible, 960 by 720 pixel resolution active matrix OLED (AMOLED) display shown above in Figure 5 (O'Brien et al. 2013). At the time of writing, this was the largest reported flexible color OLED display (2014a). The 14.7″ flexible OLED display, illustrated in Figure 5, was designed by the author in collaboration with K. Kaftanoglu.

Related Flexible Biomedical Device Research

For this work, it's important to recognize the large body of flexible biomedical device research from the John Rogers Research Group at the University of Illinois at Urbana-Champaign (2013g). The Rogers group pioneered research in ultra-thin, stretchable, tissue-like flexible electronic devices for numerous biomedical-related applications. Some of their recent research highlights include a flexible microelectrode array that maps electrical brain activity in vivo (Viventi et al. 2011), flexible in vivo optoelectronic neural simulators for optogenetic applications (Kim et al. 2010, Kim et al. 2013, McCall et al. 2013), and stretchable electronics which can conform to the surface of human skin (Yeo et al. 2013).

One of the key distinguishing features of the Rogers flexible devices is the wavy metal used for the metal interconnect. This wavy metal design, shown in Figure 6, is commonly used in the Rogers flexible biomedical devices to function as built-in strain relief for metal interconnects to prevent them from breaking when the devices are stretched or expanded, such as when inflating a balloon at the end of a catheter (Kim et al. 2011). Unlike the Rogers stretchable devices, the PEN plastic substrates used for this

work, while both flexible and bendable, are not stretchable. This allows them to be both designed and manufactured using conventional, high-density metal interconnects in a Manhattan style geometry.

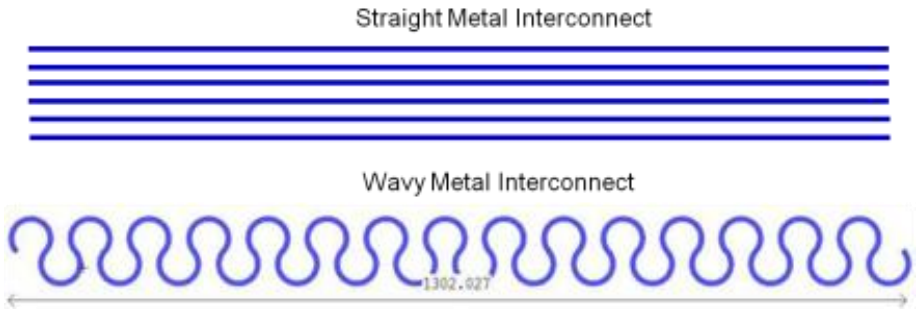

Figure 6. Approximately 1.3 mm length of wavy and straight metal interconnect.

As illustrated in Figure 6, approximately six straight metal lines can fit in the same space as one wavy metal interconnect. This difference is important in high-resolution, flexible, active-matrix array applications, such as flexible displays and flexible digital x-ray detectors which can require millions of metal interconnections to the integrated TFTs on the flexible substrate.

The other fundamental difference between the Rogers stretchable devices and the flexible biomedical devices described in this work is how each device is manufactured. The Rogers devices are manufactured by bonding discrete electronic components, manufactured separately, such as light-emitting diodes (Kim et al. 2013), to very thin, and typically stretchable plastic substrate that just consists of metal interconnect. In the flexible electronics technology used for this work, the flexible active matrix arrays are manufactured using conventional thin film transistor (flat-panel display) process tooling

on flexible plastic substrates (Raupp, O'Rourke, O'Brien, et al. 2007), with both metal interconnect as well as active thin film semiconductor devices, such as TFTs and PiN photodiodes, fabricated on the same plastic substrate.

Integrating active components and metal interconnect on the same (flexible) substrate using conventional flat-panel-display process tooling allows the active devices to be placed much closer together than would be possible using discrete component assembly methods. This allows large high resolution million+ pixel active-matrix arrays, such as flexible displays or digital x-ray detectors, to be manufactured on plastic substrates, as opposed to only being able to manufacture much lower resolution arrays using just a few discrete components per device.

Figure 7. Flexible displays manufactured on a 370 mm x 470 mm gen2 PEN plastic substrate, after debond and prior to singulation. Bendable, but not stretcheable.

Using conventional flat-panel-display processing to manufacture flexible electronics is also key to keep manufacturing costs down for low-cost and/or disposable biomedical applications. As evident to anyone who has recently priced a flat-panel television, LCD HDTVs manufactured using thin film TFTs on large substrates, cost only about $10 per diagonal inch, which translates to less than 10¢ per square centimeter of active display area.

CHAPTER 2

FLEXIBLE DIGITAL X-RAY IMAGING

Random chance seems to have operated in our favor.

Mr. Spock, *Star Trek*

Today's flat-panel digital x-ray image sensors, which have been in production since the mid-1990s, are produced exclusively on glass substrates. While acceptable for use in a hospital or doctor's office, conventional glass-substrate digital x-ray sensors are too fragile for use outside of these controlled environments without extensive reinforcement. Reinforcement, however, significantly increases weight and bulk, making glass substrate detectors impractical for remote diagnostic applications, which demand rugged as well as lightweight x-ray detectors. Additionally, glass-substrate x-ray detectors are inherently rigid, which limits their use in curved and conformal x-ray imaging applications. However, by extending flexible electronics display technology previously demonstrated on flexible plastic-substrate-based electrophoretic and OLED displays, it is now also possible to manufacture more durable, lightweight, and conformable digital x-ray detectors. This chapter provides details on the development effort, performed by the Arizona State University (ASU) Flexible Electronics and Display Center team in partnership with the Palo Alto Research Center (PARC), of one particular flexible digital x-ray detector, with a focus on the author's work as the lead designer for the effort. At the time of writing, this was the world's largest reported flexible digital x-ray detector (2014b)

Why Flexible?

Digital radiographs taken using digital x-ray detectors are currently the most common medical diagnostic procedure. Data from 2009 reported that over 1.5 billion radiological procedures were performed annually, with chest x-rays the most common (Tredwell et al. June 22-28, 2009). Surprisingly, while the developed world currently has a larger percentage of elderly citizens, the most rapidly aging populations are now in less developed countries. The World Health Organization (WHO) projects that between 2010 and 2050, the percentage of elderly in the less-developed world will increase by more than 250%, compared to only a 71% increase in the developed world (Oct 2011). Rising incomes in many of these less-developed countries, combined with the aging population, are expected to increase the demand for advanced medical care, including x-ray imaging.

One assumption is that these emerging medical imaging markets will skip older-style x-ray photographic film and go straight to digital x-ray technology (Tredwell et al. June 22-28, 2009). However, medical-imaging applications in these developing markets are expected to impose additional durability requirements, limiting the use of conventional fragile glass-substrate-based flat-panel digital x-ray detectors and creating demand for a more ruggedized detector. Medical first responders and industrial x-ray imaging professionals also have similar needs for a rugged digital x-ray detector, primarily for use in remote diagnostic applications (2013e).

Flexible digital x-ray detectors manufactured on unbreakable plastic substrates are designed specifically to meet these higher durability x-ray imaging applications.

Additionally, adding the ability to bend or curve to a conventional flat-panel digital x-ray detector also has the potential to enhance its functionality and clinical value in medical and industrial diagnostic applications (Wong et al. Nov-Dec, 2011).

Digital X-Ray Detector Fundamentals

At the conceptual level, a digital x-ray detector is essentially a digital camera, albeit an extremely large one, with typical panel (detector) sizes between 20 and 43 cm's. An x-ray source provides the illumination, and the x-ray detector functions similarly to the solid state CMOS or charge coupled device (CCD) imager in a digital camera. However, unlike CCDs or CMOS imagers which use silicon-wafer semiconductor processing, conventional flat-panel digital x-rays are currently manufactured using TFT technology on extremely large glass substrates.

The main components of a conventional digital x-ray assembly are the TFT-based digital x-ray detector, a light-blocking housing, peripheral readout and drive electronics, and a scintillator. The scintillator, typically constructed of terbium-doped gadolinium dioxide sulfide or cesium iodide, converts the incident x-rays from the source into photons, and emits visible light with an intensity proportional to the energy of incident x-rays (Street, Lu, and Ready 2003, Moy 1999). When imaging, dense material, such as bone or metal, blocks incident x-rays from striking the scintillator surface, producing fewer photons underneath the dense materials than under soft tissue, creating the characteristic grayscale x-ray image. As illustrated in Figure 8, a typical flat-panel digital x-ray detector is an insulating (glass) substrate completely covered by an active matrix array of imaging pixels.

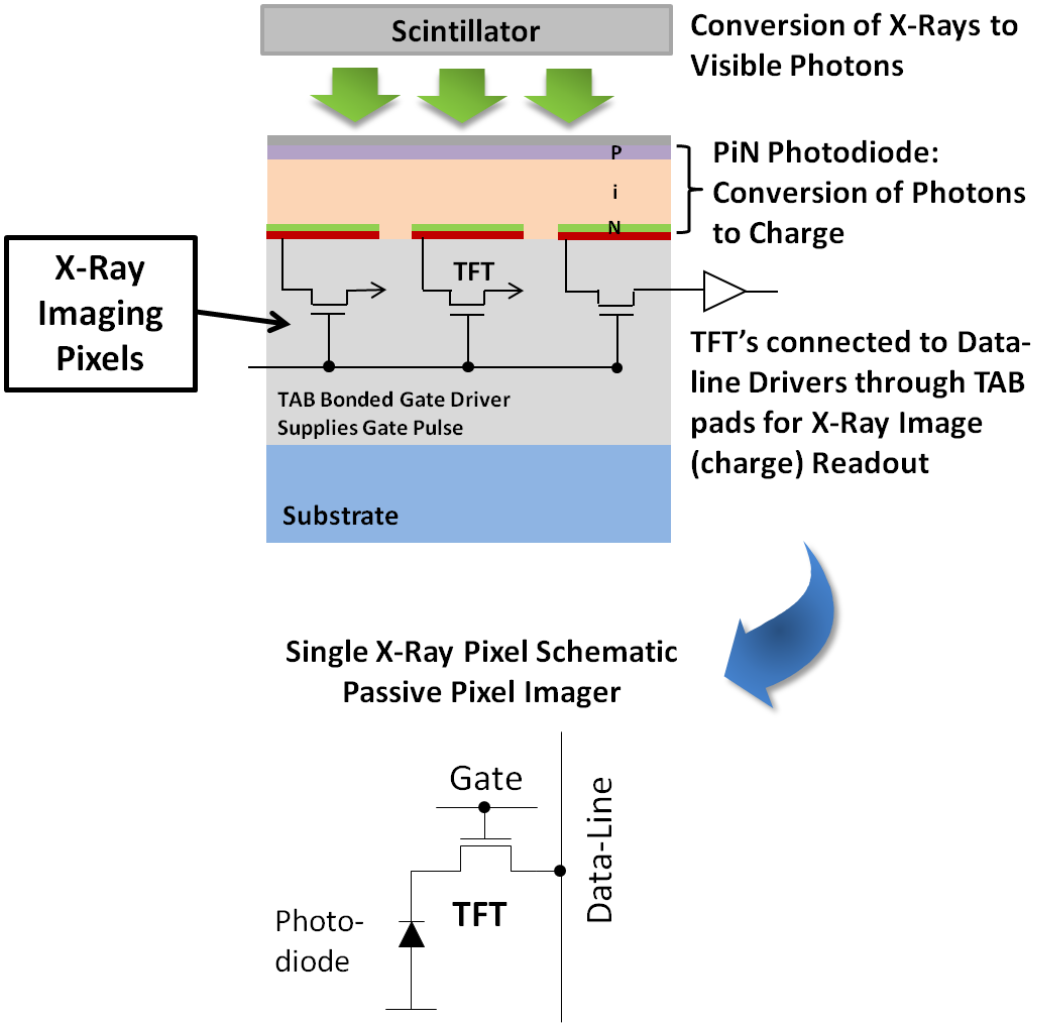

Figure 8. Digital x-ray detector structure.

Each pixel in the array has one TFT transistor and an associated photodiode. The TFT functions as an on/off switch that electrically connects the photodiode to an associated dataline when the gate line is turned on with a large positive voltage. The hydrogenated amorphous silicon (a-Si:H) PiN photodiode can be thought of as a miniature photovoltaic solar cell, which converts incident photons into electrical charges proportional to their light intensity. During x-ray exposure, charge from the incident

photons accumulates in each pixel cell and is stored within the pixel cell's capacitance (Boudry and Antonuk 1994, Street and Antonuk 1993). After the x-ray source shuts off, the charge is read out and analyzed by peripheral circuitry, and then transferred to an external computer to produce the grayscale digital x-ray image, which is proportional to the stored charge (Bushberg et al. 2002, Weisfield et al. 2004).

Applying Flexible Display Technology

To make digital x-ray detectors unbreakable and flexible, our solution was to build the new flexible digital x-ray detector using the same low-temperature TFT process currently used to manufacture flexible electrophoretic and OLED electronic displays at the ASU Flexible Electronics and Display Center (Venugopal et al. May 2010, Smith, Marrs, et al. 2013, 2013d, 2013e)

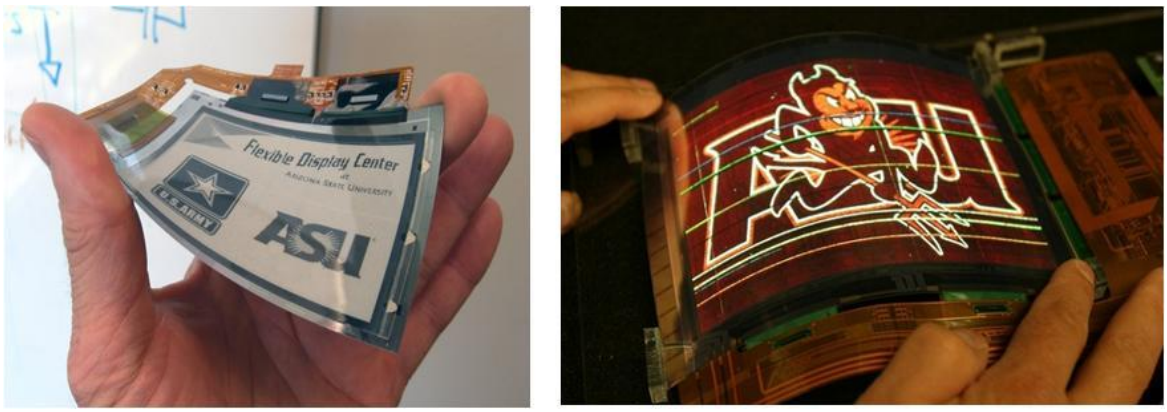

Figure 9. Photographs of flexible displays on plastic substrates. The photograph on the left is a flexible electrophoretic display, and on the right is a full color flexible 7.4" diagonal OLED display.

The essence of this technical approach involved replacing the existing fragile glass substrate used in conventional digital x-ray detector TFT and PiN photodiode device processing with a thin, flexible, and extremely tough polyethylene naphthalate (PEN) plastic substrate manufactured by DuPont Teijin Films Teonex® (2013b, Haq et al. 2010).

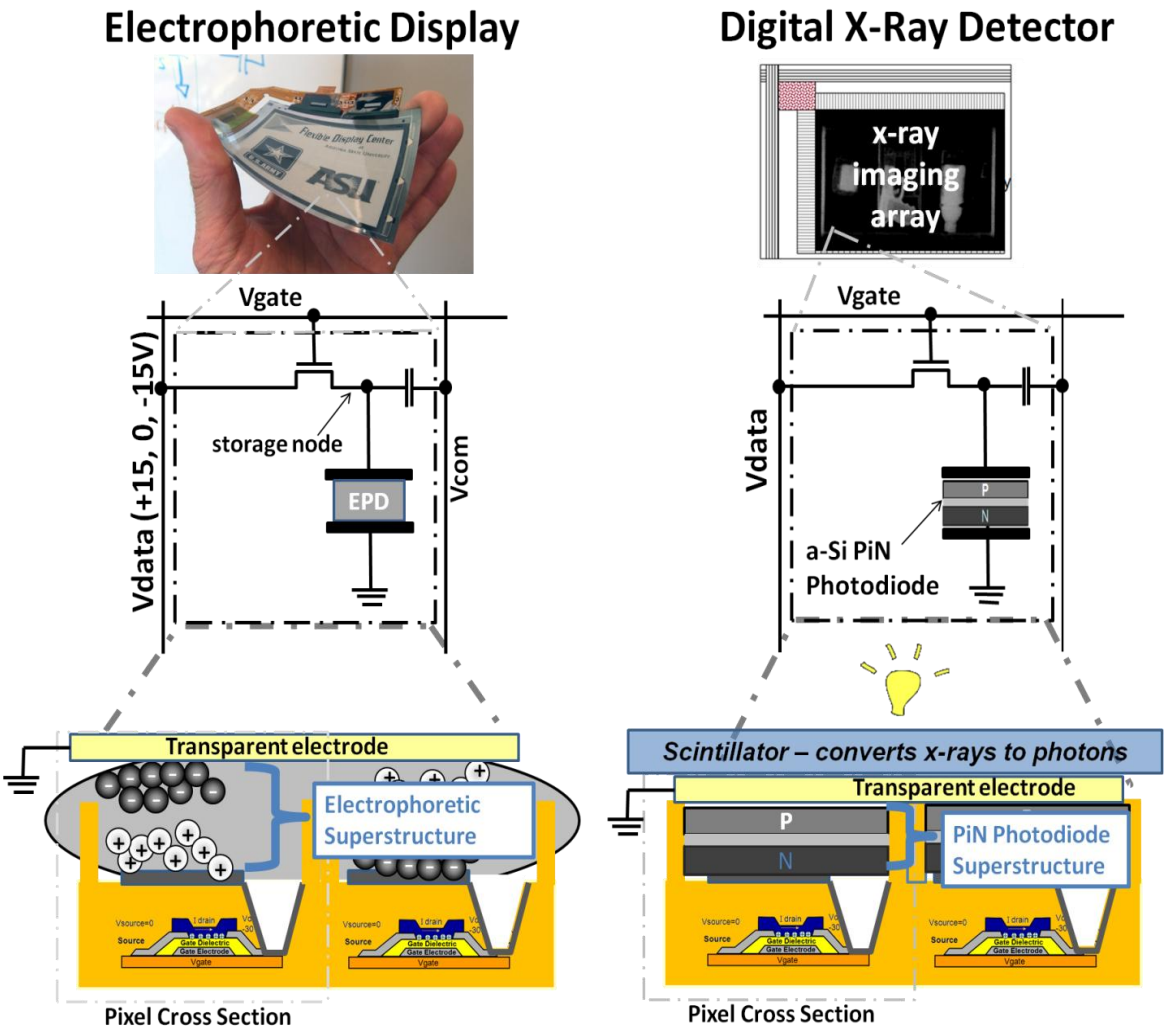

Figure 10. Comparison of flexible display to flexible digital x-ray detector architecture - showing the difference in superstructures.

Of course, a flexible display is a display device and a flexible x-ray detector is a sensor, which at first may lead one to think they are quite different structurally and essentially opposite or very different types of devices. However, as illustrated in Figure 10, both have a surprising number of similarities. From the comparison above, the only significant physical difference between the x-ray sensor and the electrophoretic display on the left is the different superstructure layers on top of both devices. For the electrophoretic display, a layer of electronic ink, which consists of charged black and white particles, is placed between the top pixel electrode and a global transparent electrode. While on the digital x-ray detector, a thin-film a-Si:H PiN photodiode layer is instead deposited between the top electrode and a global transparent electrode. Underneath these different superstructures, both devices use essentially the same type of active matrix TFT array for the substructure, with fairly similar design and fundamentally identical TFT processing. It was this observation that the upper layers of an existing flexible-display superstructure can be personalized to provide completely new functionality that was instrumental in leveraging existing flexible-display technology to then develop the prototype flexible digital x-ray detector described in this work.

This personalization of the superstructure in a flat-panel, TFT-based display process to create new types of devices is not a new concept, and is common in the commercial display industry. Referring again to the electrophoretic display cross-section in Figure 10, an LCD uses a similar TFT active-matrix array substructure, but instead of electronic ink particles, a layer of liquid crystals is placed over the top electrode of an LCD display (Street 2000). Similar to electrophoretic display, a transparent counter electrode is then positioned over this liquid crystal layer (Venugopal et al. May 2010). A

comparable personalization approach is used to manufacture OLED displays. OLED displays use a deposited thin film layer (or layers) of organic material between a counter electrode (cathode) and a transparent anode for light emission (Sarma 2003, O'Brien et al. 2013). Again, there is just a different thin film layer between the cathode and anode layers in the device superstructure to provide completely new functionality. Directly underneath the superstructure for all of the different display devices is a TFT active matrix array, also called the backplane. However, there are subtle design differences in the TFT active-matrix arrays used for the different display technologies. The same is also true of the active matrix array for digital x-ray detector which, as a sensor, requires a different design approach than a display even though it still uses comparable TFT processing. As might be expected, because it's a sensor, digital x-ray detector testing is also quite different than the method used to test flat panel displays.

The balance of this chapter focuses on the TFT active matrix design and test development unique to the flexible digital x-ray detector developed for this work. The x-ray detector design was performed by the author in collaboration with K. Kaftanoglu, while the majority of details on the flexible a-Si:H PiN photodiode superstructure process development work performed by the ASU Flexible Electronics and Display Center process engineering team can be found in the following reference (Marrs, Bawolek, Smith, et al. 2013), along with earlier similar work from Street (Street et al. 2009).

Flexible Digital X-Ray Detector Active Matrix Array Architecture

For this work, a 7.9″ diagonal flexible digital x-ray active matrix array (backplane) was designed with 640 columns and 720 rows.

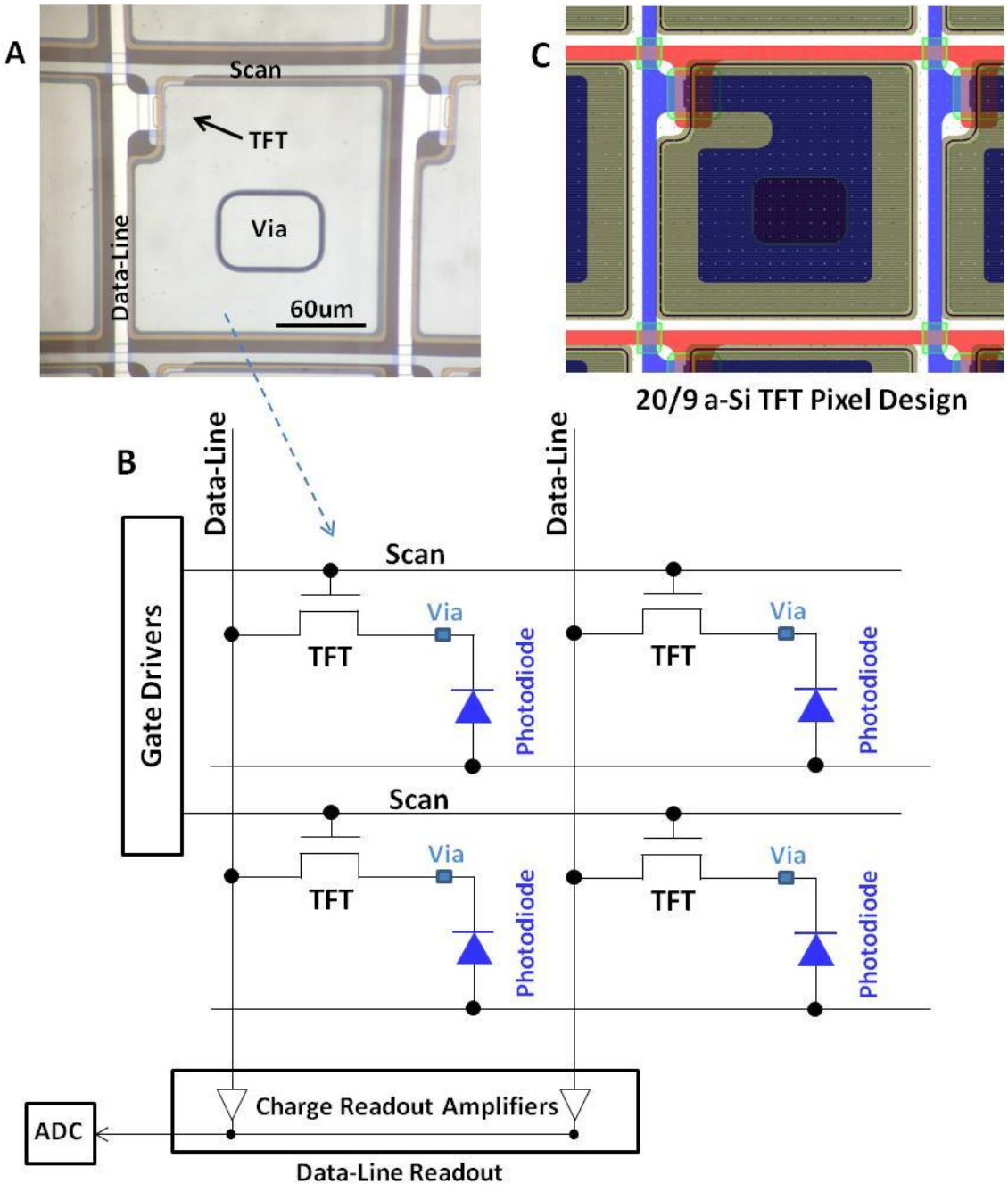

Figure 11. Passive pixel sensor active matrix array for 7.9”digital x-ray detector. (A) Optical photograph of a single a-Si TFT x-ray 1T pixel prior to deposition of the PiN photodiode. Pixel pitch is 207μm. (B) Simplified block diagram of digital x-ray active matrix pixel array illustrating connections to external TFT gate drivers and data-line charge readout amplifiers and associated analog to digital converter (ADC). (C) Physical design of a-Si:H 1T flexible x-ray pixel cell.

For digital x-ray detectors, the columns are typically called datalines and the rows are called scan lines. A 1-TFT transistor (1T) passive pixel architecture was used, with a pixel pitch of 207µms and 3 µm feature size design rules for the TFTs. Again, each x-ray 1T pixel cell consists of a PiN photodiode and a TFT switch, which electrically connects the PiN photodiode to the dataline as illustrated in the simplified block diagram in Figure 11B. This pixel sensor architecture is referred to as passive, because the TFT functions only as an on/off switch and does not provide any in-pixel amplification of the detected signal (Weisfield et al. 1998, Weisfield et al. 1999). The 1T passive (x-ray) pixel layout, captured is Figure 11C, also uses a full fill-factor design approach (Rahn et al. June 1999).

The design was fabricated using amorphous silicon (a-Si) TFTs on a 125µm thick DuPont Teijin Films Teonex® PEN plastic substrate bonded to an alumina carrier. The a-Si TFT process uses an n-type enhancement mode TFT using a bottom metal gate, inverted-staggered structure, and an active channel passivation layer (Raupp, O'Rourke, O'Brien, et al. 2007). For the TFT process sequence, molybdenum is first patterned on the PEN substrate to form the gate metal layer (scan in Figure 11), followed by a thin film deposition sequence that includes the gate dielectric layer, the active channel layer, and a protective passivation layer (Figure 12). For a-Si TFTs, the active device layer is amorphous silicon, and the gate dielectric and protective layer is silicon nitride. Contacts are then opened to the active layers, and the source/drain metal interconnect is deposited using an N+ doped amorphous silicon and aluminum bi-layer. The source/drain metal interconnect layer is annotated in Figure 11 as Data-Line. A low dielectric constant

material is spun on as an insulating interlevel dielectric layer (ILD), after which vias are opened to the source/drain metal interconnect layer.

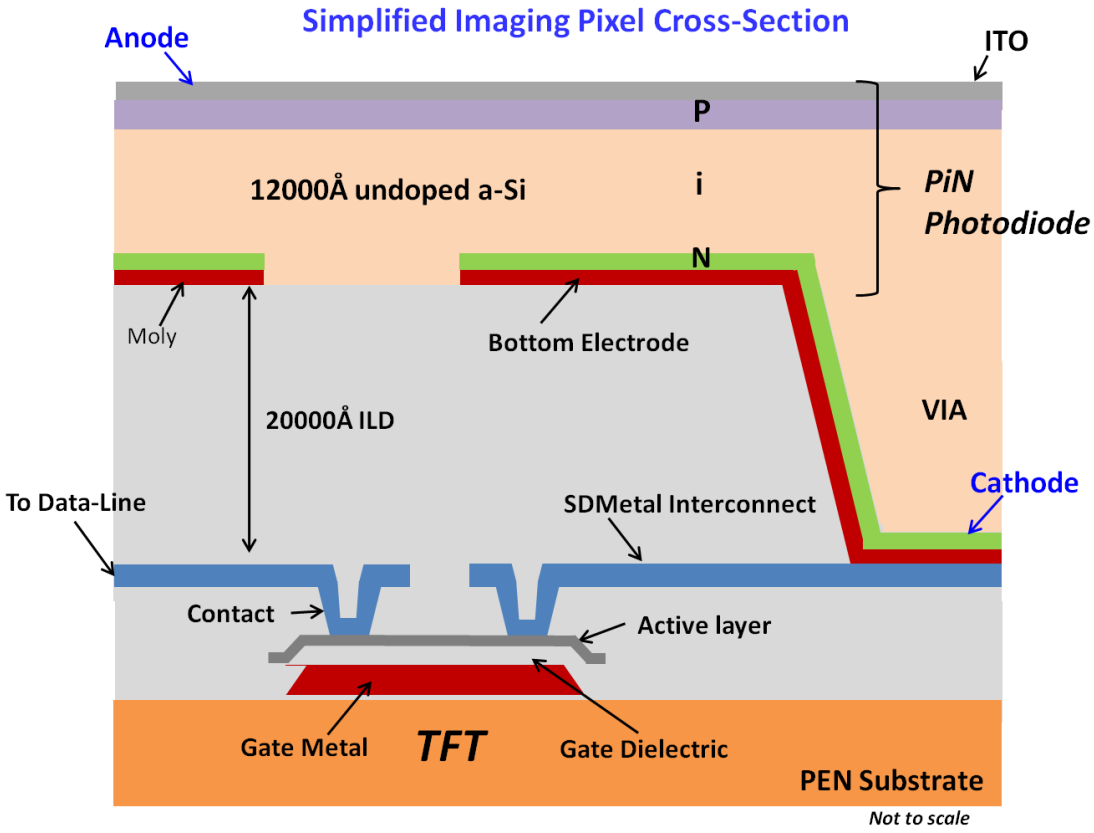

Figure 12. Full fill factor x-ray imaging pixel cross-section with a-Si:H PiN photodiode superstructure on the flexible PEN plastic substrate.

In the full-factor pixel design (Figure 12 pixel cross-section), the via in each pixel is connected to an isolated molybdenum metal mushroom metal pad (bottom electrode in figure) that, in combination with a coincident patterned N+ doped a-Si layer, defines the cathode connection to the a-Si:H PiN photodiode and provides the electrical isolation between neighboring pixels. Next, a continuous layer of intrinsic undoped a-Si:H is deposited and combined with an in-situ deposited layer of P+ doped a-Si, followed by an

ITO transparent conductor, to form the light absorption layer and global anode as also illustrated in Figure 12. Figure 11A is an optical photograph of the 207μm pixel immediately prior to these PiN photodiode processing steps. It is this continuous layer of a-Si:H light-absorption layer over the entire pixel array, combined with the continuous P+ and ITO layers, that make this type of pixel design full fill factor, as well as provide the personalization of the TFT active matrix sub-substructure to form the digital x-ray image sensor superstructure. In an alternate x-ray pixel design, the PiN photodiode layers are not continuous and instead are isolated (not continuous) in each pixel using a separate photo and a-Si:H PiN photodiode etch step. An array of top metal bus lines patterned on top of all of the pixels is then used to make the connection to each of the isolated pixel photodiode anodes (Tredwell et al. June 22-28, 2009), as opposed to the global transparent ITO electrode in the full fill factor design.

Flexible Digital X-Ray Detector Image Capture

Image capture using the Figure 11 passive pixel x-ray image sensor architecture is typically classified as a two-step operation—charge integration followed by the charge readout, which also functions as a reset (Karim et al. January 2006). During charge integration, the pixel TFT switch is turned off. Again, a negative bias is applied to the TFT gate electrode, as opposed to zero volts, to insure that the TFT switch is off. With the TFT off, the a-Si:H PiN photodiode is now electrically isolated from the dataline and immediately starts integrating charge, which is a function of the incident light intensity from the scintillator layer – with the x-ray source on. During each frame period, the integrated charge is collected and stored in each pixel using the PiN photodiode

capacitance. However, some x-ray detector designs also include a separate in-pixel capacitor (Couture et al. 2005).

For the readout/reset step which follows, the TFT switch is turned on by applying a strongly positive gate bias Vgs, and all datalines are now read out in parallel. Turning on the TFT transfers the stored charge on the pixel photodiode to the dataline, where it can be read out using external charge-integration amplifiers connected to each dataline (Figure 11). For readout, each dataline is connected to a virtual ground through the external charge amplifier, while a negative voltage bias is applied to the global transparent electrode connected to the anode of every a-Si:H PiN photodiode to reverse bias and deplete the PiN photodiode charge storage layer. The charge-readout step is how much charge is required to reset the PiN photodiode to its fully depleted state. Hence, the reset can be thought of as a measurement of how much charge is required to recharge or re-deplete the PiN photodiode. For example, the depletion region in a PiN photodiode that has been exposed to more light is reduced more than one exposed to less light, and discharges by the amount Qs (Street 1999).

$$Q_S = q\ \eta_{QE}\ n \tag{1}$$

Where η_{QE} is the wavelength-dependent quantum efficiency of the a-Si:H PiN photodiode and *n* is the number of incident photons. Hence, during readout, the pixels exposed to more light will require more recharging to reset their PiN photodiode depletion regions. At the output of the charge-integration amplifiers, more reset charge

(more recharging) now results in a corresponding larger output signal voltage V_{OUT}, while pixels exposed to less light will have a lower output voltage, where:

$$V_{\mathrm{OUT}} \propto \frac{Q_S}{C_S} \tag{2}$$

and Cs is the pixel storage capacitance. The charge-amplifier voltage outputs are then multiplexed and connected to an analog-to-digital converter (ADC), which then transfers the now-digital representation of the detected x-ray image to an integrated computer for image processing and display of the captured digital x-ray image (Taghibakhsh 2008).

X-Ray Detector Design Optimization

As part of the x-ray detector design flow, the pixel TFTs are sized (physical device width and length) to insure that the internal pixel storage capacitance is recharged during readout through the dataline. The time to recharge τ is proportional to the on resistance of the pixel TFT and the pixel capacitance (the $\tau = RC$). The required read time is set by both the number of rows and the readout rate for the entire active matrix array. A larger, higher-resolution active matrix array with more rows and a faster readout (frames per second) would require a TFT sized with less on resistance (Ron). This is typically done by increasing the physical width of the TFT. For fluoroscopy, the x-ray beam is on continuously and the captured x-ray images are updated at video frame rates. This translates to read-out rates of up to 30 frames per second (fps) for fluoroscopy. For this 7.9" diagonal detector backplane design with 720 rows, each row will need to be read out

every 46.3 µs to sustain 30 fps operation. The design optimization for the pixel TFT to meet these fluoroscopy timing contraints are outlined below.

$$\tau_{\text{READOUT}} = {}^{1}/_{fps} \times {}^{1}/_{\#rows} \quad (3)$$

A typical peripheral CMOS gate driver integrated circuit will require approximately 3 µs to turn on the row line τ_{ROW}, and a minimum of five time constants (RCs) are required to transfer the stored charge from the PiN photodiode to the dataline (Weisfield 1998), with 99.3% of the charge transferred after 5 time constants and 99.995% of the charge transferred after 10 time constants (Street 1999). Hence, using the following expression, the pixel RC time constant τ_{MIN} needs to be less than 8.7 µs for 5 time constants, and 4.3 µs for 10 time constants (for a 720 row design).

$$\tau_{\text{MIN}} = R_{ON} \times C_{PIX} < {}^{(\tau_{\text{READOUT}} - \tau_{\text{ROW}})}/_{\#timeconstants} \quad (4)$$

Assuming a typical x-ray pixel capacitance Cpix of ~1pF, (Street 1999) where:

$$C_{\text{pix}} = C_{\text{photodiode}} + C_{\text{parasitic}} \quad (5)$$

The TFT on resistance needs to be less than 4.3 MΩ, using the τ = RC relationship above, with τ = 4.3 µs from the more conservative 10 time constants. For typical digital x-ray

detector biasing, where the TFT gate voltage Vgs is much larger than the drain voltage Vds, the TFT transistor is not in saturation and the expression for the TFT drain current I_{ds} reduces to (Hosono, Kenji, and Hideo 2010, Brotherton 2013):

$$I_{\text{ds}} = \mu \frac{W}{L} Cox[(Vgs - Vth)Vds] \tag{6}$$

$$for \quad \text{Vgs} - \text{Vt} >> Vds \tag{7}$$

Rearranging the terms, the TFT on resistance Ron (Street 2009) can now be expressing using the following relationship.

$$R_{\text{on}} = \left[\mu \frac{W}{L} Cox[(Vgs - Vth)\right]^{-1} \tag{8}$$

$$from \quad R_{\text{on}} = {Vds}/{Ids} \tag{9}$$

The parameter μ is TFT device mobility, the TFT channel width is W, L is the channel length, Vth is the TFT threshold voltage, and the TFT gate dielectric capacitance is Cox. Rearranging the terms to solve for the TFT physical design parameters W (TFT width) and L (TFT length), the equation for TFT on resistance can be re-expressed as:

$$\frac{W}{L} = \left[\mu \, Cox(Vgs - Vth) \, R_{\text{on}}\right]^{-1} \tag{10}$$

Using typical a-Si TFT parameters and assuming a +20 volt gate drive (Vgs), a 1 volt threshold voltage (Vth), a minimum channel length L = 9 µm, and a 3000Å thick Si_3N_4 gate dielectric (Cox = 2.1 x 10^{-8} F/cm^2) (Marrs, Bawolek, O'Brien, et al. 2013, Raupp, O'Rourke, O'Brien, et al. 2007, Smith, Marrs, et al. 2013) and solving for W using the relationship for R_{on} above. The required TFT transistor width W is approximately 7 µms using an a-Si:H TFT mobility µ of 0.77 cm^2/V-s (Marrs et al. Oct 2011, Kaftanoglu et al. June 2011). For the actual array design, a more conservative TFT width of 20 µms was used.

Flexible Digital X-Ray Detector Assembly

For assembly with external readout electronics, the flexible 7.9" diagonal plastic substrate x-ray detectors were first debonded from their temporary alumina carriers (Haq et al. 2010) and trimmed to remove peripheral test structures (Figure 13A).

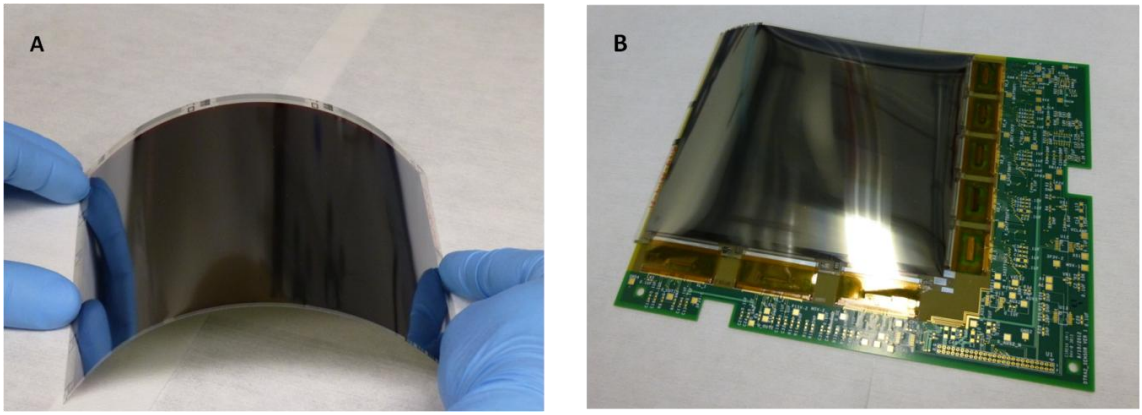

Figure 13. Flexible digital x-ray after debonding and after assembly. (A) 7.9″ diagonal 720 x 640 resolution array prior to assembly, (B) after assembly.

The flexible detectors were then tape-automated bonded (TAB) to external gate driver and charge integration amplifier chip-on-flex (COF) packaged integrated circuits (ICs). This intermediate assembly was then TAB bonded to a printed circuit board (PCB) as illustrated in Figure 13B (Smith, Marrs, et al. 2013). While the assembled unit is not flexible, it is still effectively all plastic and durable.

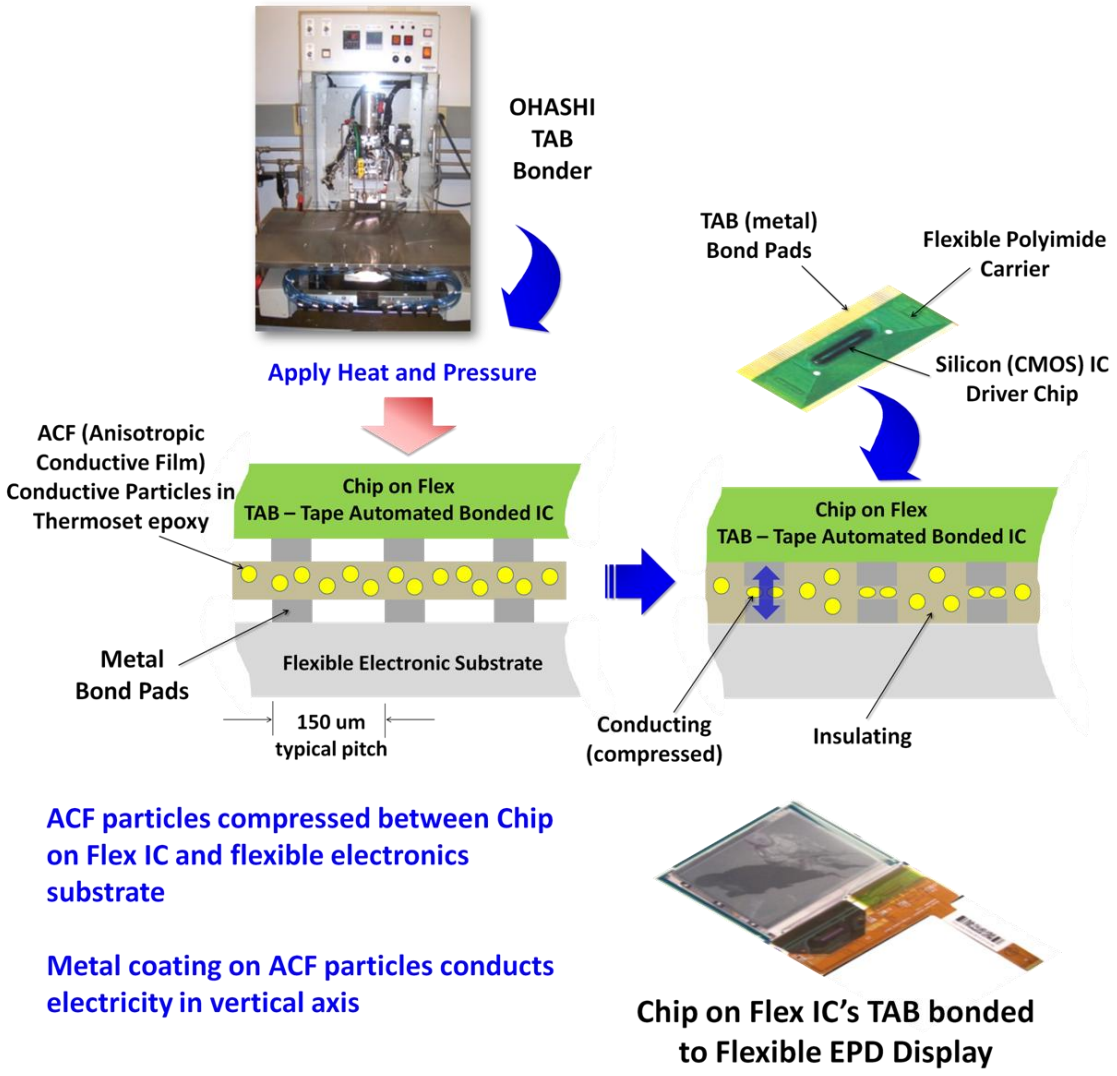

Figure 14. ACF TAB bonding of external (peripheral) chip–on-flex (COF) integrated circuits to flexible electronic substrates.

As illustrated in Figure 14, the connection between the x-ray detector substrate on the external COF ICs is achieved by positioning directionally conductive anisotropic conductive film (ACF) between the two opposing bond pads. An OHASHI bonder was used to apply localized heat and pressure to complete the ACF bond. Additionally, unlike conventional wire-bonding, which is both rigid and fragile, ACF bonding between the COF and flexible x-ray substrate also provides a significant degree of bendability or give in the final assembly, adding to the ruggedness of the assembled unit. 240 channel Solomon SSD1205U5s were used for the gate driver COFs, and STFC 128-channel XCHIPs were used for the charge integration amplifier COFs. Figure 13B shows three Solomon SSD1205U5 gate drivers bonded to the lower side of the array, and the five XCHIP COFs bonded to the right side of the 7.9″ diagonal flexible x-ray detector array.

PiN Photodiode Quantum Efficiency

To detect incident x-rays, the entire surface of the imaging array was then mated to the 464 μm thick flexible scintillator (2013a) shown below. The flexible scintillator is constructed of a terbium-doped gadolinium dioxide sulfide (Gd_2O_2S:Tb) phosphor layer on a bendable plastic base. When struck by x-rays, the Gd_2O_2S:Tb flexible scintillator emits visible green light with a peak at approximately 545nm, and with the intensity proportional to the energy of incident x-rays. The emitted generated green light is then captured by the individual a-Si:H PiN photodiodes positioned directly underneath the scintillator (Street et al. 2009).

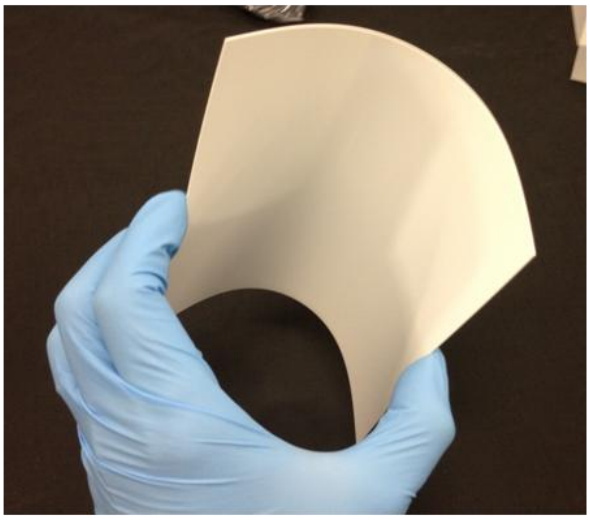

Figure 15. Flexible Gd_2O_2S:Tb scintillator.

The generated current I_{ph} from the incident light is expressed by the following relationship (Street 1999).

$$I_{\text{ph}} = G_L \times \eta_{QE} \tag{11}$$

Where η_{QE} is again the wavelength-dependent quantum efficiency (QE) of the a-Si:H PiN photodiode (Figure 16) and G_L is the incident (green) light intensity. Quantum efficiency is defined as the percentage of absorbed incident light (photons) that are converted into actual charge carriers in the a-Si:H PiN photodiode. The percentage of light absorbed A in the a-Si:H PiN photodiode is defined by the Beer-Lambert law, which is a function the absorption coefficient α for amorphous silicon and the a-Si:H PiN photodiode thickness d.

$$A = 1 - e^{-\alpha d} \tag{12}$$

The absorption coefficient α is dependent on the wavelength of the incident light, with shorter wavelength light absorbed near the top surface of the a-Si:H PiN photodiode, while longer wavelength incident light is absorbed further away from the surface (i.e., deeper). Using the relationship above for a 1.2 µm thick photodiode (parameter d), the percentage of light absorbed A for the emitted 546 nm (2.27 eV) green light from the scintillator is approximately 70% using the absorption coefficient for crystalline silicon (10^4 cm^{-1}) and >90% using typical absorption coefficients α for amorphous silicon (Ito et al. 2001).

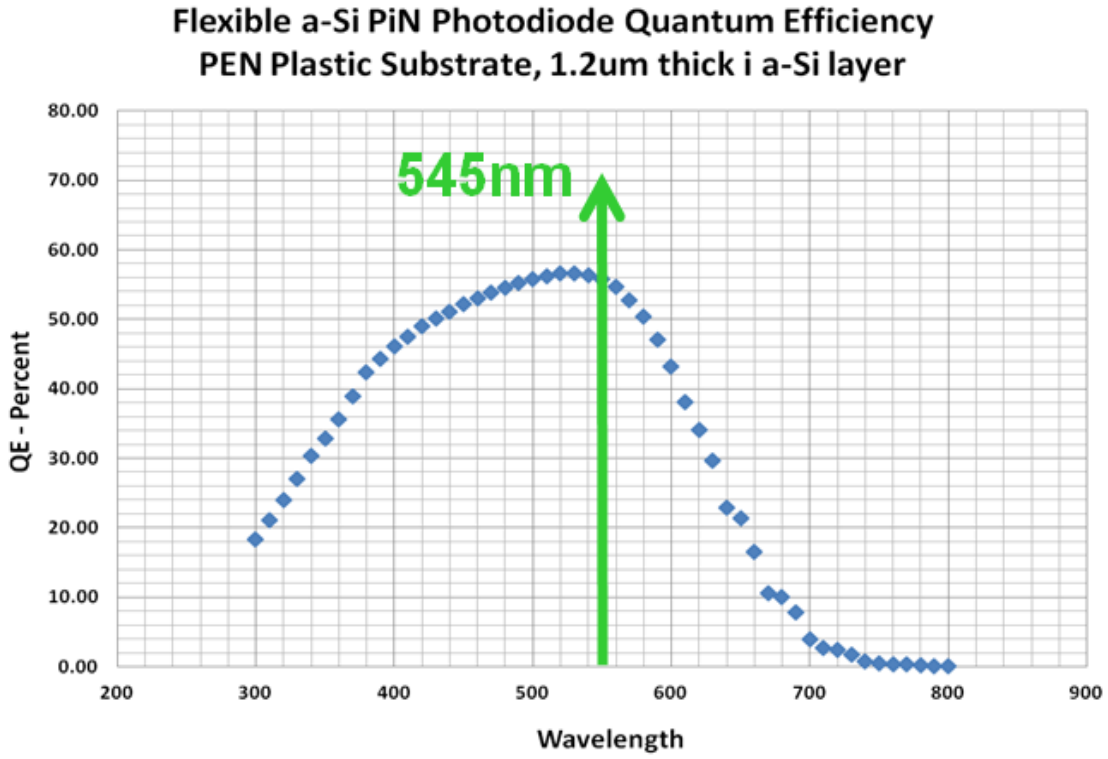

Figure 16. PiN photodiode wavelength-dependent quantum efficiency (QE) measurements for 1.2 µm thick intrinsic amorphous silicon layer at -1v reverse bias using PV Measurements QEX10 Quantum Efficiency Measurement System.

As shown in Figure 16, the measured a-Si:H PiN photodiode wavelength-dependent quantum efficiency peaks at approximately 60% near the emitted 545nm wavelength of the Gd_2O_2S:Tb flexible scintillator, shown by the green arrow. According to M. Marrs (Marrs), the observed 60% QE, which is significantly less than the predicted 90+% for amorphous silicon PiN photodiodes, can be attributed to reflective losses in the ITO electrode layer.

To perform the QE measurements, the a-Si:H PiN photodiode test structure shown below was designed and fabricated on a flexible PEN substrate. Courtesy of the ASU Solar Technology Lab (STL), the a-Si:H PiN photodiode QE was measured at a -1 volt reverse bias using a PV Measurements QEX10 Quantum Efficiency Measurement System (Jonsson 2013).

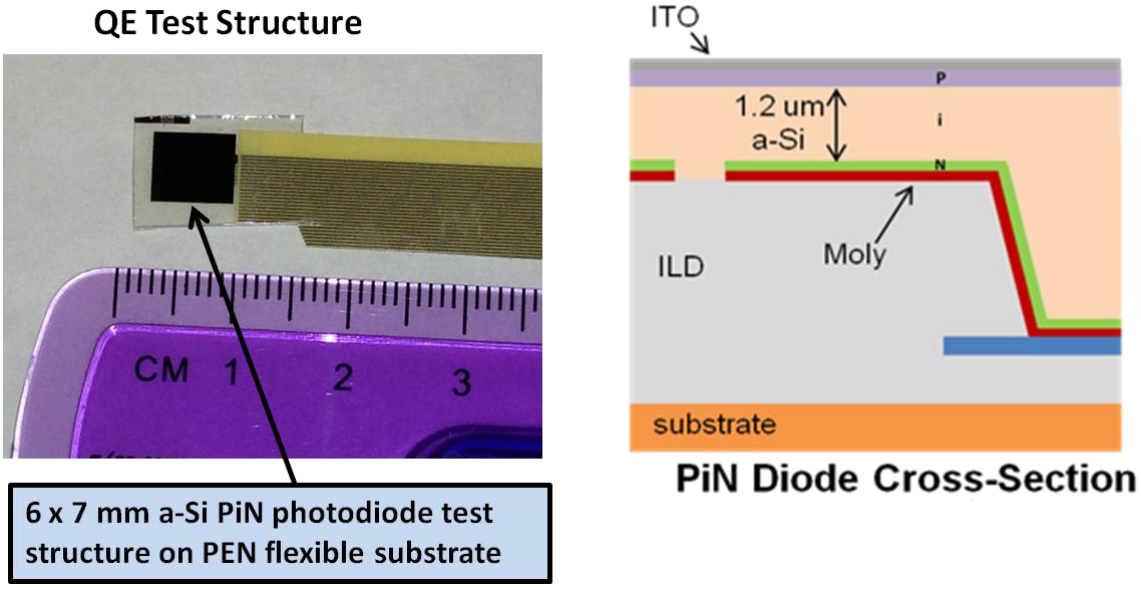

Figure 17. a-Si:H PiN Photodiode quantum efficiency test structure.

Optical Imaging Test Results

One of the more interesting optical test images for the assembled 7.9″ diagonal flexible x-ray detector is provided below in Figure 18, which clearly shows that the 7.9″ diagonal flexible x-ray detector is functional. The optical test image was generated by placing a transparency of a TG18-CH x-ray optical test pattern provided by American Association of Physicists in Medicine directly over the entire surface of the larger 7.9″ diagonal flexible detector array.

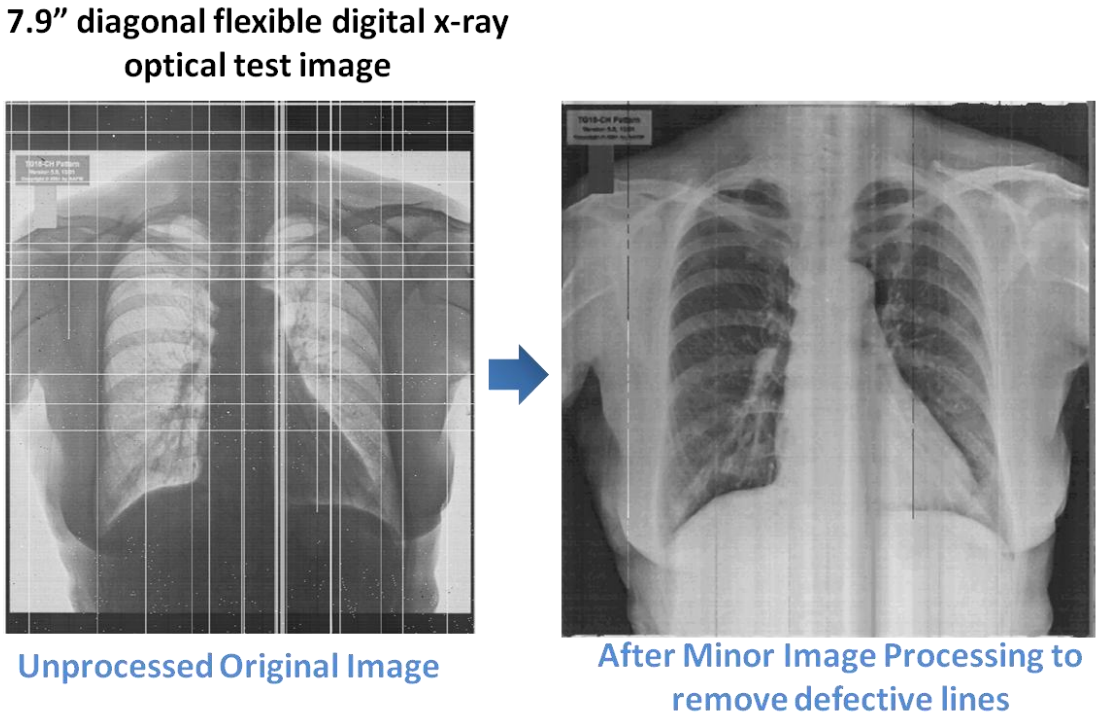

Figure 18. 7.9″ diagonal flexible x-ray optical test image for 7.9″ diagonal 720 x 640 array with TG18-CH x-ray optical (transparency) test pattern from American Association of Physicists in Medicine.

The test image was electronically captured using an electromechanical test fixture developed by PARC (Smith, Marrs, et al. 2013). To avoid oversaturating the captured image and to maximize contrast, optical imaging was performed in very dim ambient lighting. Limited post-image processing was then performed using Adobe Photoshop to first optimize the contrast, and then invert and despeckle the original image. This removed many of the line and pixel outs, and resulted in the final optimized image shown in Figure 18.

The observed black horizontal and vertical lines in the original unenhanced test image correspond to defective gate and datalines, while the single-point defects correspond to defective pixels. These defective lines and pixels are caused by particulate defects encountered during TFT processing. In a fielded production unit, more sophisticated digital image correction would be applied to remove the majority of defective lines and pixels from the final viewable x-ray image, as well as further optimize contrast and image quality (Rowlands).

Summary

This chapter demonstrated how flexible-display technology was applied to develop the world's largest flexible digital x-ray detector. These new flexible digital x-ray detectors are more durable than conventional glass-substrate detectors, and add the ability to conform to the surface of the object is being imaged. It was shown how the superstructure for an existing display process can be readily personalized to provide the new digital x-ray sensor functionality.

Adding the ability to curve or bend flexible x-ray detectors may also be invaluable in applications where x-ray imaging resolution is expected to be enhanced by conforming the detector to the item being inspected. By conforming, the distance or separation between the detector and the object of interest can be reduced significantly to enhance imaging resolution (Abbazadeh et al. 2012). For example, pipelines are typically x-rayed for cracks by placing the x-ray detector against the pipeline and then shooting the x-rays from the source through the pipeline wall and onto the detector. Since a conventional glass-substrate x-ray detector is flat (and rigid) while a typical pipeline wall is curved, it's impossible to press the x-ray detector surface flat against the curved pipeline surface. The x-ray image of the curved pipeline wall now can spread out before being hitting the detector surface, making smaller features, such as cracks, possibly more difficult to detect. A curved x-ray detector can conform to surface of the pipeline, which is expected to add the ability to detect finer cracks.

To find out if this concept works in practice, one envisioned test configuration is to attach a small, fine-line x-ray resolution test target to the inside of a diameter pipe. The resolution test target would be used to simulate different sized pipeline cracks—from small to large. X-ray images of the resolution-test target would then be taken with a conventional rigid x-ray detector placed next to the pipe, and then with a curved x-ray detector that conforms to the surface. If this simple test of conformal imaging works, smaller or finer feature on the resolution test structure should be readily visible on the new curved x-ray imager and invisible on the conventional rigid x-ray imager.

CHAPTER 3

SEAMLESS LARGE AREA DIGITAL RADIOGRAPHY

It's not complicated. Bigger is better.

AT&T

This chapter presents a new flexible electronics assembly concept designed to combine (tile) multiple small flexible digital x-ray detectors in a single much larger detector. The new tiling technique is optically seamless, and has the ability to scale up to extremely large x-ray imaging arrays. Feasibility and preliminary imaging performance was demonstrated by tiling several 16 x 16 pixel resolution prototype flexible x-ray detector test structures. Optical losses under typical digital radiography conditions were also measured by overlapping a plastic substrate flexible x-ray detector onto a commercial glass-substrate digital x-ray imaging array. Approximately 5% signal loss was observed in the transparent plastic overlap region, and the seam edge imaging artifact was demonstrated to be correctable using commercial gain calibration. A key medical imaging application for this technology is single exposure, low-dose, full-body digital radiography.

Background

As described in the previous chapter, active-matrix, flat-panel digital x-ray detectors manufactured on glass substrates, using a-Si:H TFTs as the switching elements, and a-Si:H PiN photodiodes as the optical detector, are now commonly used for digital radiography diagnostic procedures (Weisfield 1998). However, one constraint associated

with flat-panel digital x-ray detectors is the requirement for a large, active imaging area, especially in medical diagnostic applications such as a full-chest x-ray, which requires up to a 17″ x 17″ x-ray detector. Instead of manufacturing one large flat-panel detector, one alternative is to abut several smaller detectors together to form a larger, composite, optically gapless x-ray imaging array. Eliminating gaps or seams in digital radiography is required to insure that there are no missed features in the final composite x-ray image. Currently, conventional glass-substrate x-ray detectors can be assembled using the 4-sided butting (tiling) technique, illustrated in Figure 19, to create an optically seamless 4X larger detector from 4 separate digital x-ray detectors (Powell et al. 1998).

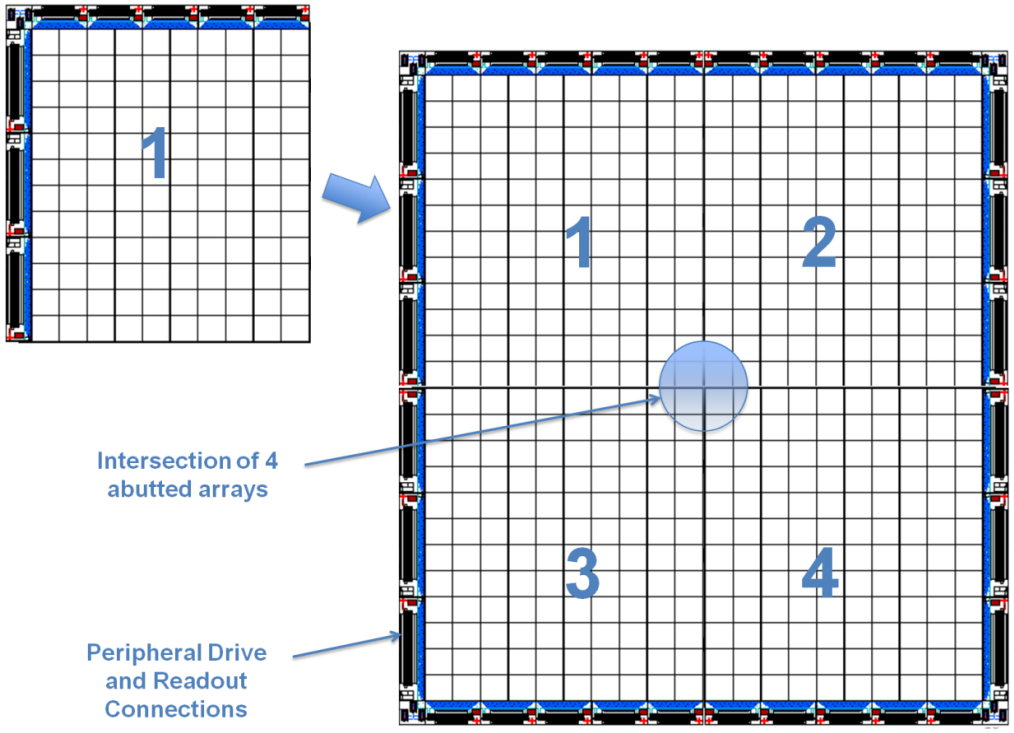

Figure 19. Conventional 4-sided butting using four x-ray detectors.

However, 4-sided butting is the limit of what is possible with conventional glass-substrate-based digital x-ray detectors to increase the maximum effective array size while preserving optically seamless imaging (no missing pixels). Referring to Figure 19 and Figure 20, the 4-sided limit is set by the requirement to connect peripheral drive and readout electronics to the periphery of each detector array (#1 to 4) while maintaining a planar detector surface for a scintillator that needs to be placed on top of the entire (4X tiled) glass substrate x-ray detector array.

As illustrated in Figure 20, if two glass-substrate x-ray detectors are stacked on top of each other instead of abutted, it's impossible for the scintillator to sit flat on both of the two x-ray detector surfaces.

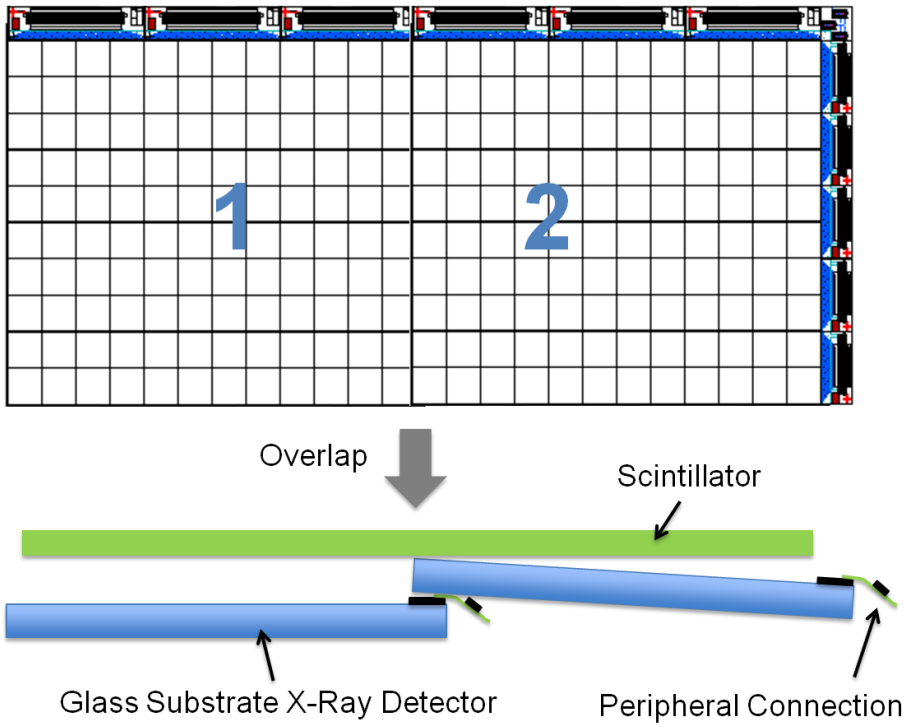

Figure 20. Limitations with overlapping glass substrate x-ray detectors.

If the scintillator doesn't sit flat on the entire surface, the photons generated in the separate scintillator during imaging will spread out and end up detected in neighboring pixels, degrading detected image quality. Optimum image quality is achieved when the scintillator is able to be pressed flat and directly onto the entire surface of the a-Si:H PiN photodiode (pixel) array. Additionally, because glass substrates are both thick and rigid, manufacturing a large-area bendable or curveable digital x-ray imaging array is currently impossible using glass-substrate x-ray detectors.

As a solution to these limitations, this work describes a new electronics assembly technique using multiple flexible x-ray detectors, again manufactured on the thin and optically transparent flexible PEN plastic substrate. To create a larger composite x-ray detector, the smaller flexible detectors are overlapped, similar to placing roofing shingles (Smith and Stowell 2012). This new flexible electronics assembly technique is optically seamless, and adds the ability to scale up to extremely large imaging array resolutions simply by adding (tiling) an unrestricted number of individual flexible x-ray detectors.

Principle of Flexible Electronic Tiles

A mechanical mockup constructed with nine individual flexible active-matrix arrays (flexible tiles) is used to help illustrate how the individual flexible x-ray detector tiles are combined to form the single, larger, composite 3 x 3 imaging array. As shown in Figure 21a, the transparent plastic substrates on each of the nine individual flexible active matrix arrays were first trimmed along a cut axis adjacent to both the bottom and right edges of the array. This leaves a transparent border along the two trimmed edges of the

detector as shown in the same figure. The border is transparent because the unpatterned (un-pixelated) PEN plastic substrate is optically transparent.

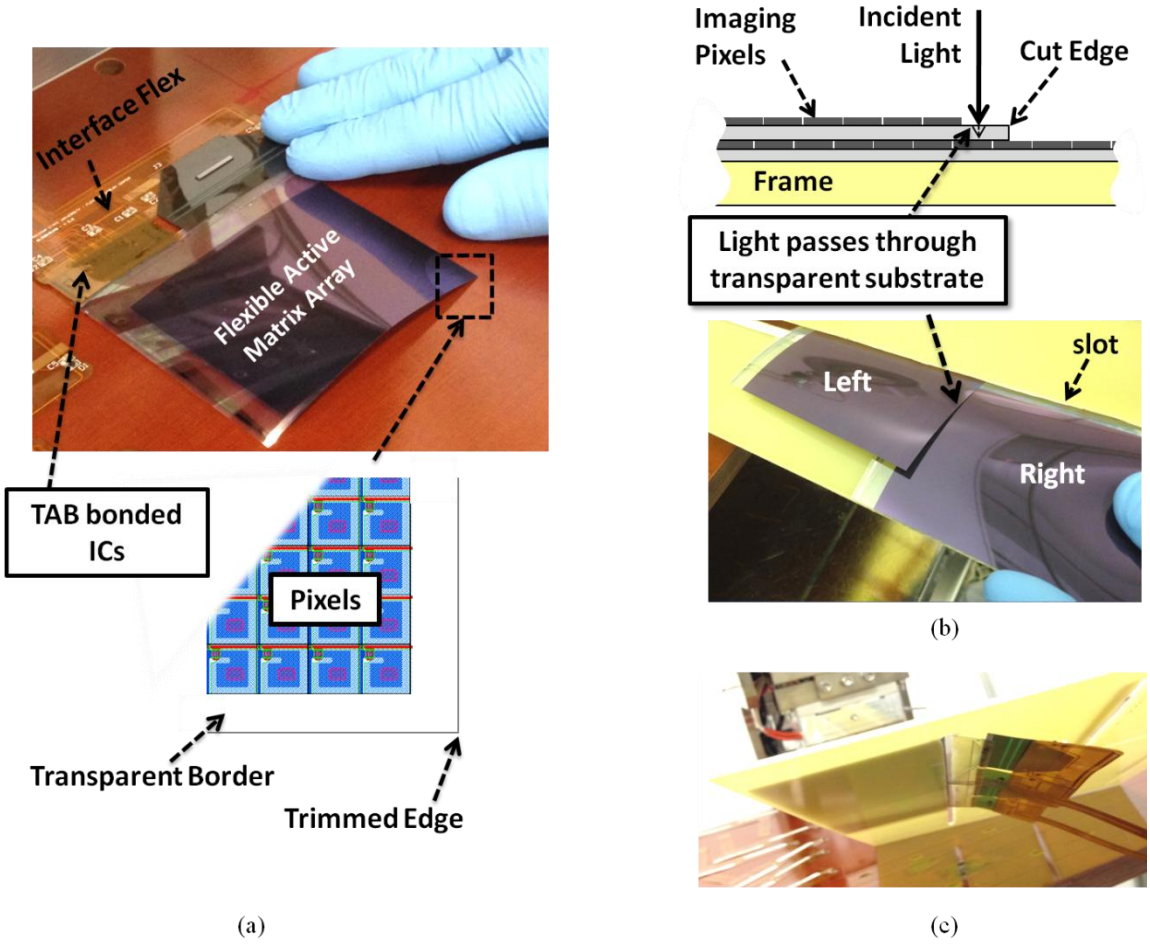

Figure 21. (a) Individual flexible electronic tile after trimming and TAB bonding. (b) Assembly photograph and cross-section drawing illustrating overlap and alignment of the flexible electronic tiles on the support frame. (c) Optical photograph of bottom side of support frame showing the protruding TAB bonded peripheral electronic connections.

External charge-readout and gate-driver CMOS integrated circuits were then ACF bonded to TAB pad connections on the arrays and associated interface flex. At this point, the nine individual flexible tiles are now ready to be inserted into the support frame and overlapped to form the single larger composite array.

To start the top level flexible electronics assembly process, the first flexible tile (right tile in Figure 21b) slides through a slot cut in a support frame, with the TAB connection side with the interface flex passed through first. This enables the electrical connections on the interface flex to extend out of the bottom of the support frame for connection to external drive and readout electronics (Figure 21c). A thin strip of double-sided tape was then used to lock the right flexible tile in place on the support frame. Referring again to figure 2b, the second flexible tile (left) was then inserted the same slot. Optical alignment is performed by sliding the two arrays across each other until the pixels line up along the edge of the two arrays as shown at the top of Figure 21b.

Spare steering pixels in the lower detector array provide adjustability and additional tolerance, as well as simplify locating the final lateral alignment position. In Figure 21b, the left (top) and right (bottom) flexible arrays are able to slide across each other by multiple pixels and still provide a seamless image. Also key, because the plastic substrate is optically transparent, light can pass through the transparent region between the edge of the cut line and the active pixel array of the top detector as illustrated in Figure 21b (top). This feature is used to expose the imaging pixels on the bottom detector to the incident light in the transparent overlap region. This eliminates any nonfunctional or missing lines in the region where two arrays (flexible tiles) overlap. The result is a continuous, optically seamless image.

Also, the PEN plastic substrate (Smith, Marrs, et al. 2013, Lujan and Street May 2012) is thin enough to allow the flexible digital x-ray detectors to be stacked directly on top of each other while still preserving planarity of the top imaging surface as illustrated in Figure 22. Following the same assembly procedures, the remaining seven flexible

electronic tiles were then overlapped and mounted on the same support frame as shown in Figure 23 photograph of the completed assembly. The first flexible tile placed is in the upper left corner. This formed a 3 x 3 composite imaging array mockup from the starting nine individual flexible electronic tiles.

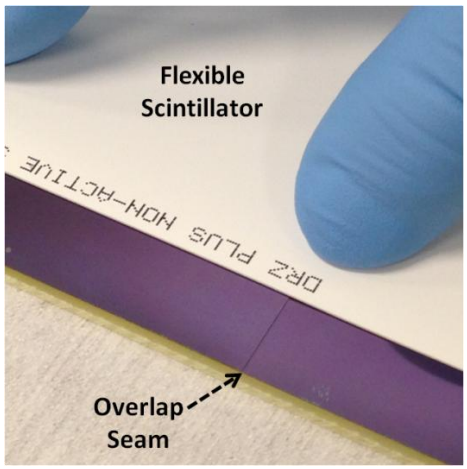

Figure 22. Flexible scintillator pressed against two overlapping flexible electronic tiles.

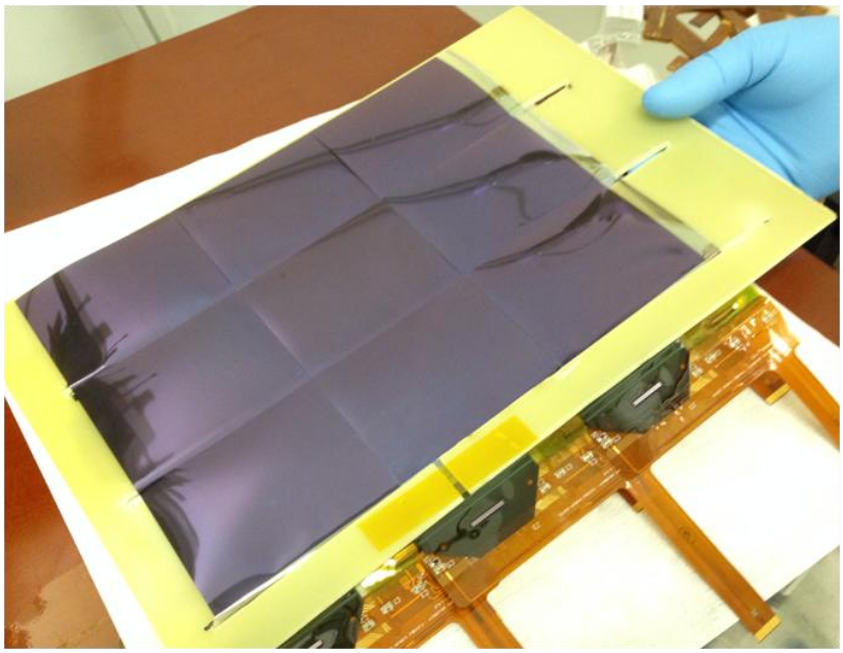

Figure 23. Assembled 3 x 3 composite active matrix array from the nine individual flexible electronic tiles.

In a production prototype, the captured images from the individual flexible tiles would be recombined electronically to form the complete composite x-ray image. Because the original images are not rotated, large, fast-moving scenes, such as those used in continuous fluoroscopy, can be imaged using the flexible-tiling approach without the formation of image artifacts, which can occur when recombining images from mirrored and rotated detector arrays using conventional 4-sided tiling approaches (Powell et al. 1998).

Flexible Electronic Tiling Advantages

Typically, the smaller you can make an active matrix array, the easier it is to fabricate an array with few, or ideally, no line and pixel outs (i.e., zero defects). Hence, a key advantage of tiling is improved manufacturability by reducing the costs associated with fabricating larger, individual x-ray detector panels with few or zero defective lines and pixels. Instead, a number of smaller, but easier and less expensive to manufacture, individual flexible detector tiles can be fabricated and then joined together.

This concept is illustrated by applying the standard Poisson equation for yield modeling (Berglund 1996) to predict the number of defective lines in an x-ray panel as a function of the array resolution (number of rows or lines in the array).

$$Y = e^{-ADo} \tag{13}$$

Where Y is the panel yield at test (% of lines without defects), A is the number of lines (resolution), and Do is the fabrication-related defect density. For example, if 1% of

the lines in a digital x-ray panel with 2048 lines are typically observed to be defective at test, the defect density Do equals 4.90E-06 for A = 2048, and yield Y = 99%, using the Poisson equation above. This value for x-ray panel defect density Do can now be used to predict the number of line outs as a function of decreasing panel resolution (size) using the following equation.

$$Number\ of\ Lines\ out = \#lines - (e^{-ADo} \times \#lines) \quad (14)$$

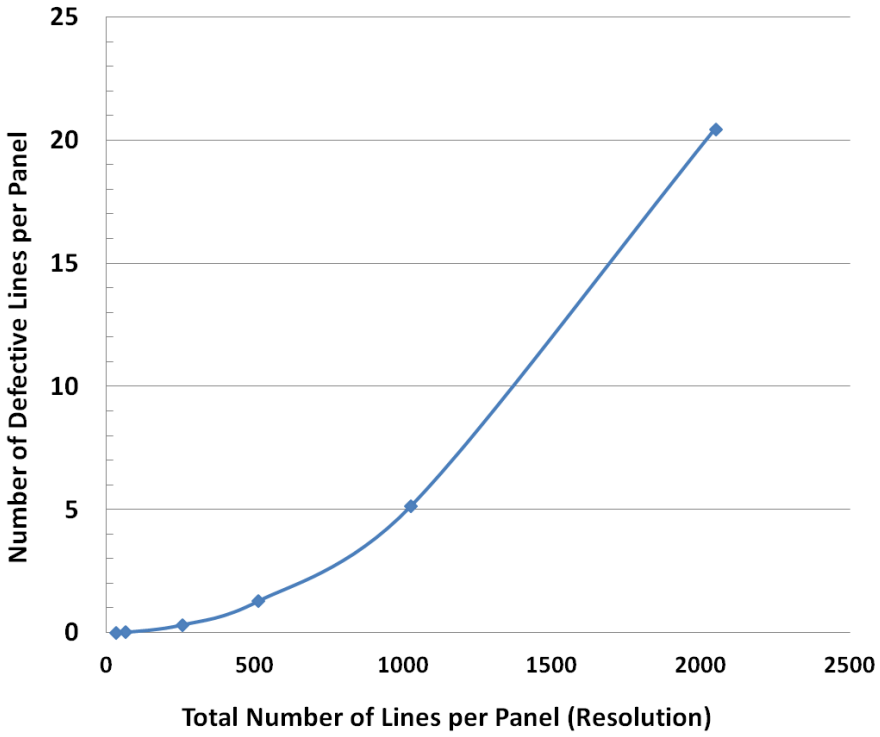

Figure 24. Predicted number of defective lines in a digital x-ray panel as a function of panel resolution (size).

Hence, if 1% of the lines in the larger digital x-ray panel with 2048 lines are typically observed to be defective at test, which translates to 20 lines out, then the

fabricated panel size could be reduced by a factor of 4 using flexible electronic tiling to reduce the predicted number of defective lines to just a single line out per panel at test (Figure 24).

Tiling can also improve x-ray detector sensitivity. This is possible because as the dataline physical length is increased in larger, high-resolution x-ray detectors, the noise associated with the long datalines connected to the charge readout amplifiers begins to dominate the total system noise (Tredwell et al. June 22-28, 2009). Tiling reduces dataline noise by partitioning the detector array into separate, smaller, lower-resolution arrays with proportionally shorter datalines, which are then read out individually using separate independent sets of electronics. These now smaller, lower-resolution x-ray detector arrays result in proportionally lower readout noise.

To illustrate, the dataline noise σ_D for a large digital x-ray detector (Weisfield and Bennett 2001) in electrons (e-) at the input of the dataline charge amplifiers is calculated using the following formula:

$$\sigma_D = \frac{\left[\sqrt{4KTR\Delta f} \times C\right]}{q} \tag{15}$$

where:

Δf = Bandwidth

K = Boltzmans Constant (1.381 x 10^{-23} J/K)

T = Temp (Kelvin)

R = Dataline Resistance

C = Dataline Capacitance

This component of dataline noise is generated by the resistive Johnson-thermal noise in combination with the noise associated with the dataline capacitance. From the noise formula above, the total dataline noise σ_D is a direct function of the dataline resistance (R) and dataline capacitance (C) terms in the equation. Reducing the length of the dataline by using multiple smaller, lower-resolution detector array with fewer pixels per dataline will reduce the dataline noise by proportionally reducing both the dataline resistance and capacitance.

Rows	1920	960	480	240
$R_{dataline}$	2000 Ω	1000 Ω	500 Ω	250 Ω
$C_{dataline}$	100 pF	100 pF	50 pF	25 pF

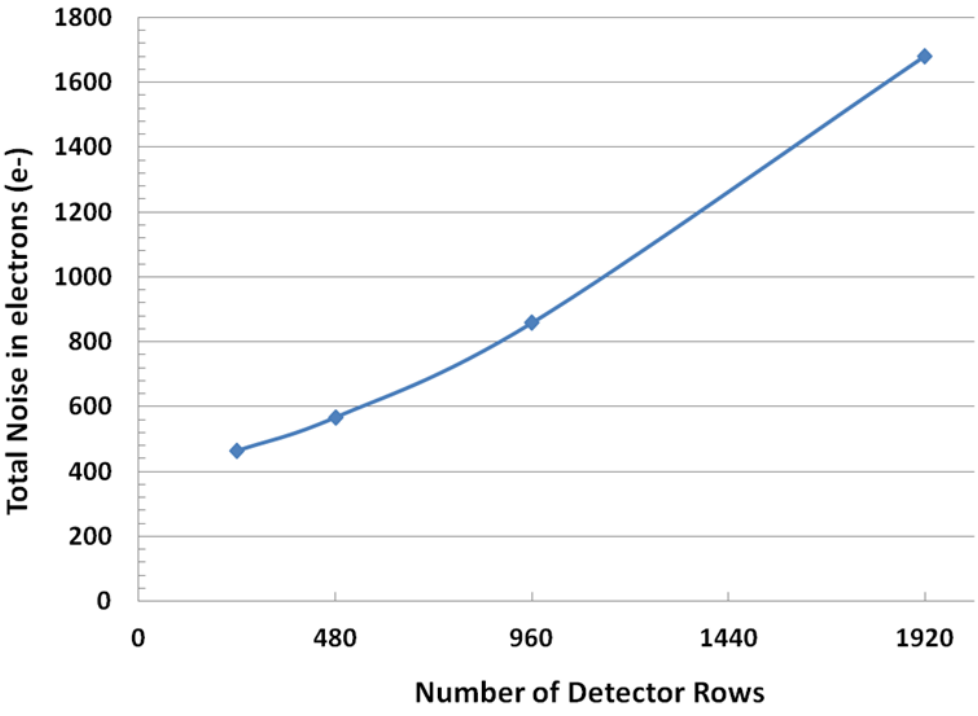

Figure 25. Effect of tiling on the total noise.

For perspective, the reported (Weisfield and Bennett 2001) total readout noise for an x-ray detector with 1920 rows is 1610 electrons (e-). For this larger, high resolution detector, the dataline noise contribution is 1272 e- out of a total 1680 e-. Tiling two half-resolution detectors, each with 960 rows, to form a composite 1920 row array will now reduce the calculated total readout noise from 1680 e- to 858 e-, essentially cutting the total noise in half, using scaled RC parameters (Figure 25) (Weisfield and Bennett 2001). The Rdataline of 2000 ohms was proportionally reduced to 1000 ohms for the half resolution 960 row detector array, and the Cdataline of 100 pF was reduced to 50 pF (Figure 25).

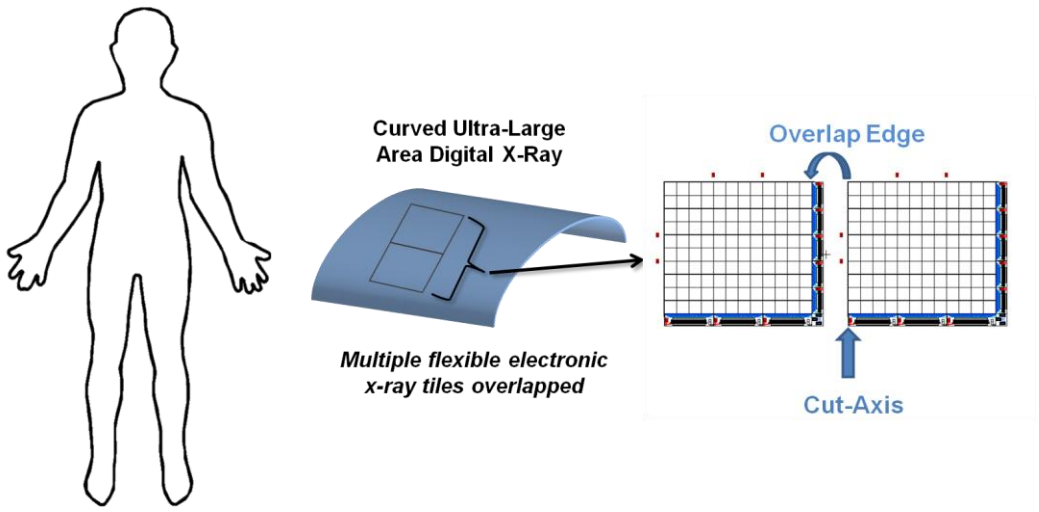

Figure 26. Large-area curved x-ray detector using flexible tiles.

As another benefit, the support frame can function as the radiation shield for the peripheral ACF TAB bonded x-ray detector readout and drive electronics since they are now tucked underneath the support frame in the tiled configuration. This can be an

advantage, especially in high x-ray energy industrial imaging applications, where high energy incident radiation can damage any exposed electronics. Yet another advantage is that if the flexible, overlapping x-ray detector tiles are mounted on a flexible support in combination with a flexible scintillator, the entire x-ray imaging assembly can be curved for ultra-large-area conformal x-ray imaging as illustrated conceptually in Figure 26.

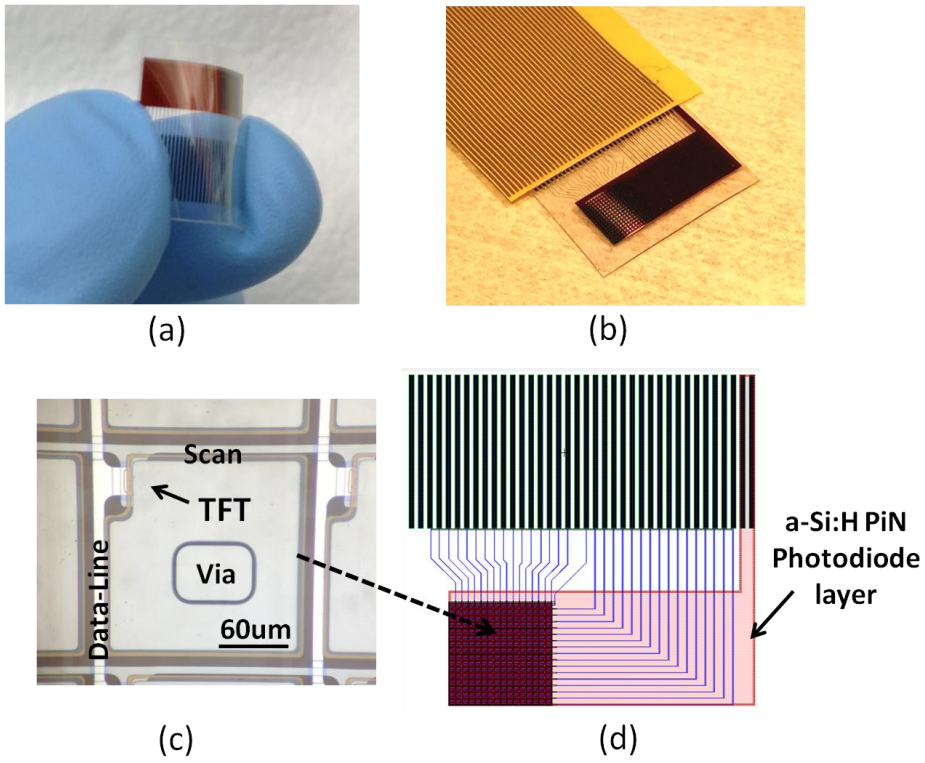

Figure 27. (a) 16 x 16 pixel array prior to assembly, illustrating the transparency and flexibility of the PEN plastic substrate. (b) Photograph of assembled array. (c) Microscope photo of a 207 µm pixel prior to PiN photodiode deposition. (d) Physical design of 16 x 16 array connected to TAB pads.

Tiled Flexible Imaging Array Design and Fabrication

To evaluate the flexible tiling concept, several small 16 x 16 pixel resolution, passive-pixel, active-matrix array prototypes with IGZO MoX TFTs and a-Si:H PiN

photodiodes were manufactured on flexible transparent plastic PEN substrates (Figure 27a). Again, the TFT manufacturing process is similar to what is typically used to manufacture large-area, flat-panel, digital x-ray detectors on glass substrates, but with the glass substrate replaced by a 125µm thick flexible and transparent plastic PEN substrate bonded to a rigid alumina carrier during TFT processing (Raupp, O'Rourke, O'Brian, et al. 2007). The IGZO TFTs in the 16 x 16 pixel array are same n-channel enhancement-mode devices used for the OLED flexible displays (Marrs et al. Oct 2011). The pixel pitch is 209 µm, with a W/L = 20/9 µm sized TFT.

The a-Si:H PiN photodiodes in the test structure uses the full fill-factor structure (Street et al. 2009) described earlier in chapter 2,where the via in each pixel is connected to an isolated molybdenum mushroom metal pad which, in combination with a coincident patterned N+ doped a-Si:H layer, intrinsic a-Si:H, P+ doped a-Si:H, and ITO transparent conductor, form the a-Si:H PiN photodiode (Marrs, Bawolek, O'Brian, et al. 2013). Also, as shown in Figure 27b, the flexible 16 x 16 tiling test structures are designed with connections and patterning on only two sides, enabling the 16 x 16 pixel test structure to be trimmed adjacent to the active pixel array on both of the unpatterned and optically transparent opposing sides—comparable to the 3 x 3 composite array mockup described previously.

Measurement Setup

The flexible 16 x 16 pixel resolution test structures were debonded from the alumina carriers, and the transparent PEN plastic substrates were blade trimmed to within approximately 1 mm from the edge of the active pixel array. The trimmed detectors were

then ACF TAB bonded to a readout interface flex (Figure 27b) and overlapped (tiled) using manual alignment to within approximately five pixels of overlap as illustrated in Figure 28. Closer alignment and trimming tolerances, including fewer overlap pixels, should be possible when using specialized assembly tooling with micrometer-type adjustments combined with a production vision system.

To operate the 16 x 16 pixel arrays, the row lines were connected to Agilent function generators, outputting a 10 ms period, -10 volt to +10 volt square wave, which switched the active matrix array TFTs in the test structure off and on, respectively. A Keithley 428 current amplifier, used for measuring the photogenerated current, was connected between the global PiN photodiode anode terminal for the pixel array and the dataline being monitored. From the Keithley 428, a -5 volts DC reverse bias was applied across the PiN photodiode for the selected photodiode, with the row line asserted by a +10 volt pulse, while the rest of the row lines are held low. Under approximately 0.5 mW/cm2 of uniform white light illumination, steady-state photogenerated currents from the individual a-Si:H PiN photodiodes were then recorded using a Tektronix digital oscilloscope connected to the output of the Keithley 428 current amplifier.

Signal intensity measurements were recorded for each pixel in the 16 x 16 array after the Keithley 428 current amplifier recovered from a temporary saturation condition due to the initial current spike from the TFT channel charge injected immediately after the unselected row lines were turned off (Lemmi and Street 2000). Steady-state mode was used to provide a direct measurement of the photogenerated current from each individual pixel. This allowed the variables that can directly affect optical loss in the

transparent overlap region to be isolated and then compare the steady-state measurements with more realistic measurements using digital radiography.

Optical losses in the transparent overlap region under typical digital radiography conditions were measured separately at GE Global Research by positioning a plastic-substrate flexible digital x-ray array onto a commercial glass-substrate light-imaging array manufactured by General Electric (GE). A Gadolinium Oxysulfide (GOS) doped with Terbium (Gd_2O_2S:Tb) scintillator was then pressed down over both arrays. With this configuration, a series of instrumented digital radiographs were then taken using a Sedecal 8Kw x-ray tube set to 70KV by A. Couture.

Image Capture Results and Discussion

The first series of measurements using the tiled 16 x 16 pixel resolution prototype test structures were taken under uniform white-light flood-exposure conditions, with the photogenerated current recorded for each pixel along 1 data line (Figure 28). Going from left to right in Figure 28, the first 5 pixels (rows 1 to 5) are from the bottom detector and outside the transparent overlap region. The next 6 pixels are also from the bottom detector and are directly underneath the unpixelated transparent plastic (PEN) portion of the top detector where it overlaps the bottom detector. The remaining data (rows 11 to 22) are from the pixels on the top detector.

As shown in Figure 28, very similar photogenerated currents were observed on both the bottom and top detectors outside the transparent overlap region. Underneath the transparent PEN overlap region (rows 5 to 10), the pixel photogenerated current was approximately 85% of the measured current in the non-overlap regions. This reduction

was not unexpected, given the reported total light transmission of 87% for DuPont Teonex® PEN (optically) transparent substrates over 400 to 800 nm (Wong and Salleo 2009).

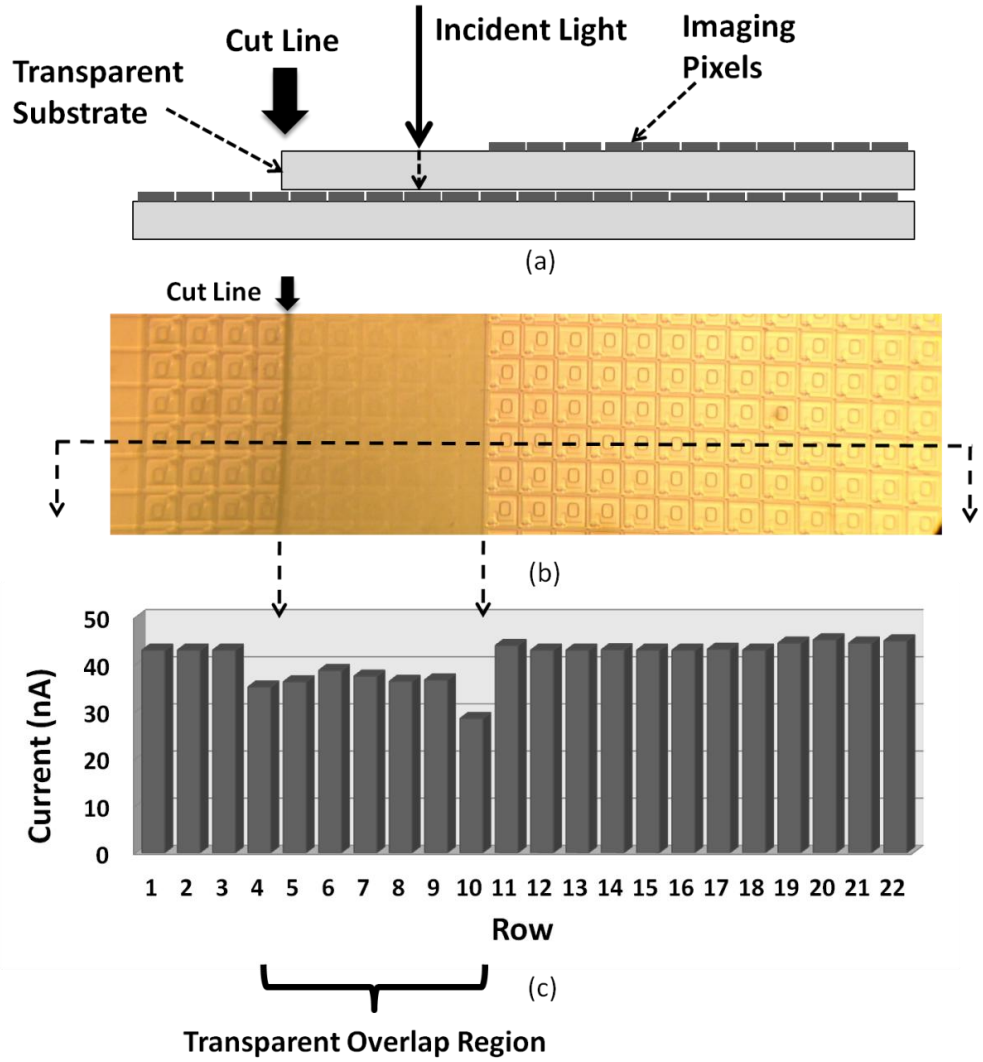

Figure 28. Overlapped 16 x 16 pixel resolution tiling test structures. (a) Cross-section of tiled 16 x 16 pixel arrays. (b) Optical microscope photograph of tiled arrays illustrating the transparent overlap region and cut line. (c) Measured PiN photodiode current of the white light illuminated array from one dataline of pixels. Detected illumination intensity by pixels directly underneath the transparent overlap region is shown to drop by approximately 15%.

The photogenerated currents in the row of pixels adjacent to the cut line (row 5), but not directly underneath the transparent layer, were also reduced by approximately 15%. This is likely due to the somewhat ragged nature of the cut line at the microscopic level, which scatters incident light. Although it is not shown well in the Figure 28 photo, the row 10 pixel in the bottom detector was partially blocked by the pixels (row 11) directly above it. This imprecise alignment and lack of precision in trimming resulted in an additional 5% loss in the detected current for this single row. Ideally, the distance of the cut edge to the top active pixel (patterned) array would be an even multiple of the pixel pitch, which would position the cut edge directly over the intersection between adjacent pixels. The edge of the top pixel would then be aligned precisely with the edge of the pixel directly underneath.

Next, a static 2-d optical image was captured using a dart-shaped opaque test pattern placed directly on the surface of the overlapping 16 x 16 pixel imaging test structures. The reconstructed grayscale image, along with a false color version, is illustrated in Figure 29, with the two images vertically aligned and approximately scaled to the original microscope photograph (Figure 29a) of the illuminated test configuration. As evident in the figure, the false color representation appears to provide a better illustration of the overlap related losses as well as highlight the approximately 15% lower photogenerated current detected in the pixels directly underneath the transparent overlap region. The grayscale image only shows a slight gray shade transition, but does represent a closer representation of the reconstructed image as it would be displayed on a monitor.

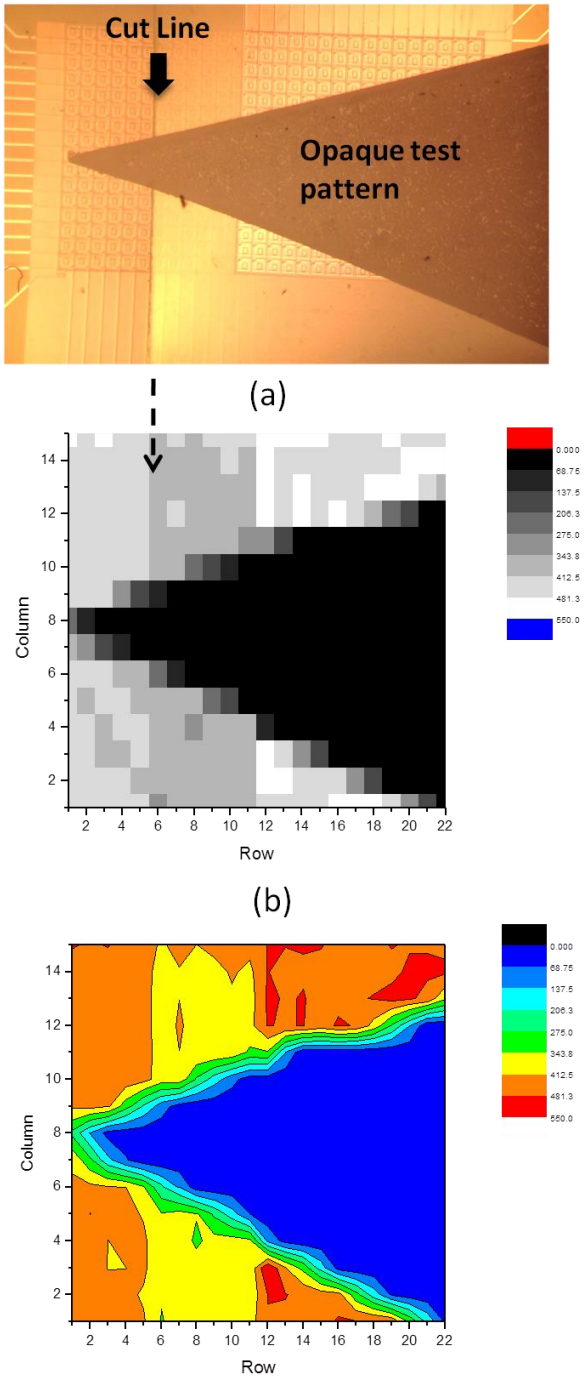

Figure 29. Optical test results for tiled 16 x 16 pixel test structures. (a) Optical microscope photo of tiled 16 x16 pixel resolution detectors with light-blocking, dart-shaped test pattern. (b) Grayscale reconstructed visible light image illustrating the ~15% difference in detected illumination intensity underneath the transparent overlap region. (c) Alternate false color representation of the reconstructed visible light image.

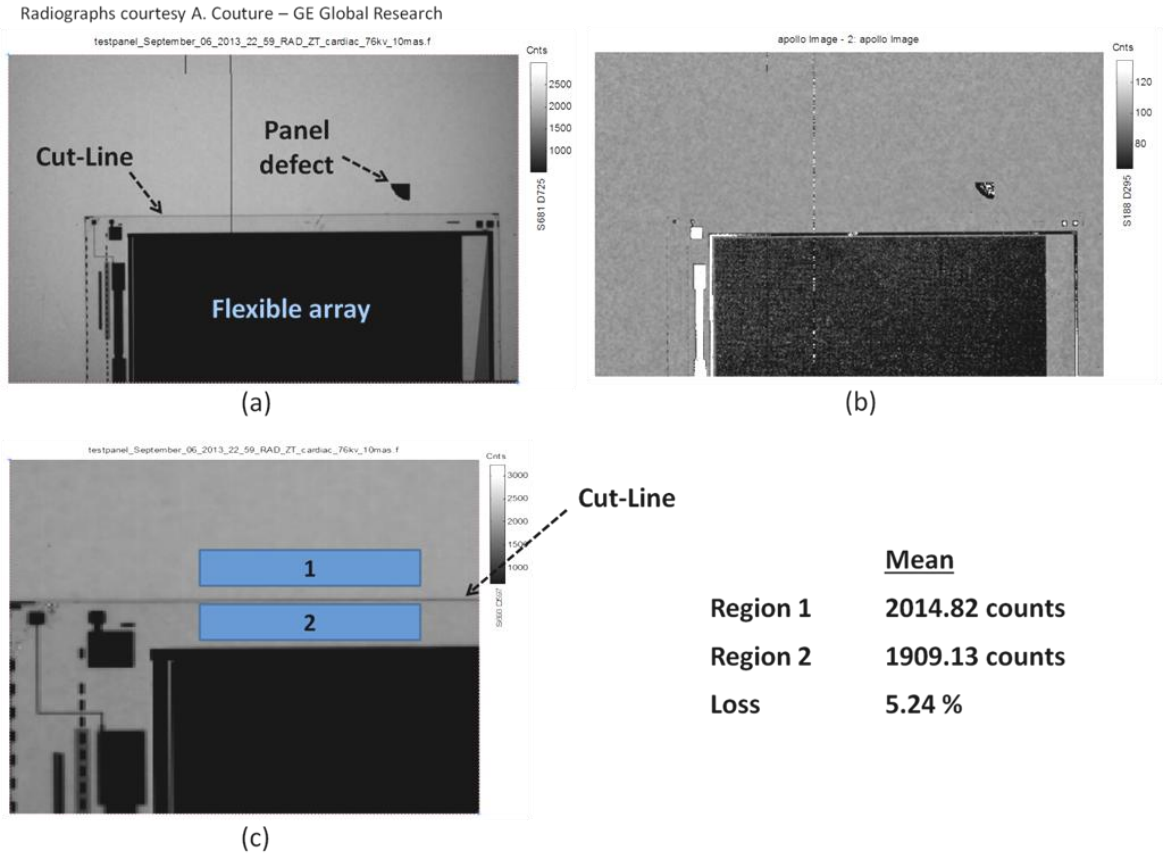

Figure 30. Digital radiographs of flexible active matrix array pressed up against surface of digital x-ray imager. (a) Initial un-calibrated digital x-ray image of the non-functional plastic substrate flexible x-ray detector placed directly on the surface of a glass substrate cardiac light imaging array. (b) Same digital x-ray image after gain calibration illustrating removal of overlap seam imaging artifact. (c) 12 x 82 pixel locations on the light imager used to determine the optical signal loss through the transparent plastic substrate. Results show a mean reduction of 5.24%.

Next, digital radiographs were generated with a non-functional plastic PEN substrate flexible x-ray detector placed directly on the surface of a 200um pixel pitch GE light imaging array. A commercial GOS scintillator screen was then placed on top of the flexible substrate and light imager, and the two arrays plus scintillator were then pressed tightly together. The first digital radiograph image captured from this assembly is shown

in Figure 30a. Looking at the center of the Figure 30a image, the location of the approximately 1-pixel-wide cut line on the upper flexible x-ray detector is clearly visible. This first image (Figure 30a) has only been offset (dark) corrected, and has not been gain calibrated. Figure 30b is the same digital radiograph image after applying gain calibration, illustrating removal of overlap seam imaging artifact from both the cut line as well as the entire transparent overlap region. The background noise observed in Figure 30b is an artifact of the approximately factor of 10 reduced scaling range as compared to the Figure 30a digital radiograph.

In Figure 30c, the results and digital radiograph measurement locations using the light-imaging array to estimate the optical signal loss through the transparent region are illustrated. Region 1 and region 2 are 12 x 82 pixel regions of array. In region 1, the GOS scintillator is in direct contact with only the GE imaging array, and in region 2, the GOS scintillator is in direct contact with both the flexible substrate that has been placed on the surface of the light imaging array and the GE imaging array. As illustrated in Figure 30a and Figure 30c, region 2 is an unpatterned transparent portion of the flexible array. This allows the optical signal loss through just the flexible PEN plastic substrate to be calculated by subtracting the mean measured signal (counts) in region 2 from region 1 which, as shown in Figure 30, is only a 5.24% loss. Interestingly, the measured signal loss using this method was 10% lower (better) than the 15% loss reported earlier using the optical (white light) measurement setup. This indicates that the combination of the scintillator and the transparent plastic substrate enhances or increases the detected optical signal by the underlying x-ray imaging array and more importantly, represents the expected performance in an actual x-ray imaging system, as opposed to the previous

direct optical loss measurements, which were taken without a scintillator. One possible explanation for the enhanced measured signal level is constructive optical interference between the deposited thin film layers and the PEN substrate, the PEN substrate itself, and the scintillator layers.

Medical Imaging Applications

The primary medical imaging application is expected to be single-exposure, low-dose, large-area digital radiography for gapless x-ray imaging of large anatomic regions including neck and chest, full-torso, full-leg, and full-spine. One specific large-area x-ray imaging application is primary full-body digital radiography for detecting injuries to the chest, thoracolumbar spine, and pelvis in trauma patients admitted to an emergency room.

Another interesting potential, albeit conceptual, medical imaging application for tiled flexible x-ray imagers is 3-D digital computerized tomography, in which applying the flexible tiling concept may offer improved imaging resolution. Digital tomosynthesis is a 3-D computed tomography technique that currently uses a single, rigid, flat-panel digital x-ray detector. In operation, the single x-ray flat-panel is mechanically repositioned around the patient to capture a series of x-ray images, which are then electronically recombined to form a composite 3-D x-ray image (Dobbins June 2009). Certain medical diagnostic x-ray imaging applications—such as mammography—can require high imaging resolutions that approach 50 μms (Taghibakhsh and Karim 2008).

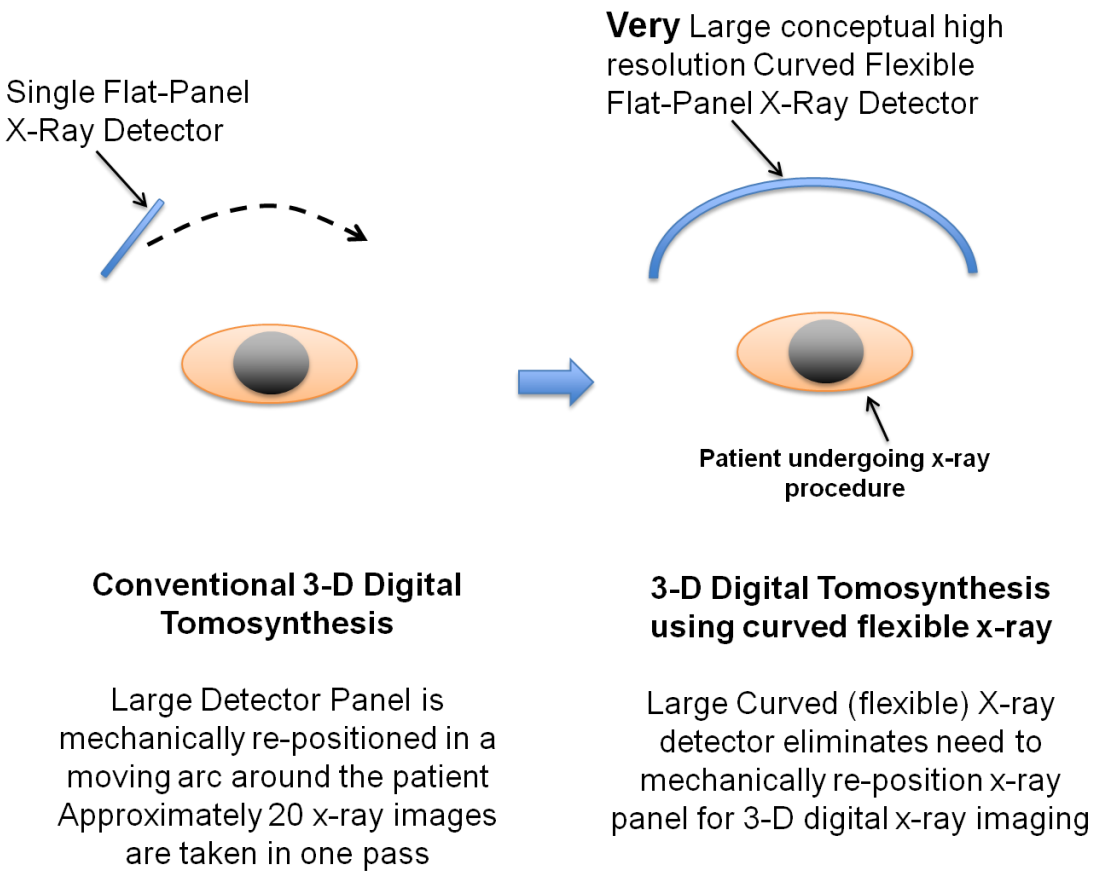

Figure 31. Flexible tiling concept for 3-D digital tomosynthesis imaging.

If the mechanically repositioned, rigid flat-panel x-ray detector is unable to provide this level of precision, a single, large, high-resolution curved digital x-ray imager could be used. If the size of the x-ray imaging array approaches the size of the patient and can be curved or wrapped around the individual, the now large and curved x-ray imager will not have to be mechanically rotated or moved during the diagnostic procedure. Instead, the high-resolution 3-D tomographic image would be taken by rotating only the x-ray source around the patient (Dobbins June 2009), while the large curved x-ray imager and the patient are held stationary. Admittedly, this imaging concept is speculative, but it demonstrates that new x-ray imaging techniques and medical diagnostic configurations

become possible if the ability to curve or bend to digital x-ray detectors is added, in combination with the ability to make x-ray detector arrays quite large.

Summary

Using prototype flexible x-ray detectors and a commercial x-ray imaging array, the feasibility and performance of a method to seamlessly tile flexible, digital x-ray detectors to create a larger, composite, digital x-ray detector without missing pixels was demonstrated. The described approach has the ability to scale up to extremely large digital x-ray imaging arrays for such medical imaging applications as single-exposure, low-dose, full-body digital radiography, or possibly even 3-D digital tomosynthesis using a large, curved, digital x-ray imager.

CHAPTER 4

ADAPTIVE X-RAY IMAGING

X-rays…I am afraid of them. I stopped experimenting with them two years ago.

Thomas Edison

This chapter presents a new approach to increase the sensitivity of digital x-ray detectors by increasing the signal-to-noise ratio (SNR) of the detected signal. The improvement is achieved using a method to reduce the background-noise level at the input to the digital x-ray charge readout amplifiers. This method works by recognizing that, in some medical imaging scenarios, the object or region of interest that needs to be x-rayed may only cover a fraction of the entire x-ray detector array. In this scenario, the detected image signal during charge readout includes extra and undesired noise from TFTs in the unused portion of the x-ray detector array. For these applications, it is possible to improve the detected image sensitivity by selectively disabling the rows in the TFT active matrix array that are not part of the region that needs to be imaged during charge readout. The adaptive x-ray imaging method reduces the detected noise at the input to the readout charge amplifiers from these used regions by re-configuring or adapting the x-ray detector to capture only what needs to be imaged.

Adaptive Digital X-Ray Imaging Fundamentals

As illustrated in Figure 32, the new approach is designed to work in x-ray imaging applications where the object or region needing to be x-rayed covers only a

portion or fraction of the active x-ray detector array. This is important because detection sensitivity is directly proportional to the SNR at the input to the peripheral digital x-ray charge amplifiers described in chapter 2, with lower noise σ translating into higher sensitivity.

$$V_{detected} = V_{signal} + \sigma_{noise} \quad (16)$$

As shown in Figure 32, the unwanted signal from the region of the detector array outside of the region of interest will consist only of noise. However, using a standard, passive-pixel x-ray detector architecture, the signal at the input to the charge amplifiers connected to each dataline will include both the noise from these outer unused or unwanted regions, as well as the region of interest.

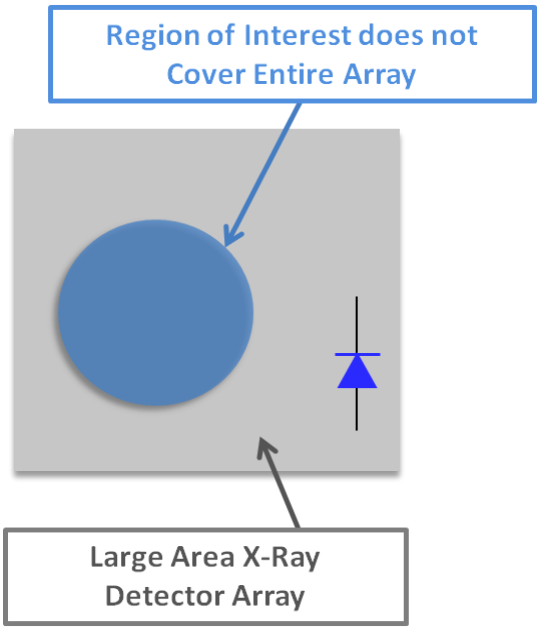

Figure 32. X-ray imaging regions.

The adaptive imaging method is designed to reduce the detected noise at the input to the charge amplifiers from these outer and used regions by adapting the detected image to include only the regions that need imaging, and disabling the rest of the array. The result is the ability to detect lower level signals from only the region of interest, and thus improve x-ray detector sensitivity.

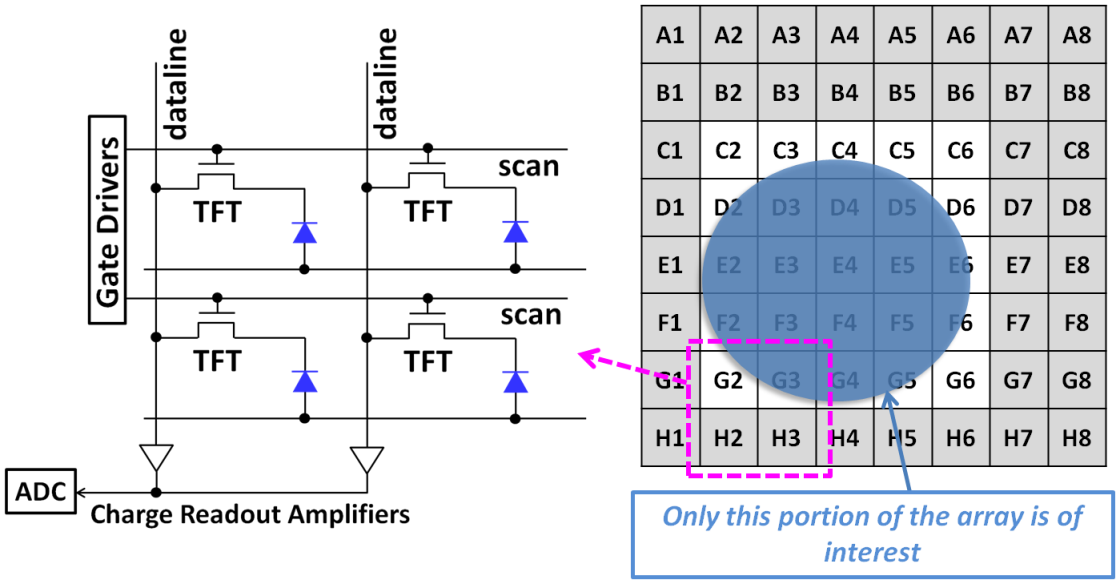

Figure 33. Adaptive imaging concept schematic using small active matrix array.

This relatively straightforward new concept is illustrated using the simple active matrix TFT array schematic for a digital x-ray imager in Figure 33. As shown in the figure, the region of interest only covers a fraction of the entire conceptual 8 x 8 pixel imaging array (rows C to G and columns 2 to 6). The pixels in rows A, B, and H, along with columns 1, 7, and 8, are effectively unused and outside the active region. These unused x-ray detector pixels have been shaded to help graphically illustrate which pixels

would need to be isolated from the external charge readout amplifiers. However, it should be pointed out that in an actual detector array, the resolution would be much larger than the simple 8 x 8 example active matrix array, typically greater than 1000 x 1000 pixels.

Zooming in to the exploded 2 x 2 grouping of pixels in the lower left corner of the partial detector array, each x-ray pixel again consists of an a-Si:H PiN photodiode and a TFT switch. As described in chapter 2, the TFT electrically connects the photodiode to the dataline when the scan (row) line is asserted. As shown in the figure, the bottom row H in the 2 x 2 zoomed region is outside of the region of interest, while row G, directly above, is in the active area. Hence, a portion of the detected signal on the dataline at the input to the charge readout amplifiers from row H, as well as rows A and B, is unwanted noise.

Noise from Transient TFT Leakage Currents

One of the noise components in these unused rows is shot noise caused by a time varying (transient) leakage current from off-state TFTs (Powell 1989). Essentially, when a TFT is turned off, it actually does not turn off immediately; instead, the TFT injects a time-varying charge signal directly onto the parallel datalines during the sequential readout of the array (Lemmi and Street 2000). This charge-emission-induced leakage current from the off-state TFTs is caused by the detrapping of electrons from deep states in the bandgap of the TFT's active (semiconductor) device layer at an emission rate determined by their energy depth (Powell 1989). Depending on the size and resolution of the x-ray detector, several hundred to several thousand off-state TFTs can be connected to a single dataline. Hence, any additional charge introduced onto a dataline from these

off-state TFTs during readout will result in a dark-state voltage offset at the output of charge integration amplifiers connected to each dataline (Lemmi and Street 2000). Additionally, the random variation in the charge-emission leakage current also increases the shot noise in the amplified signal of the detected image.

Measurement and Analysis of TFT Transient Leakage Currents

To gain an understanding of the magnitude of the charge-emission-induced transient leakage currents for both IGZO and a-Si:H TFTs, test structures were designed to emulate a portion of a typical x-ray detector dataline. This allowed for an accurate estimation of the transient leakage current, comparable to what would be found in an actual x-ray detector array. The IGZO and a-Si:H TFT test structure used for this work is shown below (Figure 34), configured as a large, parallel array of 126 individual TFTs, each with a W/L = 96/9 µm.

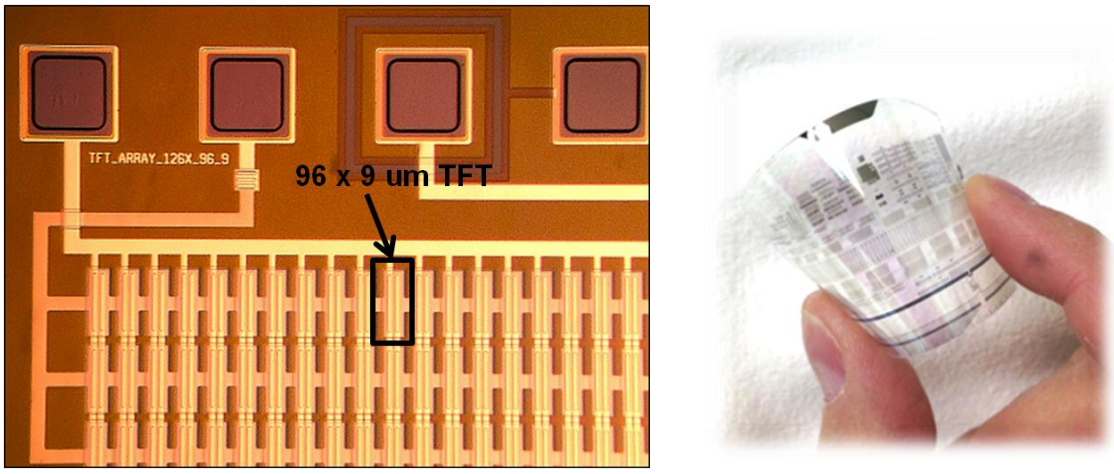

Figure 34. 126 x 96/9 µm parallel array TFT test structure and test pads.

The combined (total) TFT width of approximately 12 mm in the test structure ensures that observed TFT thermal emission current levels are well above the instrumentation noise floor, and provides a TFT test structure area sized to approximately 5 to 10% of a typical single x-ray detector dataline. The results were then normalized to μm^2 by dividing the transient leakage current by the active semiconductor device area of [126 x (120 µm x 41 µm)], which accounts for the detrapping of charge from the entire active device area as opposed to just the 96/9 µm channel region.

For the transient emission current measurements, the TFT source and drain electrodes were both connected to the input of a Keithley 428 current amplifier. A +5 volt to -10 volt square wave was then applied to the TFT gate electrode. +5 volts on the gate turns on the TFT and pulls charge (electrons) into the active channel, where they are trapped in deep localized states. -10 volts is then applied to the gate electrode to turn off the TFT. At the instant of being turned off, the channel charge (electrons) immediately exits the TFT drain and source terminals, which causes a brief current spike at the input to the Keithley 428 amplifier. This brief current spike is then immediately followed by the time-varying transient thermal emission of trapped electrons from their deep states (the signal of interest). The thermal emission TFT leakage current was then recorded using a Tektronix digital oscilloscope connected to the output of the Keithley 428 current amplifier, after the current amplifier recovered from a temporary saturation condition due to the initial current spike from the TFT channel charge. This issue, and the approximately 10 order of magnitude difference between the thermal-emission-leakage currents and initial channel charge current spike, bracketed the measurement window to between approximately 2 msec and 100 msec. Below 2 msec, the current Keithley 428

amplifier was still saturated from the initial channel charge spike; above 100 msec, the observed thermal emission current level dropped below a detectable threshold using the described test instrumentation.

TFT Measurement Results and Discussion

The measured transient thermal emission leakage currents for both a-Si:H and IGZO TFTs on PEN plastic substrates from identical test structures are illustrated in Figure 35, where:

$$I_{\text{transient}} = \frac{V_{\text{out}} \times \frac{1}{gain}\left(\frac{A}{V}\right)}{TFT\ active\ area\ (um2)} \tag{17}$$

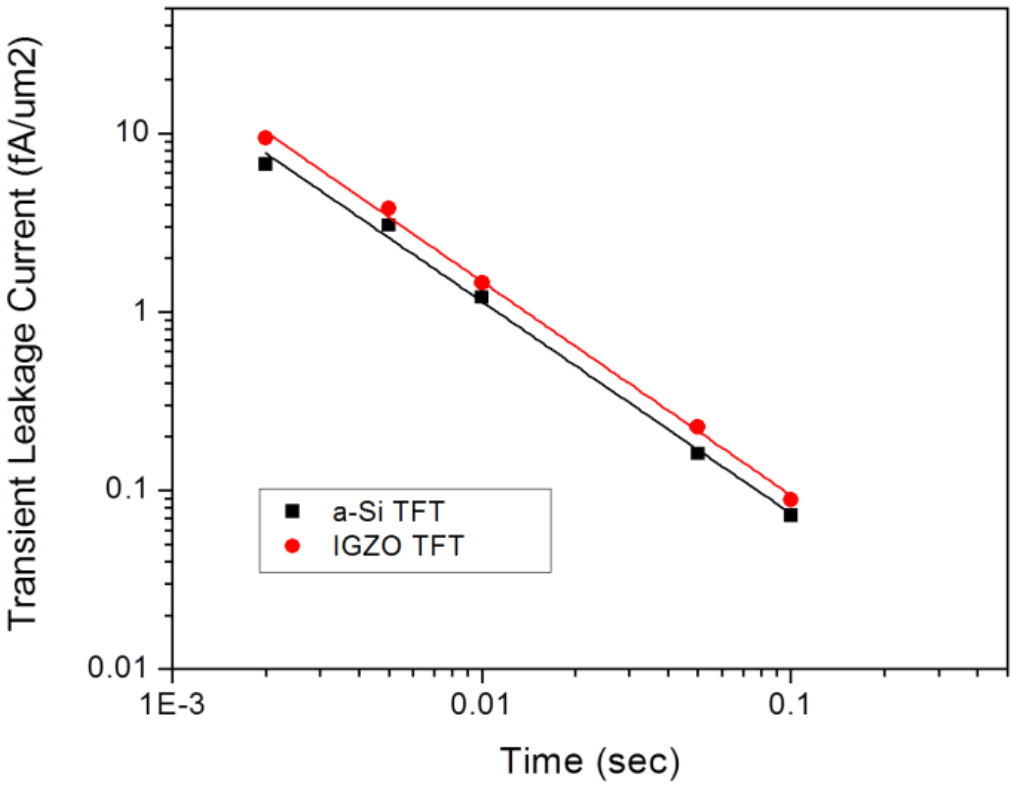

Figure 35. Transient TFT thermal emission charge detrapping leakage currents.

From Figure 35, the observed TFT transient leakage currents decay in a 1/t power law-like behavior over approximately two decades after switching off the TFTs, indicating a uniform density of states in the band gap as the charge is thermally emitted from traps in these deep states (Zelakiewicz et al. 2005). The transient leakage current for the IGZO TFTs was approximately ~1.3X higher than the a-Si:H TFTs. At this time, there is no explanation why the IGZO emission current is higher. The assumption is the IGZO trap density is higher than the a-Si:H TFTs.

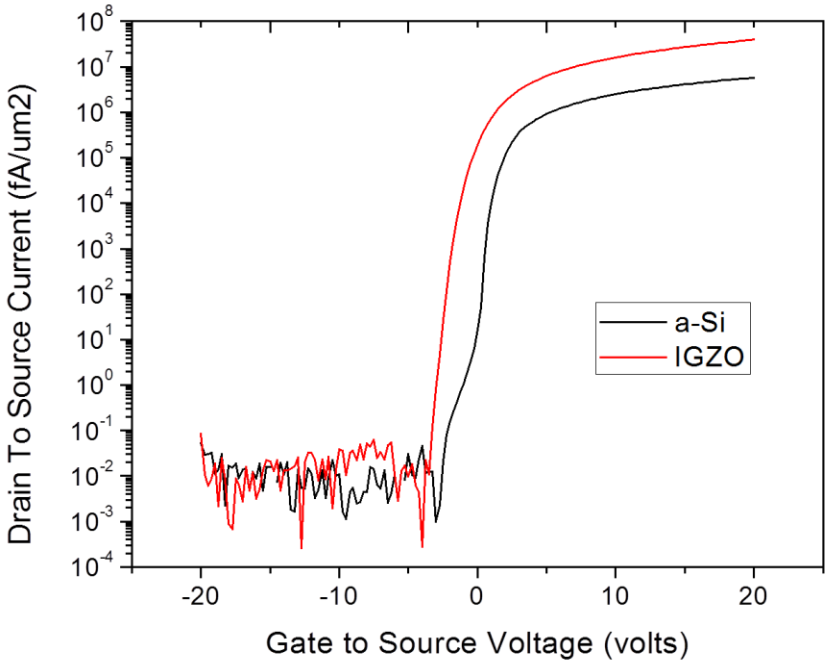

Figure 36. Static DC transfer characteristics (Vds = +1 v) of a-Si:H and IGZO TFTs fabricated on PEN plastic substrates with the drain current normalized to fA/um^2. IGZO TFT mobility and off current is approximately 10X a-Si:H.

From this data, an interesting comparison can be made by mathematically projecting the observed transient thermal emission current to its predicted value after

several seconds, which correlates to the approximate time required for a semiconductor parameter analyzer to measure the static DC leakage current. Not surprisingly, both the mathematically projected TFT transient emission current and the measured static leakage current (Figure 36) are approximately equal after several seconds, and are in the range of ~0.01 fA/um^2 at Vgs = -10 V. This comparison helps underscore that TFT off-state leakage currents in the sub-1 sec typical digital x-ray detector operating conditions are in reality both time varying and, more importantly, orders of magnitude higher than predicted by conventional static DC leakage measurements. For example, in a typical x-ray fluoroscopy imaging application, the digital x-ray detector needs to operate at video-frame rates, which requires the array to be readout every 0.033 sec for 30 fps operation.

$$\tau_{readout} = 1/fps \tag{18}$$

From Figure 35, the leakage current when reading out at 0.033 seconds is approximately two orders of magnitude higher than the current if it is read out after 1 second. Hence, to reduce the noise level at the input to the digital x-ray charge amplifiers, it would be advantageous to turn off (disable) any unused rows for at least 1 second before reading out, and reconstructing the x-ray image from the active portion of the TFT active matrix array.

Contribution of Transient Leakage Current to Detector Shot Noise

The contribution of the TFT transient leakage (off) current to the detector shot noise σ_s is calculated using the following expression.

$$\sigma_S = \sqrt{\frac{\int I_{off}(t)dt}{q}} \quad (19)$$

where $\int I_{off}(t)dt = I_{leak} \times t_{integration} \times \#rows \times TFT\ active\ area$ (20)

For an x-ray fluoroscopy detector with 2048 rows, a 30 fps readout rate, a 10 µs integration time, a 96 x 9 µm TFT (120 x 41 µm active area), and a 1.5 fA/um^2 pixel TFT transient leakage current (measured data from Figure 35), the predicted shot noise σ_s is 972 e$^-$. This assumes a sampling point at 0.015 sec for 30 fps operation, which averages the switching activity of the TFTs in one frame period.

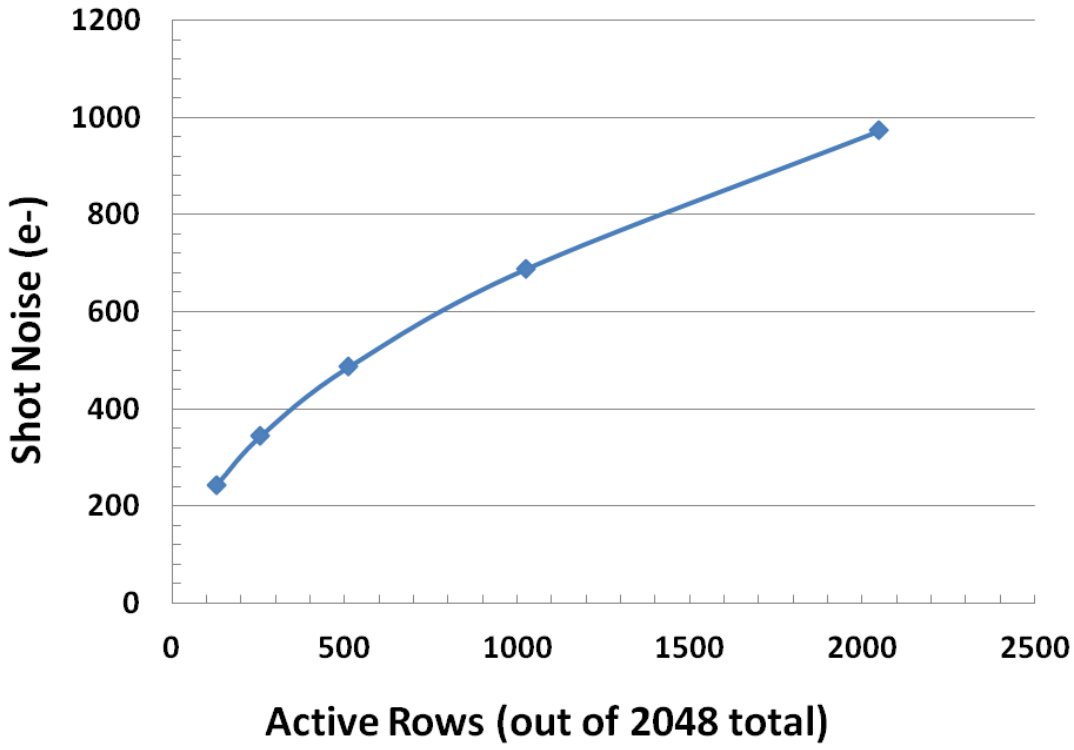

Figure 37. Detector shot noise in electrons (e-) as a function of the number of active detector rows.

Assuming an x-ray imaging scenario where one-half of the rows in the 2048 row array could be selectively turned off, the shot noise component would now drop by approximately 285 e^- , as illustrated in Figure 37. This translates to a reduction in overall reduction in system noise by approximately 7%. This analysis assumes that the shot noise σ_s is one-fourth of the total detector noise in a typical passive pixel x-ray detectors (Tredwell et al. June 22-28, 2009).

$$\%\, reduction = (\sigma_{2048\, rows} - \sigma_{1024\, rows}) \,/\, (\sigma_{2048\, rows}\ x\ 4) \qquad (21)$$

A lower noise level at the input of the charge amplifiers will now allow the x-ray imager to detect slightly lower-level or weaker signals captured on the pixel PiN photodiodes in the region of interest that might otherwise be swamped out by the shot noise from the unused rows, improving x-ray detector sensitivity. Lower noise could also allow the x-ray source to be operated at a slightly lower energy level during diagnostic procedures to reduce patient radiation exposure.

Conceptual Adaptive Digital X-Ray Imager

A conceptual, simplified, array schematic for an adaptive digital x-ray detector is illustrated in Figure 38. To add adaptive imaging to a standard x-ray detector, all row lines are multiplexed internally and controlled by an integrated row disable decoder. In the operational example shown in the same figure, Row 2, which falls in the area selected for imaging, is set to operate normally via the external control signal applied to the row

disable decoder. This connects the row 2 gate line to the standard row driver circuit block (green path). In parallel, the same external control signal applied to the row disable decoder also disables, or turns off, rows 1 and 3 by connecting both of the disabled row lines to -10 volts (red path) using the multiplexers connected to the input of each row line. With this approach, the TFT transient off-state leakage currents from the rows 1 and 3 TFTs, which are connected to the same dataline as row 2, are now reduced by approximately two orders of magnitude after ~1 second.

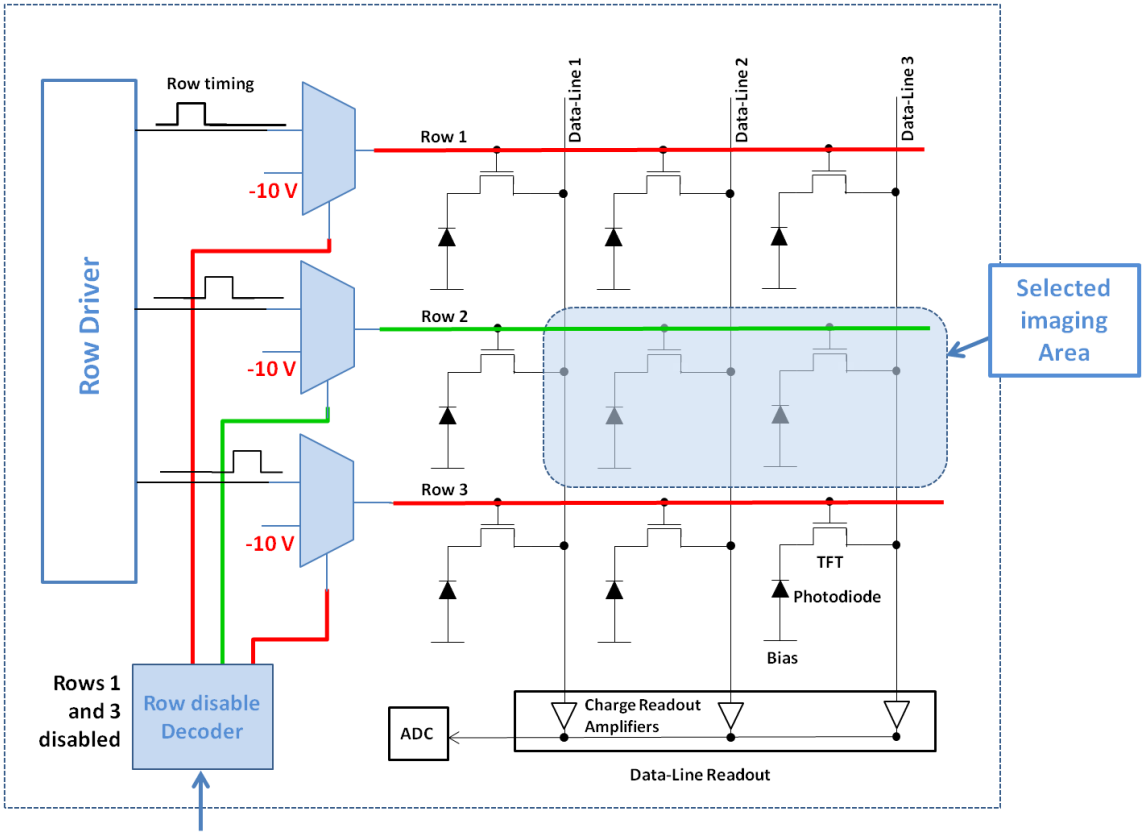

Figure 38. Adaptive imaging capability integrated into digital x-ray active matrix array.

To configure or select the region of the x-ray detector for imaging, one conceptually straightforward method would be to start the x-ray diagnostic procedure, after which the user could perform the equivalent of circling or highlighting the region of interest on the displayed x-ray image—equivalent to manually zooming in on a computer screen with a mouse. Computer processing would identify when rows to selectively disable and the corresponding digital signal would then be applied to the integrated row disable decoder input.

Alternatively, the detector array could initially run through an automated configuration sequence, where each pixel is individually addressed and read out. A signal-processing algorithm would then be applied to determine the illumination state for each of the sampled pixels. After the entire detector array is sampled, only the active, illuminated portions of the array would be enabled, and the unused rows would be disabled. This approach is likely viable for diagnostic procedures where the object to be x-rayed covers only a small portion of the entire detector array, such as a hand or arm. Also, it is assumed that this sampling sequence would be repeated periodically during typical operation, albeit at a very small percentage of the overall signal duty cycle. The enabled portion of the pixel array would now actively "adapt" to a potentially spatially variable or moving image—hence the term adaptive imaging for this concept. At startup, a short-duration, low-energy x-ray flash is required initially, followed by signal processing to determine which rows to selectively disable before capturing the image. This may slightly increase patient x-ray radiation exposure for a digital radiography procedure in which only a single x-ray image is required. However, for medical imaging procedures during which the x-ray is on continuously, such as fluoroscopy, when the

diagnostic procedure can run several minutes, a small additional dose at the beginning is insignificant compared to the total dose received by the patient during the entire procedure.

Summary

This chapter presented a new approach to increase the sensitivity in digital x-ray detectors by reducing the background noise level at the input to the digital x-ray charge readout amplifiers. The new method recognizes that in some medical imaging scenarios, what needs to be x-rayed may only cover a fraction of the entire x-ray detector array. Hence, the detected signal during charge readout includes extra and undesired noise from TFTs in the unused portion of the x-ray detector array. It was shown that is possible to improve the detected image contrast by selectively disabling the rows in the TFT active matrix array that are not part of the region to be imaged using a straightforward procedure.

CHAPTER 5

FLEXIBLE INTEGRATED ISFET BIOSENSORS

In biology, nothing is clear, everything is too complicated, everything is a mess, and just when you think you understand something, you peel off a layer and find deeper complications beneath.

Richard Preston, *The Hot Zone*

According to the published IUPAC definition (Thevenot et al. 2001), "a biosensor is a self-contained integrated device which is capable of providing . . . analytical information using a biological recognition element which is in direct spatial contact with a transducer element." One well known integrated biosensor is the ion-sensitive field effect transistor (ISFET) biosensor, which measures the pH of an electrolytic solution using a sensor layer integrated on the same substrate with a read out transistor. However, up until now, ISFET biosensors have only been produced on fragile substrates−typically glass or silicon−which poses a problem in sensing applications such as the food industry or water-quality monitoring, where the use of fragile substrates is problematic. Additionally, ISFET biosensors implanted inside the human body or applied to the skin surface need to be both shatter proof and mechanically compliant.

As a solution to these limitations, this chapter presents a new shatterproof and flexible ISFET biosensor using active matrix TFT technology that can be fabricated using conventional TFT display process technology. The core of the new flexible biosensor approach is again replacing conventional fragile substrates with a flexible PEN plastic substrate, with just the TFT active matrix array superstructure optimized for biosensing

(Smith, Shah, et al. 2013). The methodology is comparable to the superstructure personalization described in Chapter 2, where a flexible display was converted into a flexible digital x-ray detector by only modifying the upper thin film process layers. The process modifications required for biosensing, and the new flex ISFET experimental results are the focus of this chapter.

Background

The ISFET is well established as a pH sensitive biosensor (Bergveld 2003a), and biochemical sensing is also possible if a biological recognition material is immobilized on the ISFET gate-sensor surface (Schoning and Poghossian 2002). As illustrated in Figure 39, the ISFET is essentially a conventional MOSFET in which the gate electrode has been replaced by an electrolytic solution and a separate reference electrode. In operation as a pH biosensor, the gate dielectric layer over an active semiconductor channel region in an ISFET is brought into direct physical contact with the electrolytic solution to be measured. Electrically active ions, such as hydrogen (H+), from the electrolyte are then directly absorbed onto the surface of a sensitized dielectric sensor layer. The charge from the absorbed H+ ions is then able to modulate the conductivity of the active semiconductor channel underneath the dielectric sensor layer. The greater the absorbed charge on the gate (sensor) electrode's surface, the greater the change in device conductivity (Lee, Kim, and Kim 2009). The effect is similar to applying a small voltage bias to the gate of a conventional MOSFET, which also changes the device conductivity. For example, as the pH of the solution is decreased (made more acidic), more hydrogen

H+ ions from the electrolyte solution are available to bond to the exposed gate dielectric (sensor) layer, creating an increasingly positively charged surface layer.

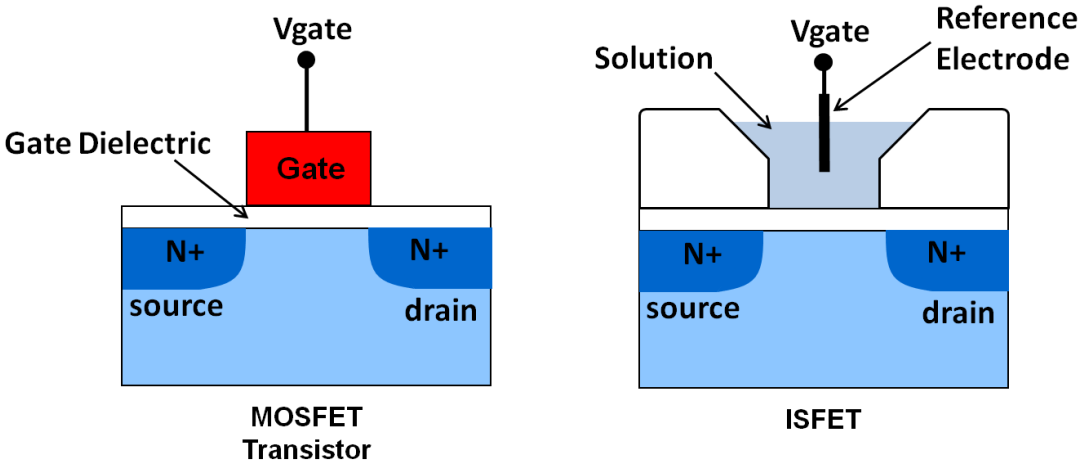

Figure 39. ISFET Biosensor compared to conventional MOSFET transistor.

The positively charged surface now attracts more electrons into the device conduction channel, increasing channel conductivity. The result is an increase in ISFET drain-to-source current as the pH concentration of the solution is decreased. Looking at the same effect in another way, the absorbed surface charge shifts the current-voltage (I-V) ISFET transistor characteristics as the pH concentration of the electrolyte in contact with the pH sensitive gate electrode is changed. Reported shifts are typically 50 to 60 mV for each unit of pH (Bergveld 2003a).

For biological or chemical sensing, a separate recognition material is added to the surface of the gate dielectric layer (Schoning and Poghossian 2002, Schöning and Poghossian 2006). A reaction at the gate electrode surface in proportion to the concentration of the substance being analyzed is used to change the pH concentration at

the sensor electrode surface. For example, the surface of the exposed gate dielectric layer could be coated with a highly selective enzyme, such as glucose oxidase (GOX), which is designed to detect the concentration of glucose in the solution. When the sensitized, enzyme-coated sensor electrode is now brought into contact with a glucose solution, an enzymatic reaction can take place, inducing a local reduction in the pH at the sensor electrode surface from the gluconic acid that is proportional to the glucose concentration.

$$Glucose \; + \; O_2 \; \xrightarrow{GOX} \; gluconic\ acid \; + \; H_2O_2 \qquad (22)$$

However, the gate electrodes for semiconductor devices are typically buried and electrically isolated underneath thick insulating dielectric layers. To function as a biosensor, the biologically (pH) sensitive layer needs to be brought to the surface of the semiconductor device structure where it can make direct contact with the electrolyte solution. Additionally, to maximize sensitivity by increasing the physical size of the sensor, the area of the biological or pH-sensitive layer may need to be quite large in proportion to the size of the biosensing ISFET transistor. This is the physical device width (W) and channel length (L) of the ISFET transistor. To address these issues, an extended gate biosensor (EGFET) is typically used. The EGFET is constructed of a large metal gate electrode with a pH sensitive layer brought up to the top surface of the sensor (Georgiou and Toumazou 2009) as illustrated in Figure 40. This top sensor electrode (the extended gate) is electrically connected to the gate terminal of the sub-surface conventional three terminal transistor, and the top surface of the pH-sensitized extended metal gate is now directly exposed to the electrolyte solution.

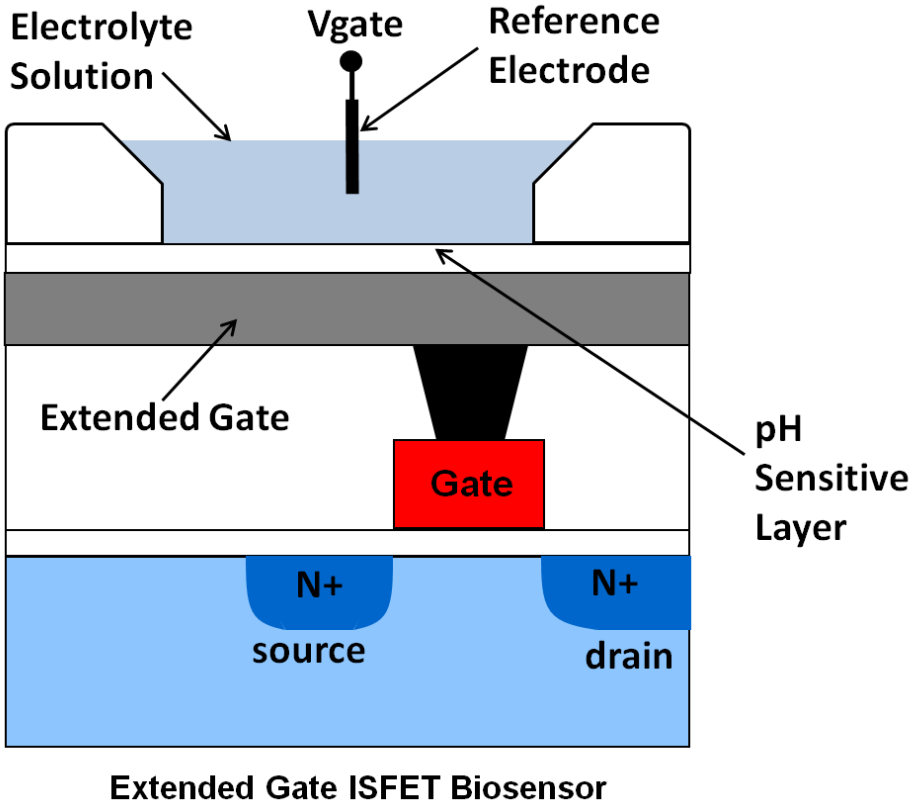

Figure 40. Extended gate ISFET simplified cross-section.

With this approach, the size of the extended-gate top electrode can be orders of magnitude larger than the ISFET transistor device's width and length. Again, absorbed charge, now on the surface of the extended gate electrode, shifts the transistor I-V characteristics, turning the EGFET into a biosensor.

At a fundamental level, the absorbed charge on the sensor electrode surface shifts the device threshold voltage (Vth), which is gate voltage required to turn on the ISFET. The effect of the threshold shift on the ISFET drive current (Ids) is modeled using the simplified relationship below (Wen-Yaw et al. 2008) for linear mode operation.

$$I_{ds} = \mu \frac{W}{L} Cox[(Vg - Vth^*)Vds - 0.5Vds^2] \quad (23)$$

$$where \quad Vth^* = Vth + \zeta \quad (24)$$

Again, μ is the mobility of electrons in the TFT device channel, W and L are the TFT device channel width and length, and Cox is the gate dielectric capacitance. Vg represents the external voltage applied to the gate of the external reference electrode. The new or shifted ISFET threshold voltage Vth* term in the equation equals the original MOSFET threshold voltage Vth plus an additional factor ζ to account for the potential shift induced by absorbed charge on the ISFET sensor electrode (Wen-Yaw et al. 2008). This simplified relationship for ISFET threshold voltage Vth* can then be expanded, as shown below, to include the new ISFET-related interface (surface) potential terms (Bergveld 2003a, Bergveld 2003b, Nguyen, Seol, and Lee 2011), in combination with the terms related to device material properties common to both ISFETs and conventional MOSFET or TFT semiconductor devices.

$$Vth^* = E_{ref} - \Psi + \chi^{sol} - \frac{\phi_{Si}}{q} - \frac{Q_{ox} + Q_{ss} + Q_B}{C_{ox}} + 2\phi \quad (25)$$

The (common) semiconductor device material properties are defined by the last three terms in the equation. ϕ_{Si} is the semiconductor work function, Cox is the gate dielectric capacitance, Q_{OX}, Q_{SS}, and Q_B represent the charges in the gate dielectric, the

surface and interface states, and the charge in the depletion region, respectively, and ϕ is the potential difference between the Fermi level of doped and intrinsic silicon. The ISFET-related device parameters are defined by the first three terms in the equation. E_{ref} is the reference electrode surface potential. X^{sol} is the surface dipole potential of the electrolyte solution, and Ψ is the surface potential of the ISFET sensor electrode, which is a function of the chemical reaction occurring on its surface. In practice, all of the terms in the equation are constant and independent of the solution pH, except for Ψ, which is a direct function of the electrolyte solution pH. Hence, only the Ψ term in the equation for ISFET threshold voltage Vth* changes as the solution pH changes.

$$\Delta\Psi = f(\Delta pH) \tag{26}$$

From site binding theory, which describes the charging of an insulator-electrolyte interface, the chemically active insulator (dielectric) surface of the ISFET sensor electrode contains hydroxyl (OH) groups which can accept or donate electrically active ions (typically H^+ ions) when in contact with an electrolytic solution (Schoning and Poghossian 2002). It is this chemical reaction at the ISFET sensor electrode surface that modulates the surface potential Ψ, and makes ISFETs sensitive to the pH of the solution. The H^+ ion protonation state of the ISFET sensor electrode surface can now be expressed as a direct function of the electrolyte solution pH, where the relationship of the surface potential Ψ to the solution pH is expressed using the following simple equation derived by Bergveld (Bergveld 2003a).

$$\Delta\Psi = -2.3\,\alpha\,\frac{kT}{q}\,\Delta pH_{solution} \tag{27}$$

$$\alpha = \frac{1}{\left(\frac{2.3kT}{q^2}\right)\left(\frac{C_S}{\beta_S}\right) + 1} \tag{28}$$

The ISFET sensitivity factor α varies between 0 and 1, and is a function of the ability of the ISFET sensor surface to deliver or take up H^+ ions (protons), with the maximum sensitivity at α = 1. Using a room temperature kT/q of approximately 26 millivolts, the maximum ISFET sensitivity is 59.2 mV/pH. This value is typically called the ideal Nernstian sensitivity. Not surprisingly, some ISFET electrode materials are more sensitive than others. Tantalum pentaoxide Ta_2O_5 is one of the better performing ISFET electrode materials, with a reported near ideal Nernstian sensitivity of 58 mV/pH over a wide pH range, while a conventional silicon dioxide SiO_2 dielectric layer has a sub-Nernstian sensitivity of only 30 mV/pH (Bergveld 2003b).

Large Area Active Matrix Array Biosensor Advantages

In practice, ISFETs biosensors can be configured as large parallel arrays of individually addressed extended-gate ISFETs and manufactured on silicon CMOS wafers (Meyburg et al. 2006). One illustrative example is the ION Torrent DNA sequencer, which uses a large, rectangular array of millions of individual extended-gate ISFET biosensors on a single CMOS integrated circuit for DNA sequencing. DNA recognition material is immobilized on the extended gate dielectric layer, and the functionalized DNA fragments cause a localized change in the pH at the extended-gate surface by emitting a burst of H+ ions upon bonding with the target nucleotides (dNTP) which are

flowing in solution over the entire surface of the ISFET sensor CMOS array (Merriman 2012).

While large-area ISFETs are desirable because of their large, sensitive capture area, combined with easier integration with area intensive chemical and biological recognition material, manufacturing large ISFETs using a CMOS wafer-fabrication process can become cost-prohibitive. This is primarily because the biological or chemical sensing array size for conventional ISFETs on silicon substrates is ultimately constrained by a photolithographic stepper field size to approximately 1 cm^2 for each CMOS die. Commercial high-volume TFT technology, used to manufacture large-area OLED and LCD displays, offers one lower cost alternative to produce large-area ISFET biosensors (Estrela et al. 2008, Pinto et al. 2012). This enables biosensing arrays orders of magnitude larger in size than conventional silicon-substrate ISFETs. In turn, a correspondingly larger number of unique biological or chemical recognition sites are now possible. Leveraging the massive scaling advantages of traditional LCD TFT display technology, which can now manufacture displays on gen2 sized rigid substrates that approach $10m^2$, offers the additional advantage of dramatically reducing the unfunctionalized sensor cost to pennies per cm^2 as described in chapter 1, which is expected to be key for low cost disposable biosensing applications.

Prototype Flexible ISFET Biosensor

In our new approach, the plastic-substrate TFT technology used to manufacture flexible displays (Figure 41) was applied to develop a new large-area and low-cost flexible ISFET biosensor. In construction, similar to the previously discussed flexible x-

ray detector development effort, the rigid and fragile glass or CMOS silicon substrates used to manufacture conventional ISFETs was replaced with a thin, durable, and flexible PEN plastic substrate. Integrated on the PEN plastic substrate are Indium Gallium Zinc Oxide (IGZO) metal oxide (MoX) TFTs combined with an indium-tin oxide (ITO) extended-gate, pH sensitive layer.

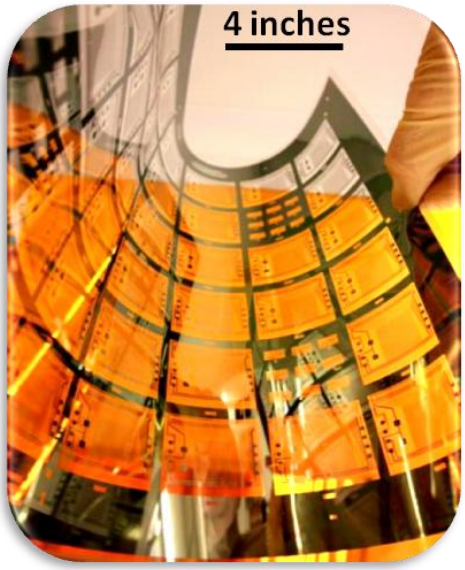

Figure 41. Flexible display on plastic.

Using this new configuration, the now-100% plastic ISFET biosensor is now shatterproof, as well as conformable and bendable. To help appreciate the 100% plastic form factor and the large sensor size now possible with this new approach, a photograph of a debonded 370 mm x 470 mm Gen2 flexible substrate is shown above. In the photograph, 20+ separate three inch diagonal flexible displays integrated on the same Gen2 370 mm x 470 mm substrate can be seen. Using the technical approach outlined in

this section, the same thin-film display technology used to make a Gen2-sized sheet of flexible displays can now be applied to make a comparable Gen2 sheet of flexible biosensors with only a few minor modifications to the upper thin-film process layers.

To evaluate the initial viability of the new concept, a prototype flexible, extended-gate pH biosensor was assembled using an IGZO TFT parametric test structure (Figure 42c) trimmed from a Gen2 plastic substrate, which was originally used for a large-area, flexible OLED display demonstration (O'Brien et al. 2013).

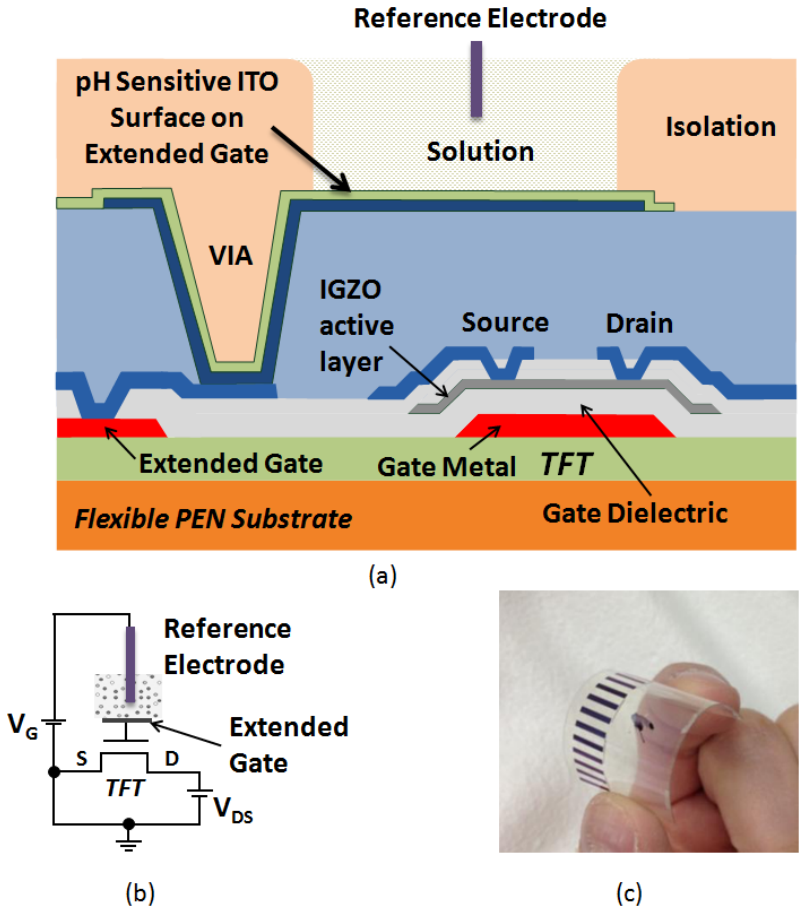

Figure 42. Prototype flexible ISFET biosensor. (a) Cross-section of flexible extended gate ISFET biosensor – Flex-BioFET- using a bottom-gate, inverted-staggered metal oxide IGZO TFT with an active channel passivation layer and ITO pH sensing layer. (b) Schematic of ISFET pH biosensor test circuit. (c) Optical photograph of Flex-BioFET test structure on PEN plastic substrate prior to assembly.

The intent was to use a typical TFT structure from a flexible display to prove that functional ISFETs biosensors can be manufactured using a standard flexible display process. As illustrated in Figure 42 and Figure 43, the 1-mm wide gate-bond pad (G) for the W/L = 9/9 µm IGZO TFT test structure is externally unconnected and functions as the extended-gate electrode for the new flexible ISFET. The top metal layer of ITO, used as the transparent top electrode in the flexible OLED display process, has been repurposed to function as the extended-gate pH-sensitive layer in the prototype flexible ISFET (Figure 42a) and is connected to the TFT gate electrode. While not typically used as the ISFET sensor layer, ITO has previously been shown to provide a Nernstian response for ISFETs on glass substrates between pH2 and pH12 (Yin et al. 2000, Chiang et al. 2009, Nguyen, Seol, and Lee 2011).

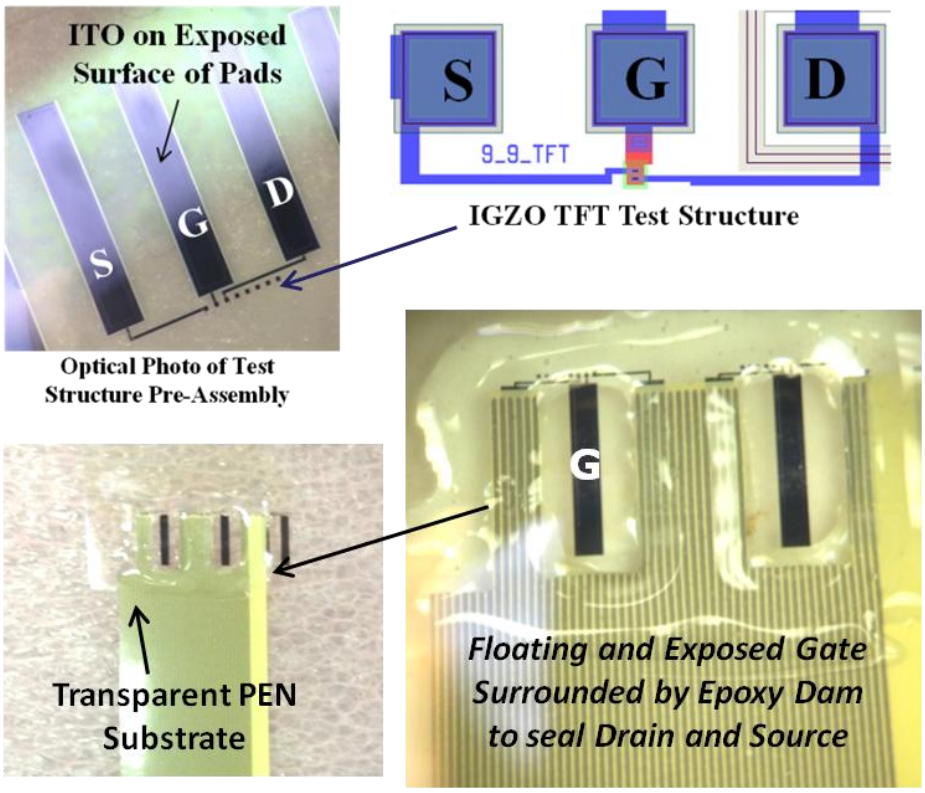

Figure 43. Prototype ISFET biosensor assembly

Using the existing ITO top metal layer as the pH sensor layer eliminates the need to make any changes to an existing active matrix display TFT display process sequence, and has the added advantage of demonstrating a pH-sensor layer common to most commercial OLED and LCD display processes. However, for pH sensing, a separate insulating well was added as a biosensing superstructure above the extended-gate electrode to hold or capture the electrolyte solution. To do this, an approximately 3 mm-long shallow well (dam) was formed over both the extended ITO gate using a thin layer of solvent-free epoxy to complete the biosensor superstructure (Figure 43). In production, the epoxy layer would likely be replaced with a (thick) thin-film layer, such as SU-8.

This epoxy well superstructure created an active ITO-gated pH sensor area of approximately 1 x 3 mm, and also provided electrical isolation between neighboring extended ITO gates in a simple linear sensing array structure. For testing, the flexible ISFETs were connected to a Keithley 4200 semiconductor parameter analyzer to measure the IGZO TFT I-V characteristics at room temperature in a dark enclosure. The prototype flexible ISFET gate electrode was then immersed in three different pH buffer concentrations by filling the epoxy well with the buffer solution from a micropipette, with a de-ionized water rinse between each pH change. Starting with pH4, a separate Ag/AgCl wire reference electrode was lowered into the solution well using a micro-manipulator probe head. The wire reference electrode was then connected to the Keithley 4200 to apply the gate bias (Vg) to the buffer solution and measure the flex ISFET drain to source current.

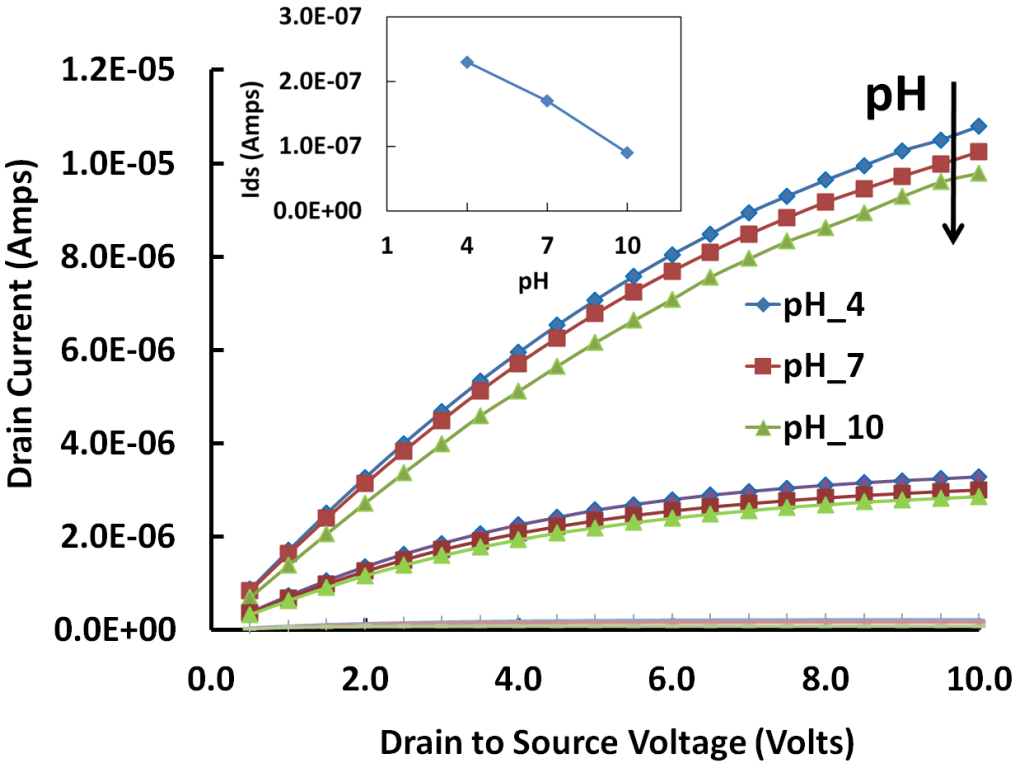

Figure 44. Flexible ISFET measured pH response.

At each of the three (pH4, pH7, and pH10) buffer concentrations, Ids-Vds sweeps were then performed with the reference electrode gate bias sequentially set to Vg = 5, 10, and 15 volts. As illustrated in the composite plot in Figure 44, a decrease in the prototype flexible ISFET drain current (IDS) was correctly observed as the pH concentration was increased, confirming decreasing H+ ion protonation of the ITO extended gate electrode surface as the pH concentration was increased.

A similar pH response of the ITO gated flexible biosensor was observed by also performing an Ids-Vg sweep at each of the three different pH buffer concentrations. As shown in Figure 45, the ISFET effective threshold voltage shifts positive as the solution pH is increased from pH4 to pH10. Again, as the pH buffer concentration is increased,

fewer positive H+ ions bond to the ITO sensor surface. This shifts the ISFET turn on voltage more positive.

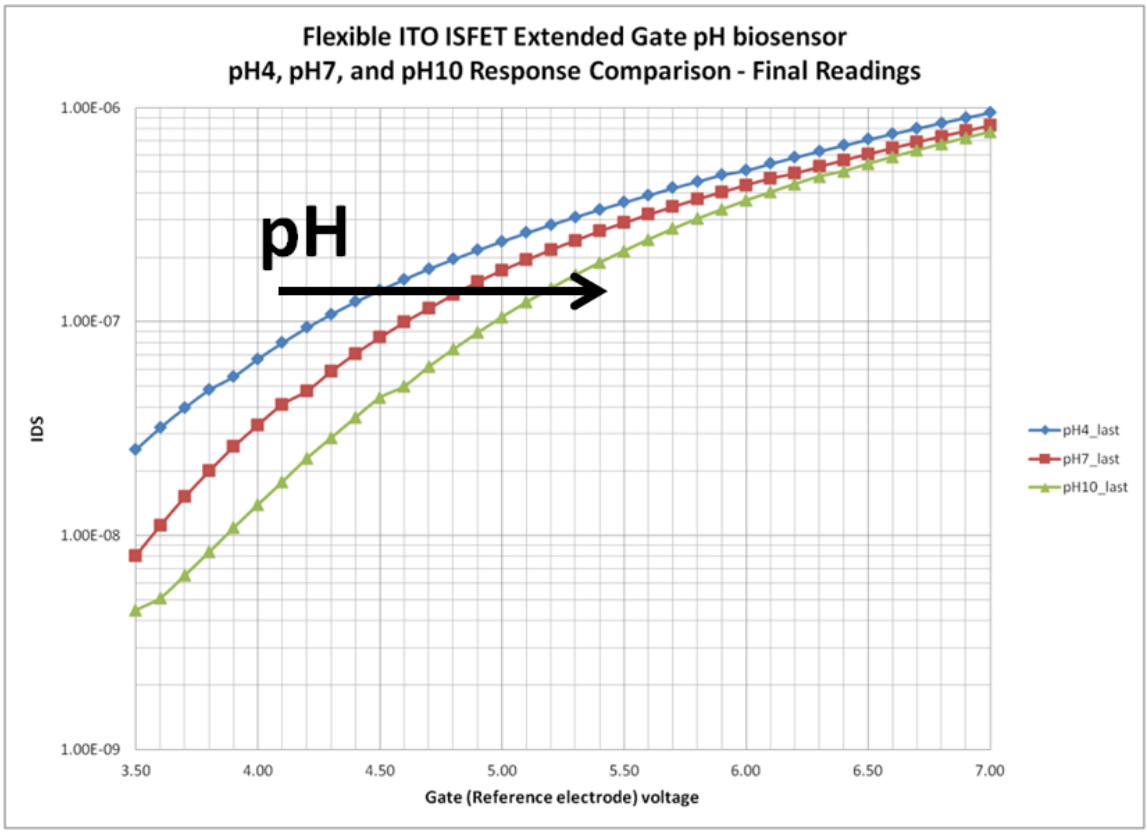

Figure 45. Flexible ISFET measured pH threshold voltage response.

Both of these measurements confirm that the prototype ITO-gated ISFET biosensor correctly senses the buffer solution pH and responds correctly to the pH concentration of the buffer solution. Hence, this early ISFET prototype demonstrated the initial viability of using an IGZO TFT integrated with an extended gate ITO sensor layer to produce flexible pH ISFET biosensors on PEN plastic substrates. However, given the

need to insert a separate Ag/AgCl wire reference electrode in the pH solution well, the complete ISFET biosensor assembly, including the reference electrode, is not flexible.

Flexible Biosensor with Integrated Reference Electrode

An improved now fully flexible ISFET assembly required the integration of a flexible reference electrode on the same PEN plastic substrate as the ISFET TFT and ITO extended gate sensor layer. To demonstrate this, a second flexible ISFET biosensor prototype was manufactured, but now with an integrated and flexible Ag/AgCl (silver/silver-chloride) reference electrode printed directly on the flexible PEN plastic substrate.

Referring to the figure below, a second IGZO TFT test structure was trimmed from an OLED flexible display substrate, identical to the TFT test structure used for the first prototype. To form the new integrated flexible Ag/AgCl reference electrode, a small dot of silver epoxy was first deposited adjacent to the solution well region on IGZO TFT test structure. A 30ga wire was then bonded to the dot and run to a separate printed circuit board (PCB) to form the external gate (Vg) connection for the reference electrode. In a production version, the separate external wire lead would be replaced by an integrated metal trace on the plastic PEN substrate. Next, a 700µm-wide flexible reference electrode was screen-printed on top of the TFT substrate in the space between the gate and drain bond pads using a flexible Ag/AgCl ink (Creative Materials 124-36), as shown in Figure 46. The flexible Ag/AgCl reference electrode was intentionally not printed directly onto the surface of ITO (metal) gate TAB pad of the TFT test structure to prevent the chlorine

in the Ag/AgCl ink from attacking the exposed ITO surface of the gate TAB pad and compromising the reference electrode connection.

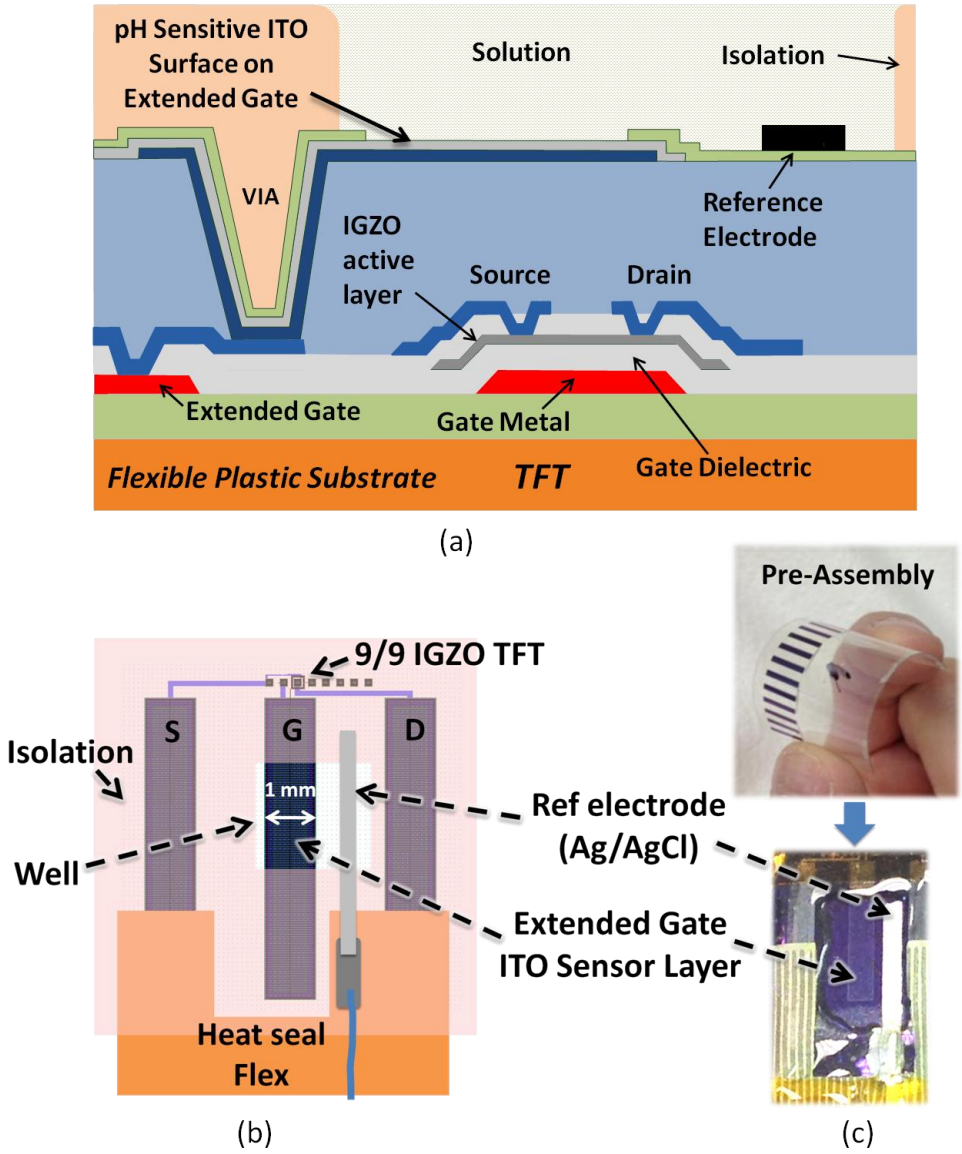

Figure 46. Flexible pH biosensor with integrated reference electrode (a) Cross-section of prototype flexible plastic ISFET pH biosensor, using a W/L = 9/9 µm bottom-gate IGZO n-channel TFT and a 1 x 3 mm extended gate ITO pH sensor layer. (b) Assembly drawing of the prototype flexible ISFET pH sensor with integrated Ag/AgCl reference electrode. (c) Optical photograph of the flexible ISFET prototype pre and post assembly.

Instead, the Ag/AgCl ink was printed on top of a separate silver epoxy dot, which was first patterned on the surface of the ITO gate pad prior to printing the Ag/AgCl ink. The chlorine in the Ag/AgCl will not attack or degrade the silver epoxy and silver. Again, an ~3 mm long shallow well for the pH solution was then formed over both the extended ITO gate and now the Ag/AgCl reference electrode using a thin layer of solvent-free epoxy. This created an active (ITO) pH-sensor area of approximately 1 x 3 mm as shown in Figure 46. Hence, in this new approach, the Ag/AgCl reference electrode and patterned epoxy well form the new ISFET biosensing superstructure added to the top of the baseline flexible display (TFT) process.

Experimental Results and Discussion

The drain, source, and reference-electrode (gate) leads for this newer and now fully integrated prototype flexible ISFET pH biosensor were then connected to a Keithley SourceMeter to measure the I-V device characteristics in collaboration with Sahil Shah. For this round of I-V ISFET measurements, the gate bias on the reference electrode was set to +10 volts and the drain-to-source bias to +5 volts to operate the TFT just below saturation, as well as insure that the TFT is turned on. The epoxy well was then filled with different pH buffer concentrations using the sequence of pH 4 → pH 7 → pH 10 → pH 7 → pH 4, with a sample interval of 400 seconds for each pH concentration. The epoxy well was again rinsed with de-ionized water between each pH change.

The ISFET drain current was then sampled from 0 to 10, 200 to 210, and 400 to 410 seconds in each interval, with an average of 10 data points per each 10-second interval. In typical operation, it is assumed that the ISFET will also be similarly briefly

sampled and then turned off to reduce dynamic power consumption. As illustrated in Figure 47, a decrease in the flexible ISFET drain current was again observed as the pH concentration increased from pH 4 to pH 10, confirming decreasing H+ ion protonation of the ITO extended-gate electrode surface as the pH concentration was increased.

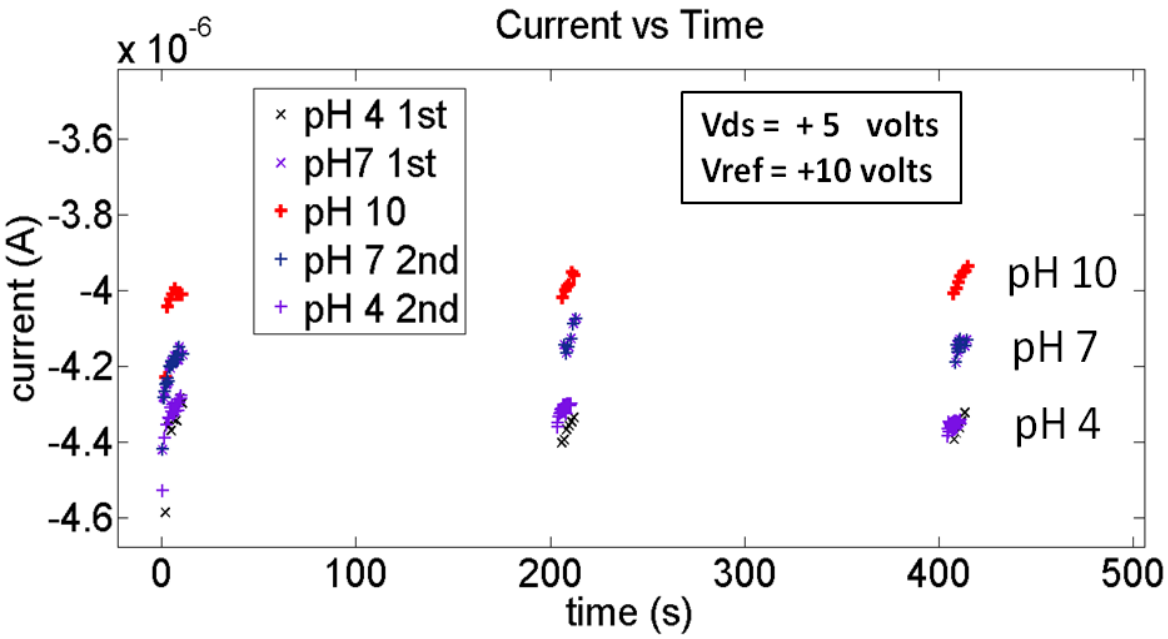

Figure 47. Flexible ISFET temporal response for pH sequence: pH 4 → pH 7 → pH 10 → pH 7 → pH 4, with the ISFET drain current sampled at 0 to 10 sec, 200 to 210 sec, and 400 to 410 sec in each interval

pH discrimination was also shown to improve at longer measurement intervals, with an observed average 4.7% difference in measured ISFET drain current between the three different pH buffer concentrations at 400 seconds. The most significant observed downward drift (drift) in ISFET drain current occurred during consecutive measurements in the initial 0 to 10 second sample period, which was initially attributed to hydration of the ITO pH sensor layer surface (Pinto et al. 2012, Jamasb, Collins, and Smith 1998).

As shown in the box plots in Figure 48, the pH response was also demonstrated to be repeatable over multiple pH cycles with the average ISFET drain current in the second pH4 cycle essentially identical to the initial measurement at 400 to 410 second measurement interval. However, we found that after continuous electrolyte immersion for several days, the chlorine from the printed Ag/AgCl reference electrode began to etch the ITO sensor layer on the extended gate electrode. Switching to gold for the reference electrode was observed to eliminate this issue.

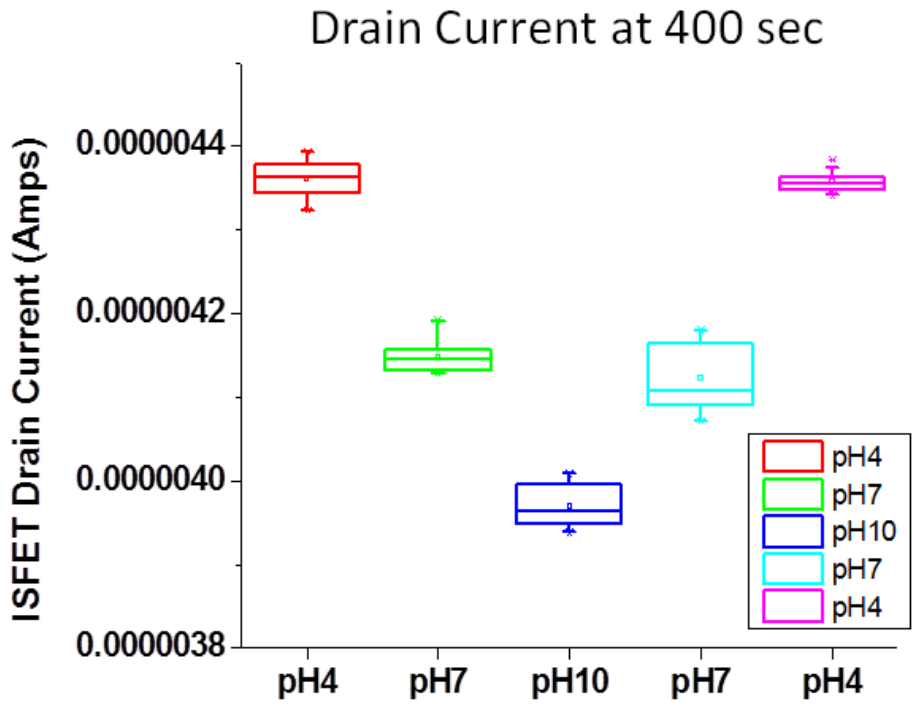

Figure 48. Box plots of ISFET drain currents measured at 400 to 410 seconds for each pH interval. ISFET drain current correctly decreases as pH increases and pH response is repeatable over multiple cycles.

As illustrated in Figure 49, the new integrated flexible gold reference electrode was formed using a gold-plated printed circuit board (PCB) trace trimmed from a

separate flexible substrate. These new flexible ISFETs were designed with an extended gate sensor area of 1 x 1 mm, which was electrically connected to the gate electrode of a W/L = 200/9 µm IGZO metal oxide TFT. This provides an extended gate sensor surface that is ~550X larger than the area of the TFT gate electrode.

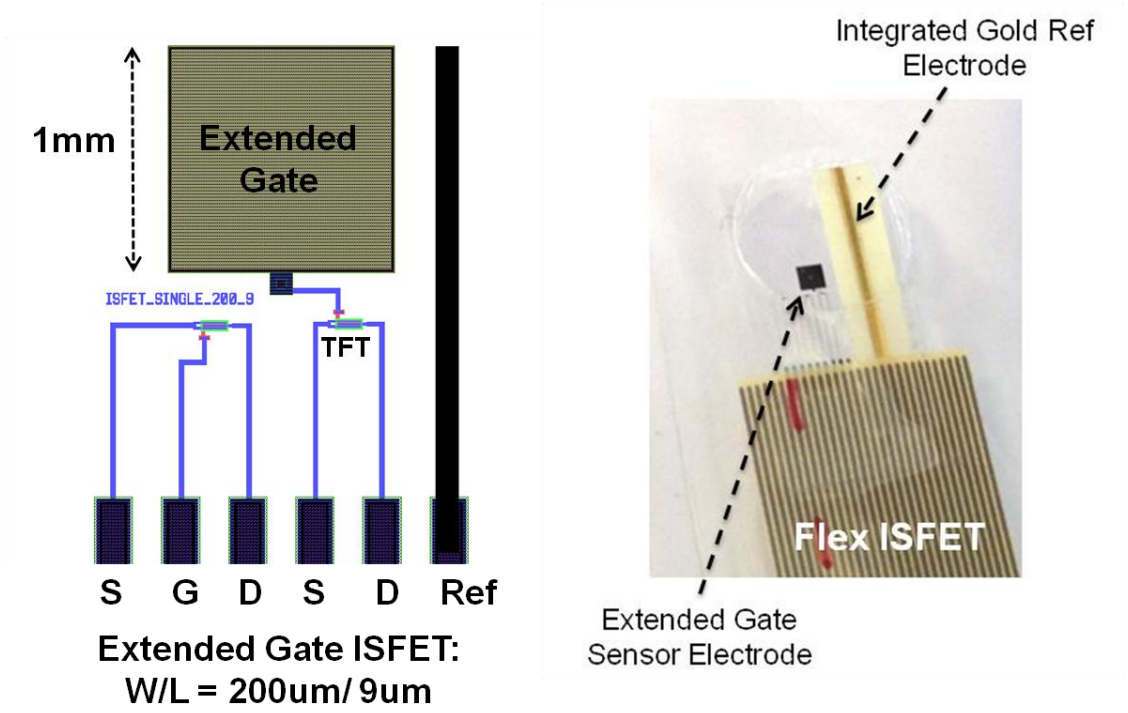

Figure 49. Flexible pH biosensor with integrated gold reference electrode.

To assemble, the trimmed gold trace was positioned immediately adjacent to the 1 x 1 mm extended gate. To make the external electrical connections, heat-seal flex was then bonded to the drain and source bond pads on the TFT test structure, along with the gold reference electrode, followed by bonding to a small separate breakout PCB. GBC heat seal thermal lamination film was then applied to provide both electrical isolation and environmental encapsulation for the flexible ISFET test structures, instead of the printed solvent-free epoxy. To encapsulate (laminate), a small hole that exposed both a portion of

the gold reference electrode and the entire 1 mm^2 ITO sensor electrode was punched in the top sheet of the GBC thermal lamination film, and the bottom sheet of the GBC lamination film was positioned under the ISFET test structure. A thin temporary sheet of Teflon was then placed over the top of the assembly to protect the sensor electrode and the entire flexible assembly was run through 110°C rollers to activate the adhesive and seal the assembly.

Functionality of the new gold reference electrode was initially evaluated at wafer level using an unassembled ISFET test structure with the trimmed gold trace taped down adjacent to the ISFET extended gate sensor pad. The ISFET electrodes were connected to a Keithley 4200 Semiconductor Parameter Analyzer and a series of ISFET drain current (Ids) vs. gate electrode voltage (Vgate) plots were generated (Figure 50). The first plot is with an external (separate) gold-plated electrode (needle) making direct contact with the extended gate electrode pad. The separate gold electrode was then raised and a (green) drop of pH 7 buffer solution was placed on top of the ISFET 1mm^2 extended gate electrode sensor pad. The tip of the separate gold electrode was then lowered into the drop of pH 7 buffer solution, without touching the sensor electrode surface, as shown in the Figure 50 photograph. In this experimental configuration, the gold needle now functions as a conventional ISFET reference electrode. A second -10 volt to +10 volt Ids vs. Vgate plot was captured and overlaid on the previous plot.

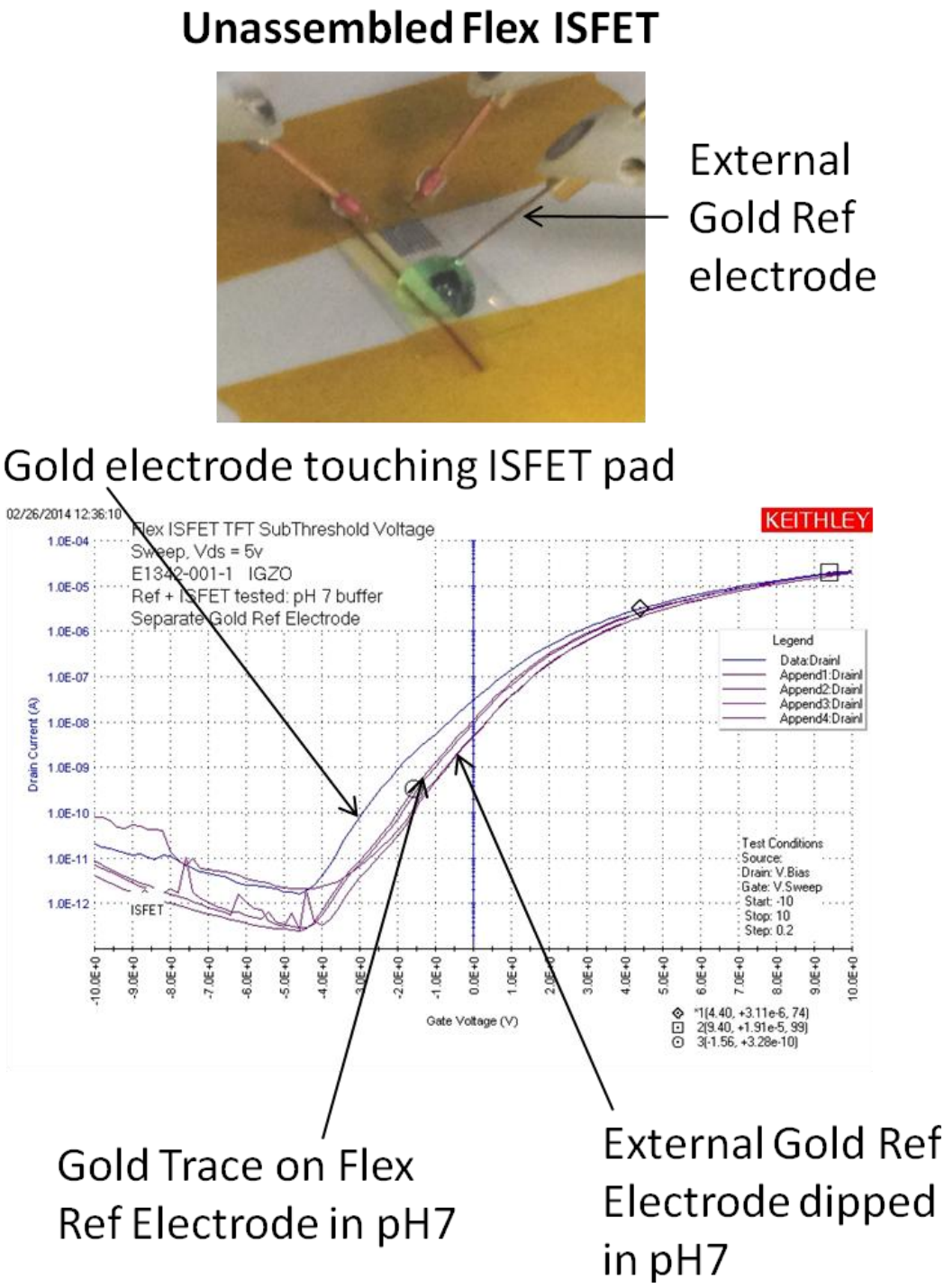

Figure 50. pH test results for unassembled ISFET test results at wafer level with trimmed gold trace (on flex) taped down next to ISFET extended gate sensor pad.

As shown, an approximately 1 volt positive shift in the TFT threshold voltage was observed using the separate gold needle as an ISFET reference electrode. The external gold needle electrode was then removed from the pH 7 buffer solution and a third Ids vs. Vgate plot was captured with the Keithley 4200 gate terminal now connected to the trimmed gold trace, which was also covered by the same drop of pH 7 buffer solution. As shown in the same figure, similar Ids vs. Vgate results were observed using all three experimental techniques, indicating that the new flexible gold ISFET reference electrode is functioning correctly and the ISFET is sensing pH.

Limitations of Existing Flex ISFET Technology

While all of the reported experimental results demonstrated the correct response of the drain current to solution pH, the results also showed that the existing flex ISFET configuration is currently unable to detect small differences or variations in solution pH. As illustrated in Figure 51, a wide spread in measured flex ISFET drain currents was observed at each of the three different pH buffer solution concentrations when plotting all of the captured ISFET drain current data from Figure 47 as function of solution pH. This limitation is further illustrated in Figure 51, where the ISFET drain current for a pH 8 or even a pH 9 buffer solution could easily fall within range of measured drain currents for pH 7. This indicates that the current ITO-gated flex ISFET configuration is currently unable to tell the difference between a pH 7 and a pH 8 buffer solution. To help understand this sensitivity issue, the pH response was more closely evaluated as a function of time.

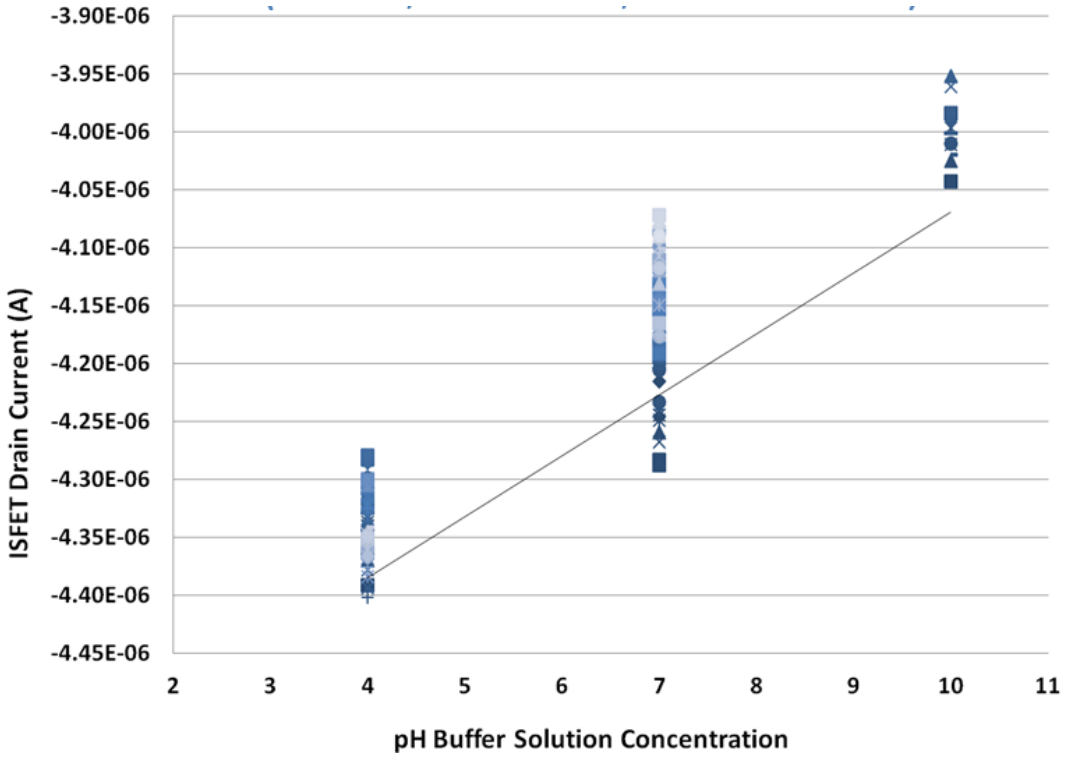

Figure 51. Flexible ISFET temporal response dataset for pH sequence: pH 4 → pH 7 → pH 10 → pH 7 → pH 4. All ISFET drain current measured at pH4, pH7, and pH10, from 0 to 10s, 200 to 210s, and 400 to 410s. Wide spread in ISFET drain currents observed at each of the different pH buffer solution concentrations.

As illustrated in Figure 52, the ISFET drain current appears to be dropping as a function of how long the ITO-gated ISFET sensor surface is exposed to (immersed in) the pH buffer solution. The observed temporal drift in the ISFET drain current over time also appears more pronounced when the ISFET gate and drain are biased, as shown in the zoomed in portion of the pH response plot for the 400 to 410 second measurement window, at Vg = 10 volts, and Vds = 5 volts (bottom plot in Figure 52). However, drift as a function of time is a well known issue with conventional ISFETs. As reported by Jamasb, ISFET threshold voltage tends to drift slowly positive over time. The result is

lower ISFET drain current as a function of time, (Jamasb, Collins, and Smith 1998) identical to what we observed.

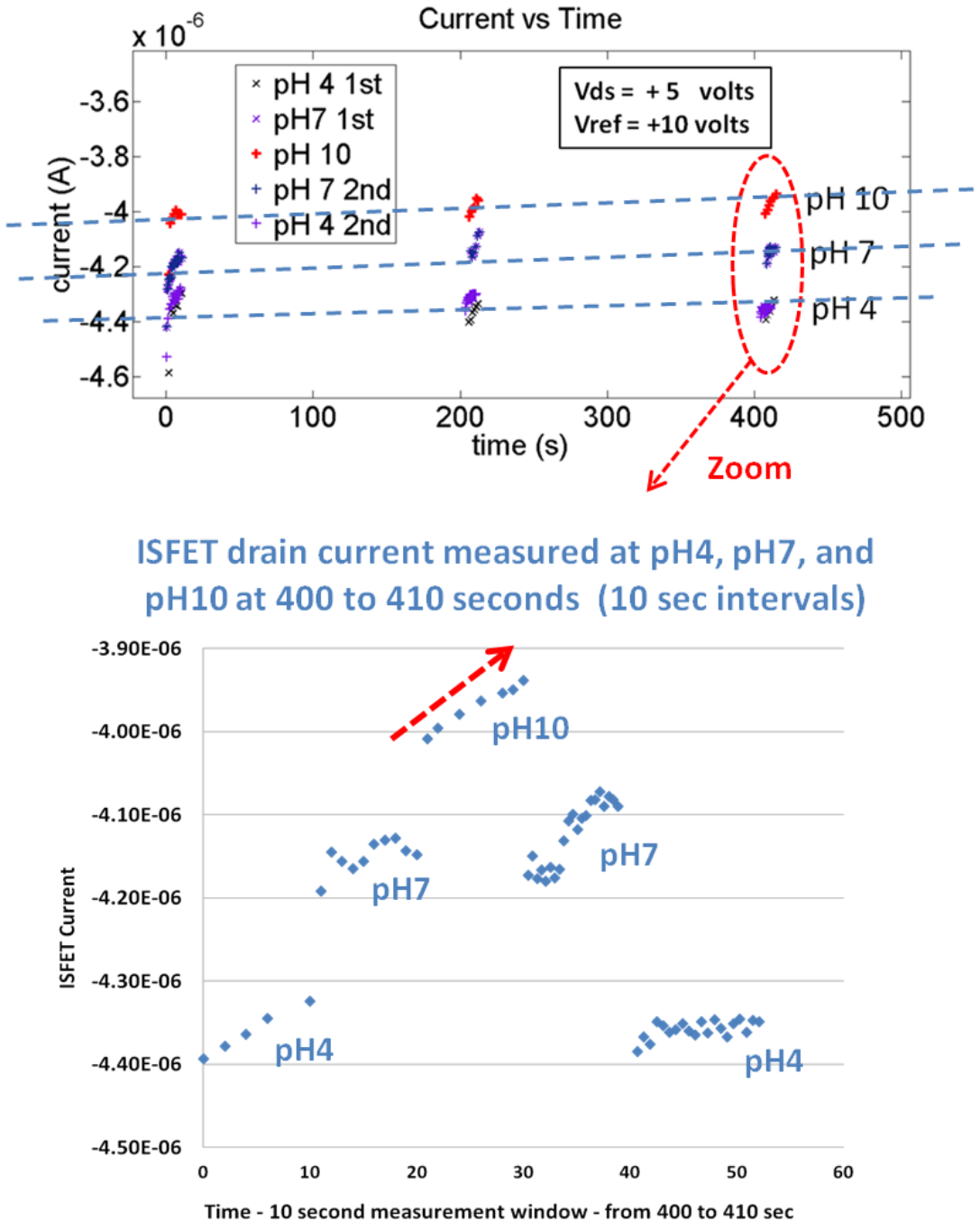

Figure 52. Effect of time in pH buffer solution on Flex ISFET pH Response.

As discussed in chapter 1, the maximum processing temperature for PEN plastic substrates is limited to approximately 200°C (Wong and Salleo 2009). This lower-temperature processing has previously been shown to aggravate or worsen TFT device stability when a sustained DC bias is applied to the TFT gate electrode (Allee et al. 2008). However, as illustrated in Figure 53, the application of a sustained DC bias on the TFT gate electrode was shown to shift the IGZO TFT threshold voltage negative as opposed to the positive threshold shift observed on the IGZO TFTs used on flex ISFETs.

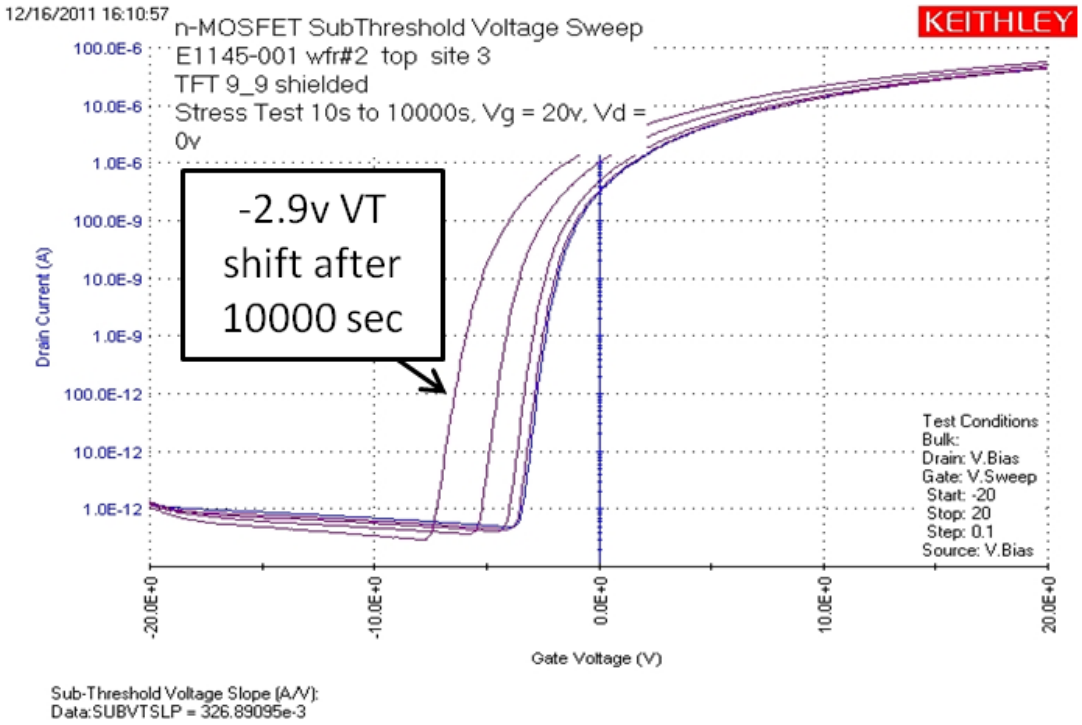

Figure 53. IGZO TFT positive gate DC bias stress stability data. Stress Conditions: Vgs = +20v, Vds = 0v; data taken at 0 sec, 10 sec, 100 sec, 1000, and 10000 sec's

This implies that another mechanism is responsible for the observed positive threshold shift of the ISFET IGZO TFTs. Literature reports that a temporal positive

ISFET threshold voltage drift is can be caused by a change in the chemical composition of the ISFET sensor surface over time, where some sensor electrode materials are known to be more prone to chemical modification than others. In one example, Ta_2O_5 and Al_2O_3 sensor electrodes are reported to be more robust than SiO_2 electrode (Jamasb, Collins, and Smith 1998). Hence, one explanation for our observed drift is that the chemical composition of the ITO sensor electrode is changing as both a function of time as well as voltage bias, when the ITO-gated ISFET sensor electrode is immersed in an electrolyte solution.

The observed temporal threshold voltage drift also appears to influence the Nernstian mV/pH response of the ITO gated flex ISFET. From Bergveld (Bergveld 2003b), a relatively consistent value for the Nernstian response was expected, with a magnitude less than the 59mV/pH ideal response. Instead, an indeterminate Nernstian response was observed, with the calculated response shown to be affected by the length of time the ITO sensor electrode was immersed in the pH buffer solution. As described earlier, the Nernstian response in mV/pH directly corresponds to the change in the ISFET threshold voltage ΔVth* as a function of the change in solution pH (ΔpH).

$$Nerstian \quad {}^{mV}/_{pH} \quad = \quad {}^{\Delta\Psi}/_{\Delta pH} \; = \quad {}^{\Delta Vth^*}/_{\Delta pH} \tag{29}$$

The relationship for the ISFET threshold voltage Vth*, as a function of the experimentally measured Ids, is expressed by rearranging the ISFET equation for drain current (Ids) and solving for Vth*.

$$I_{ds} = \mu \frac{W}{L} Cox[(Vg - Vth^*)Vds - 0.5Vds^2] \quad (30)$$

$$Vth^* = V_g - \left[\frac{\left(\frac{Ids}{K} - \frac{Vds^2}{2}\right)}{Vds}\right] \quad (31)$$

$$where \qquad K = \mu \, {}^{W}/_{L} \, Cox \quad (32)$$

Using this equation, experimentally derived ISFET threshold voltages Vth* using the measured ISFET drive current (Ids) after 10 seconds of immersion, and then after 410 seconds for each of the different solution pH's are shown in Figure 54. The value for K was calculated using the physical parameters for the W = 9 μm/L = 9 μm IGZO TFT, where μ = 13.1 cm^2/V-sec and Cox = 0.00015 F/m^2. The drain bias (Vds) is 5 volts and the gate bias (Vg) is 10 volts. The delta threshold voltage (ΔVth*) is the difference in calculated ISFET threshold voltages Vth* for neighboring solution pH's. The Nernstian response in mV/pH is then calculated by dividing the calculated ΔVth* (in millivolts) by the difference in solution pH, which is three (pH4 → pH 7 → pH10). The calculated Nernstian responses mV/pH were then averaged for each of the different solution pH's, using the last two ISFET drain currents captured at the end of the 0 to 10 second and 400 to 410 second measurement period.

As illustrated in Figure 54, a 47 mV/pH sub-Nernstian response was observed after 10 seconds of exposure to the pH buffer solutions, comparable to what ISFET theory might predict (Bergveld 2003b). However, after 410 seconds of exposure, a 67 mV/pH super-Nernstian average response was observed using the same analysis.

	pH4	pH7	pH10	pH7	pH4	Nerstian	mV/pH
calc Vth*	3.139	3.252	3.418	3.276	3.138		
delta Vt (mV)	113.26	113.26	166.08	142.45	138.02	average:	
mV/pH		37.75	55.36	47.48	46.01	46.7	
calc Vth*	3.124	3.241	3.418	3.272	3.144		
delta Vt (mV)	117.10	117.10	177.19	145.77	128.47	average:	
mV/pH		39.03	59.06	48.59	42.82	47.4	
						after 10 seconds	
					avg	47.0	mV/pH
calc Vth*	3.078	3.278	3.480	3.346	3.068		
delta Vt (mV)	200.65	200.65	201.96	134.55	277.40	average:	
mV/pH		66.88	67.32	44.85	92.47	67.9	
calc Vth*	3.099	3.294	3.492	3.337	3.081		
delta Vt (mV)	195.15	195.15	197.25	154.44	256.19	average:	
mV/pH		65.05	65.75	51.48	85.40	66.9	
						after 410 seconds	
					avg	67.4	mV/pH

Figure 54. Experimentally derived ITO-gated Flex ISFET Nernstian mV/pH responses after 10 seconds and 410 seconds of immersion in pH buffer solution

Unfortunately, the observed super-Nernstian response at longer ITO electrode immersions can't be explained using conventional ISFET theory (Bergveld 2003b), which sets an upper limit of 59.2 mV/pH for the ideal Nernstian response. It appears that temporal drift in ISFET drain current, which is more pronounced when the ITO electrode is immersed for longer time intervals both affects and compromises the ISFET Nernstian response.

Multi-Analyte Biosensing Active-Matrix Arrays

Looking ahead, a production flexible ISFET biosensor could be configured as a large, parallel, active-matrix TFT array with individually addressed ISFET biosensors integrated on the same flexible plastic substrate (Migliorato et al. 2008, Nakazato 2009). Large parallel ISFET biosensor arrays offer increased sensitivity by increasing the total sensor surface area and reduce the capacitive loading on each ISFET TFT, which also increases sensitivity by using a large number of separate, smaller extended-gate sensor pads.

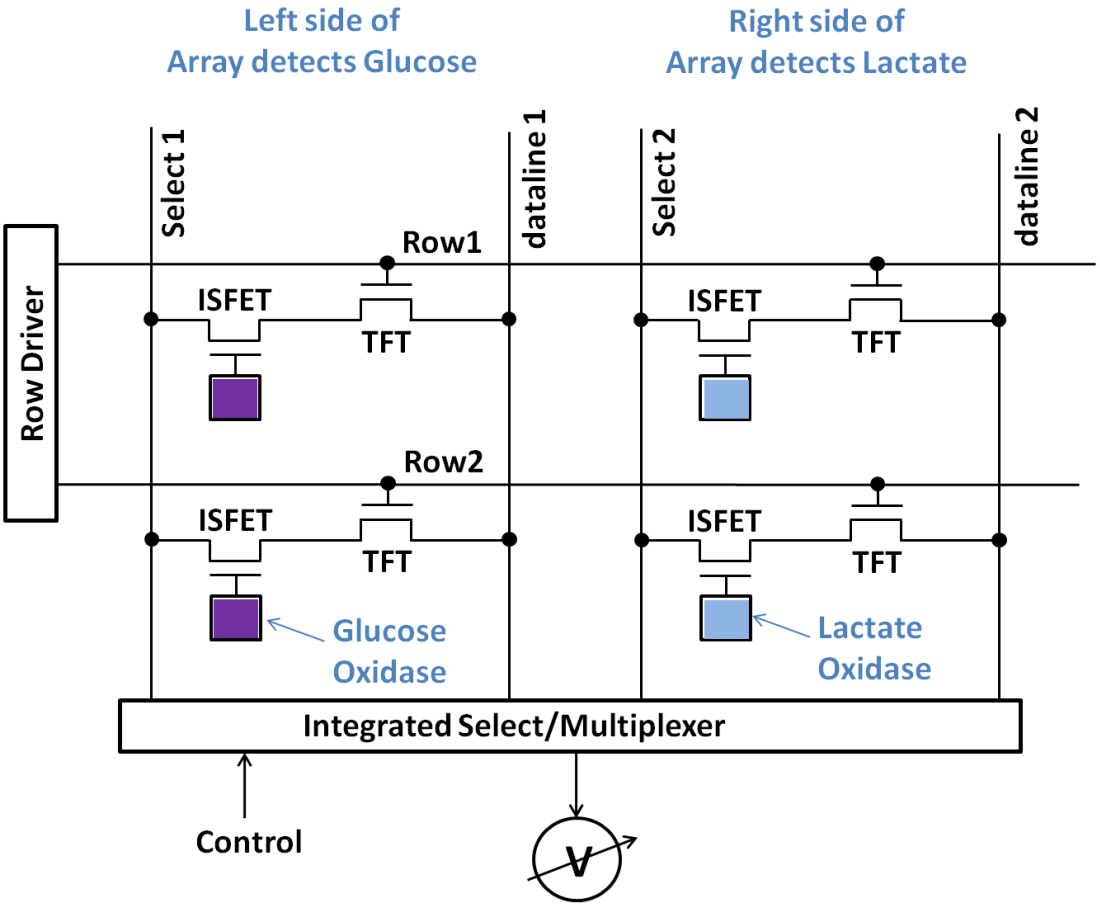

Figure 55. Multi-analyte flexible ISFET biosensor.

Each of the smaller ISFET sensor pads is then connected to its own TFT, as opposed to just one extremely large extended gate pad (sensor) connected to a single transistor. Large, parallel ISFET arrays also allow the extended gate sensor pads in the same active matrix array to be functionalized with different bio-recognition materials. For example, the extended gate-sensor pads for the flexible TFT ISFETs on the entire left side of an active-matrix array could be functionalized with glucose oxidase, while the ISFETs on the entire right side could be separately functionalized with lactate oxidase.

This conceptual dual-mode configuration would then provide the ability to simultaneously monitor both glucose and lactate levels, as illustrated below in a simplified 2 x 2 TFT active matrix array (Figure 55). In practice, the active-matrix-array size would be much larger, with an estimated several hundred rows and columns (or more). Note that the (flexible) reference electrode and its connection are not shown in the simplified schematic.

In operation, to select and read out an individual two transistor 2T biosensing ISFET cell, a single row line is turned on by applying a high positive-voltage pulse in combination with applying voltage to one of the vertical select (column) lines. Asserting the row lines turns on the 3-terminal TFT access transistor and the voltage on the column (select) line biases the drain of the ISFET biosensor. Now, through the dataline port, the I-V characteristics of each selected 2-terminal flex TFT biosensor (e.g., an EGFET) can be measured externally. An external control signal connected to a column parallel multiplexer (MUX) then sequentially steps though the select lines (Select1 and Select2 in the figure) to readout each ISFET in the active row. After reading out, the row is turned

off, the next row is then turned on, and the sequential ISFET readout operation is repeated. This row-by-row sequence is repeated until the entire ISFET TFT array is read out. External signal processing is then applied to each of the ISFET I-V readouts to determine the detected glucose and lactate concentrations.

One potential conceptual application for this type of glucose and/or lactate biosensing is a disposable transdermal smart bandage or skin patch to monitor human physiological conditions. For example, a flexible biosensor patch could be applied directly to the skin surface on the lower extremities of diabetic patients to detect the formation of pressure ulcers, or to monitor for infection in existing ulcers. Knight et al. reported that the lactate concentration in human sweat can change in response to the breakdown of soft tissue during the formation of pressure sores, common to diabetic patients (Knight et al. 2001). Derbyshire et al. later described a biosensor that could be applied to the skin surface to monitor lactate levels in human sweat as a indicator for pressure ulcers forming in at-risk diabetic patients (Derbyshire 2013). The thin and conformal form factor of the flexible ISFET TFT biosensor described in this chapter seems like an excellent fit for this type of skin-mounted disposable smart patch or bandage.

In an alternative—albeit speculative—application, the operation and configuration of a large active matrix array of ISFETs on a flex plastic substrate is quite similar to the Ion Torrent CMOS DNA sequencer (Merriman 2012, Rothberg et al. 2011) described earlier in this chapter, as well as other similar ISFET devices for DNA analysis (Gonçalves et al. 2008, Toumazou et al. 2013, Lee, Kim, and Kim 2009). However, the silicon CMOS ISFET sensor surface area of the Ion Torrent DNA sequencer is at least

10X to 100X smaller than what should be possible using a similarly configured flexible TFT-based ISFET biosensor. While still unproven, a much larger TFT-based ISFET biosensor may offer higher sensitivity than conventional CMOS-based ISFET biosensors.

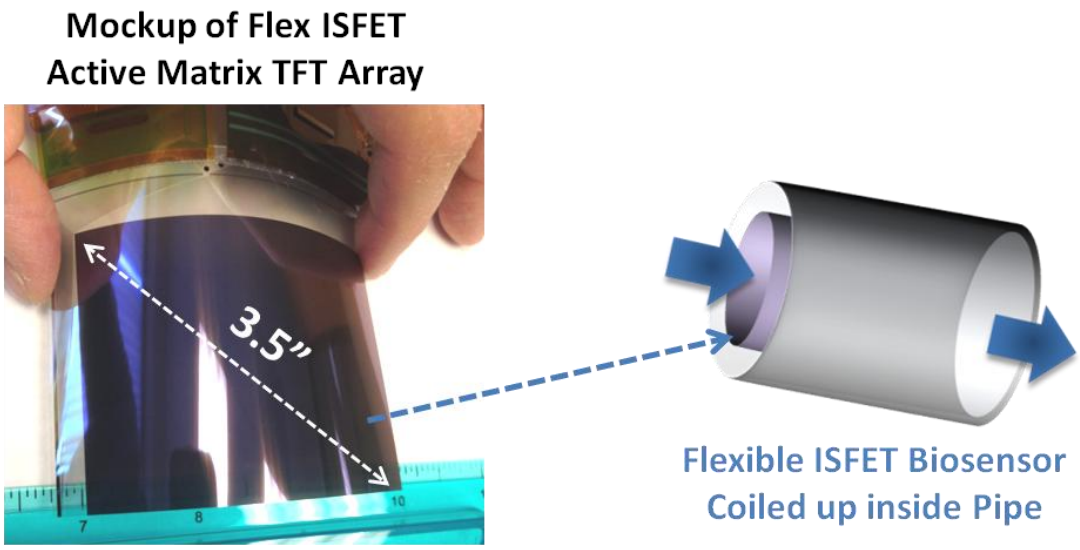

Figure 56. Flexible ISFET biosensor coiled up inside a pipe.

New form factors are also envisioned by adding flexibility to ISFET biosensors. For example, the same flexible ISFET could also be coiled or rolled up to line the inside of a pipe to significantly increase the active sensor area. In a DNA sequencing application, the nucleotides would then be pumped through the ISFET-lined pipe as one approach to take advantage of the now much larger sensor area offered by using TFT technology to manufacture ISFET biosensors.

Summary

The results from the initial flexible ISFET biosensor prototype, and especially from the second flexible ISFET prototype with the integrated Ag/AgCl reference

electrode, demonstrate that flexible display technology can be readily personalized to manufacture 100% plastic ISFET pH biosensors. The described new technique applies commercial flat panel display technology to make very large area active matrix TFT sensor arrays, which are more than 10X less expensive to manufacture than comparable CMOS-based ISFETs and provide a sensing area that is orders of magnitude larger than CMOS-based ISFETs. These new larger TFT display technology-based ISFETs also allow for much easier integration with area intensive chemical and biological recognition material as well as allow for a larger number of unique recognition sites to be incorporated on the individual ISFET sensor arrays for low cost multiple disease and pathogen detection. These new, flexible ISFETs are expected to be useful in biosensing applications in which low cost, disposability, shatter resistance, and/or a large biosensing array area is valued. Envisioned flexible biosensor applications include disposable smart bandages to monitor human physiological conditions, multi-analyte water quality monitors coiled inside piping, and food safety biosensors, as well as implantable biomedical diagnostic sensors. However, while the discussed ITO-gated flex ISFET, correctly senses solution pH, the current configuration is unable to detect small pH changes. Temporal threshold voltage drift also appears to influence Nernstian mV/pH response, which becomes issue during extended duration immersion in electrolytic solutions.

CHAPTER 6

FLEXIBLE BIOPHOTONICS

The knowledge to reconnect a brain does not exist yet in the galaxy

Mr. Spock, *Star Trek*

This chapter presents a new biophotonic application for large-area, high-resolution, flexible OLED display technology currently used to manufacture color flexible displays on plastic substrates. The new concept uses a fully addressable, high-resolution flexible OLED active matrix array to selectively stimulate and/or silence small groups of neurons on the cortical surface or within the deep brain. Fundamentally, the new approach involves mating a conformal high-resolution flexible OLED display with the cortical surface of the brain or, alternatively, injecting a narrow sliver of an ultra-thin flexible OLED display deep into the brain. Again, similar to the previous chapters, this new flex biomedical application required minor modifications to the existing flexible display superstructure, as well as changes to the design of the active matrix array.

Background

Optogenetics is a new biophotonic technology in which light stimulation is used to control the excitation, inhibition, or signaling pathways of optically excitable cells in genetically modified neural tissue. Recent research has identified Optogenetics as a powerful new tool to diagnose and treat, as well as understand (Deisseroth January 2011), numerous neurological/psychiatric diseases and disorders, such as epilepsy, stroke, seizures, paralysis (Platoni 2010), depression (Foutz, Arlow, and McIntyre 2012),

schizophrenia, and Parkinson's disease (17 December 2010, Deisseroth 2010). Using a viral vector, neurons are genetically modified to express light-gated ion channels in the cellular membrane which are sensitive to incident light. Cells expressing Channelrhodopsin-2 (ChR2) are activated or excited by blue light, while yellow light directed on cells that express Halorhodospin are quieted or silenced (Zhang et al. 2007, Han and Boyden 2007).

A common approach, familiar from striking photographs in major publications (Schoonover and Rabinowitz 2011), involves inserting the exposed tip of a fiber-optic cable into the brain tissue of an animal model—typically a rat or mouse (Wang et al. 2012). An external light source—a laser or LED—is then mechanically coupled to the end of the fiber-optic cable, and the neural tissue surrounding and underneath the exposed tip at the other end of the fiber optic cable, is illuminated. However, penetrating fiber optic–based neural stimulation methods still require a permanent opening in the cranium, which poses serious infection risk to the animal model undergoing the procedure. The single cylindrical fiber light source from the exposed tip also projects nonspecific omnidirectional illumination over a large volume of neural tissue, limiting the ability of fiber optic–based methods to target localized neural regions.

Newer approaches replace the fiber-optic probe with a small array of discrete LEDs bonded to the surface of a thin, flexible, biocompatible substrate (Kim et al. 2010, Kim et al. 2013). With an integrated miniature electrical power source mounted inside the skull and using wireless inductive power transfer, this approach is designed to eliminate the need for a permanent opening in the cranium by using an array of discrete LEDs placed in direct contact with the cortical surface or within the deep brain using a

penetrating probe. However, one key limitation with existing discrete LED arrays is the requirement to turn on either the entire emissive array or activate major sections of the emissive LED array. This inability to turn on small individual (single) pixels prevents optogenetics researchers from optically exciting and/or silencing localized regions of neural tissue, as well as increasing the electrical power consumption of the implanted device.

To address these limitations, a new Optogenetics on flex concept was developed in collaboration with Dr. Jennifer Blain Christen. Instead of a discrete component LED array, the new flex electronics concept illustrated in Figure 57 involves mating a high-resolution flexible OLED display to the cortical surface to optically excite neural tissue. This new approach for Optogenetics leverages low-cost, large-area, flexible, color OLED display technology (O'Brien et al. 2013) to extend earlier LED-based technology (Kim et al. 2010, Kim et al. 2013) to now provide a fully addressable high-resolution emissive electro-optical array.

As illustrated below, the conceptual flexible OLED optogenetics device is designed as a chronic *in vivo* implant. To place the device, a craniotomy is performed on the animal model and the entire flexible display substrate is pressed up against the cortical surface. The bone is then replaced to seal the skull. Electrical power for the implant would be provided using wireless inductive power transfer, similar to a cochlear implant. In the envisioned operation, selected individual OLED pixels in the flexible display would be turned on (addressed) to target and selectively illuminate specific localized regions, as opposed to turning on the entire display as required in today's more conventional LED-based approaches (Kim et al. 2013, Kim et al. 2010).

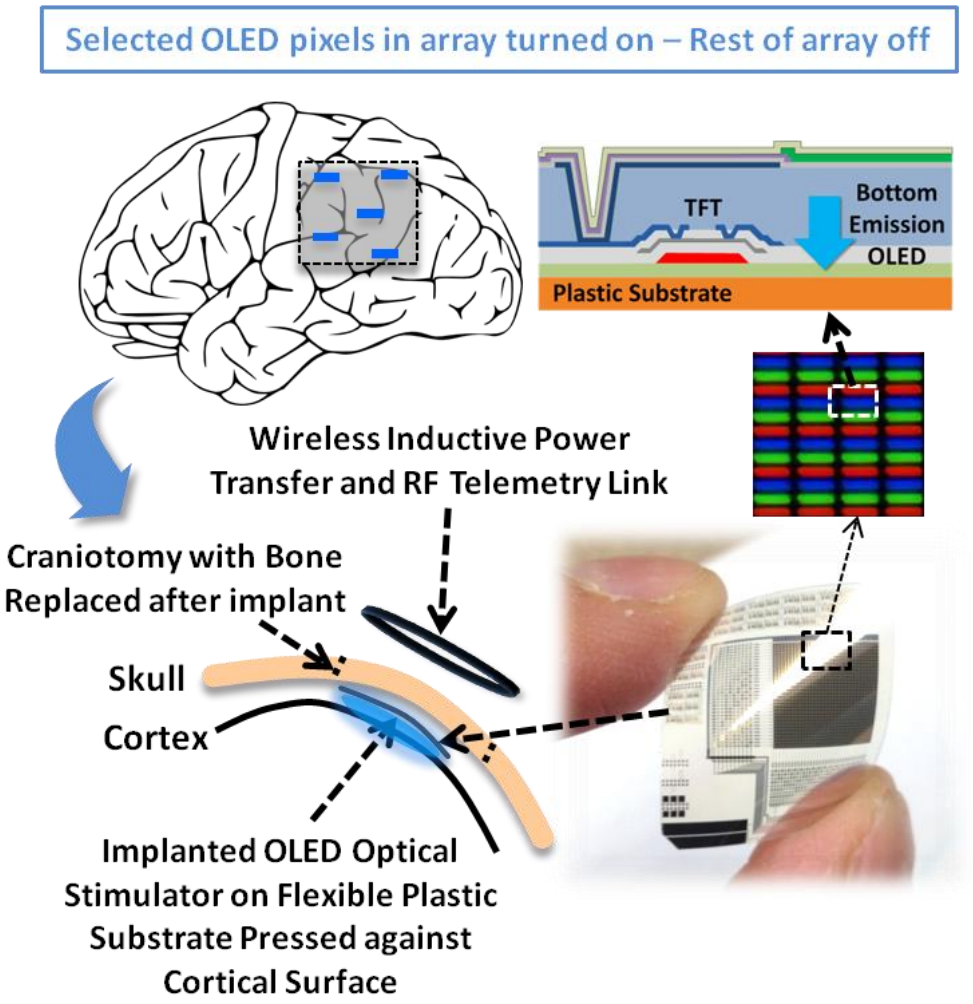

Figure 57. Concept for chronic low power flexible color OLED display on a transparent plastic substrate to selectively optically stimulate and/or silence isolated groups of neurons.

Applying Flat Panel Flexible Display Technology to Optogenetics

As conventional discrete LED arrays increase in size beyond just a few LEDs, the ability to individually turn on each LED is impossible unless a major portion of the LED array area is converted to interconnect wiring. For example, individually addressing each discrete LED in an array with x rows and y columns requires a total of x times y

individual connections (Feili, Schuettler, and Stieglitz 2004). Hence, the wiring to individually address even a small 32 x 32 discrete LED array would require 1024 separate connections, both peripheral to and routed within the array, while an x by y resolution TFT active matrix array used in flat-panel displays only requires x plus y connections. For example, a 32 x 32 TFT active-matrix array requires only 64 total external connections, and even fewer if the external connections are multiplexed. Selectively addressing (turning on) only a very small subset of the overall chronic emissive optical array is key given the expected challenges associated with supplying electrical power from a miniature power source placed inside the skull, since power consumption is directly proportional to the number of active (emitting) light sources. In the 32 x 32 array test case with 1024 separate emitters, being able to turn on only one emitter at a time could conceivably reduce power consumption by up to ~1000X. Additionally, having to simultaneously turn on a large number of high-brightness LEDs in a chronic implant can also present a problem with tissue heating (Kim et al. 2013), as well as limit the ability of optogenetic researchers to selectively optically excite and/or silence small, localized regions of neural tissue.

Flexible OLED Display Technology for Optogenetics

As illustrated in Figure 58, the primary difference between a discrete LED array and an active matrix OLED display array is the addition of thin-film access transistor TFT1, source follower transistor TFT2, and storage capacitor Cs (2T1C) in each emissive OLED pixel, while a discrete LED array uses just one LED (plus interconnect wiring) per pixel. In an active-matrix OLED array, these three thin-film devices provide the

individual addressability (turn on) function for the emissive OLED in each pixel. To address or select an individual pixel in an OLED display, the gate line connected to the OLED pixel is first asserted, turning on TFT1 (Figure 58).

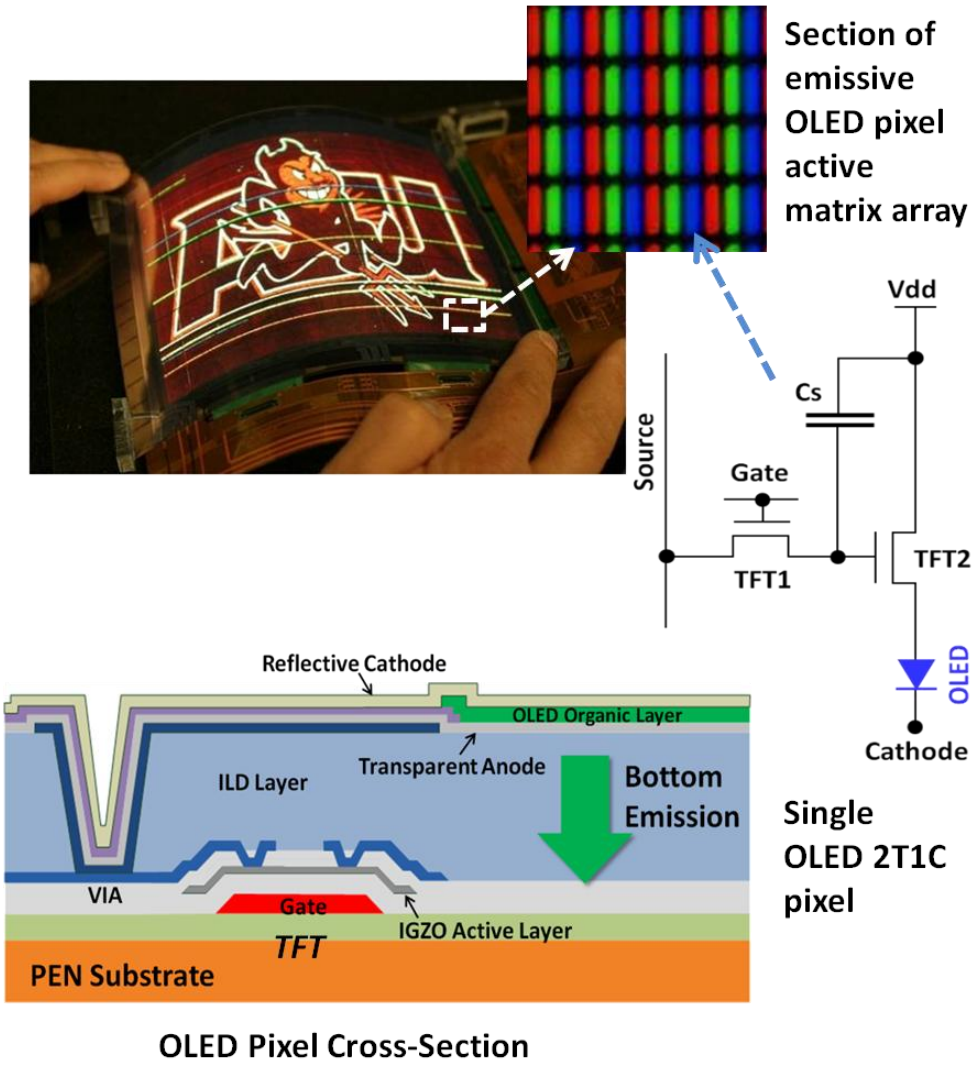

Figure 58. Flexible color OLED display technology.

This transfers the signal voltage from the source line to the storage capacitor Cs. TFT1 is then switched off (gate line goes low), and the signal voltage stored on Cs is

applied to the gate of source follower TFT2. The OLED now emits a bright light proportional to the current supplied by source follower TFT2 (Sarma 2003), which exits out the bottom of the device through the transparent ITO anode and through the bottom of the transparent PEN plastic substrate. Higher OLED current directly translates to a brighter pixel, with the OLED current and luminance proportional to the voltage applied to the TFT2 gate electrode.

Unlike conventional discrete LED optogenetics array approaches, the OLED, TFTs, and pixel capacitor are not separate discrete components; instead, they are integrated on the same substrate and formed using micron and sub-micron scale-patterned layers during the flat-panel display TFT manufacturing process sequence (Marrs et al. Oct 2011, Raupp, O'Rourke, O'Brien, et al. 2007, Venugopal et al. May 2010). Similar to the flexible digital x-ray detectors discussed earlier, chronic in vivo applications also require the emissive OLED array to be both conformable and shatterproof (Smith, Marrs, et al. 2013). Again, a flexible Dupont Teijin Films Teonex® PEN transparent plastic substrate (Haq et al. 2010) is used for this new bio-related flexible electronics application. Using a thin and flexible substrate with all the components integrated on the same substrate allows the implanted flexible OLED and thin-film transistor (TFT) active cortical array to be thin enough to sit below the brain's pia mater and could allow it to be placed in direct contact with the cortical surface.

Experimental Details and Device Fabrication

To demonstrate the initial viability of applying flexible OLED display technology to optogenetic applications, determining whether flexible OLEDs can emit a bright

enough light to induce optical stimulation in modified neural tissue was necessary. Literature reports that blue light centered at approximately 450 nm is the optimum wavelength to activate modified neurons expressing ChR2 (Kim et al. 2013, Mattis et al. 2012), which (fortunately) very closely matches the wavelength and electroluminescent spectrum (Figure 6) of the 455 nm blue OLEDs used in our existing flexible color OLED display. For this effort, bottom-emitting blue OLED test structures, shown in the Figure 59 photograph, were fabricated on flexible PEN plastic substrates at the ASU FDC 6″ pilot line using the same flexible 455 nm blue OLED device technology illustrated in Figure 58 (Haq et al. 2010). Deposition of all thin-film layers was performed in an OLED deposition tool from Angstrom Engineering Inc. The detailed OLED device structure used is shown in Figure 59, while the simplified version, including the PEN plastic substrate, is illustrated in the Figure 58 OLED pixel cross-section.

The detailed, fluorescent-blue OLED device structure consists of injection, transport, and blocking layers, along with the emission layer. These are abbreviated as HIL (hole injection layer), HTL (hole transport layer), HBL (hole blocking layer), ETL (electron transport layer), and EIL (electron injection layer). A reflective aluminum layer is used to form the cathode, and the anode is a transparent ITO layer located directly under the HIL. The emissive layer used for this effort is a single host doped with a blue fluorophore, in which the injected electrons and holes recombine to emit (bright) blue 455 nm light, which exits out the bottom of the device through the transparent ITO anode and then the transparent PEN plastic substrate as shown in Figure 58. To change the emitted color (wavelength), different dopant materials can be used to create red or green OLEDs.

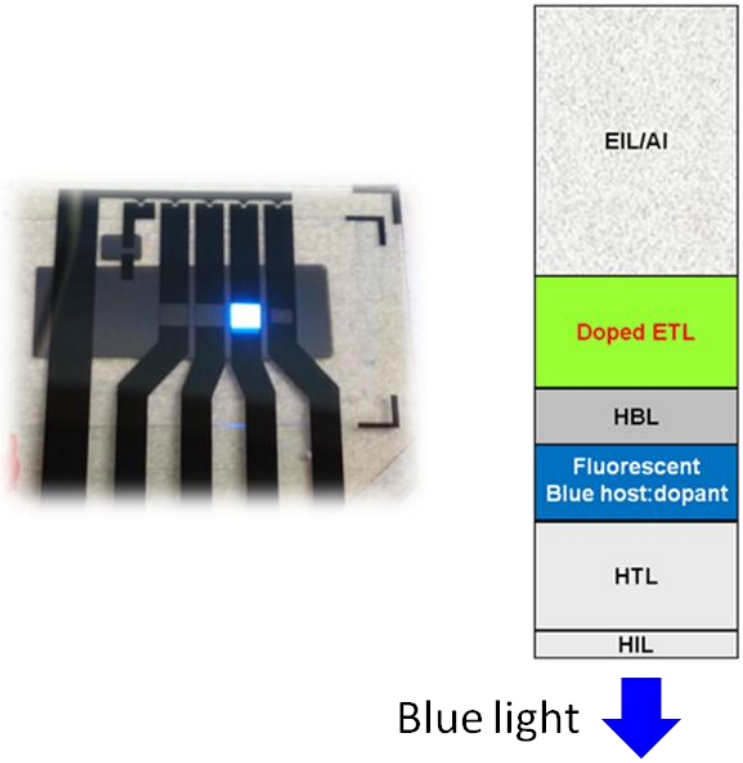

Figure 59. Flexible 4 mm2 bottom emitting 455 nm blue OLED test structure used for this work, and detailed fluorescent blue OLED device structure, with scaled organic layer thicknesses.

Optical characterization by Y.K. Lee and B. O'Brien was performed using the singulated 4 mm^2 emissive area OLED test structures after debonding the flexible plastic substrate from an alumina carrier. Electroluminescence (EL) optical spectra were taken using an Ocean Optics HR4000CG spectrometer. Luminance vs. voltage (L-V) data was collected using a Newport optics 818-UV photodiode and Keithley 2400 source meter, with measurement techniques defined by Forrest et al. (Forrest, Bradley, and Thompson 2003).

High Light Intensity Pulsed Blue OLED Development

From literature, a minimum of 1 mW/mm^2 of instantaneous pulsed irradiance at a wavelength of ~450 nm is required to induce optical stimulation in genetically modified neural tissue (Kim et al. 2013, Degenaar et al. 2010).

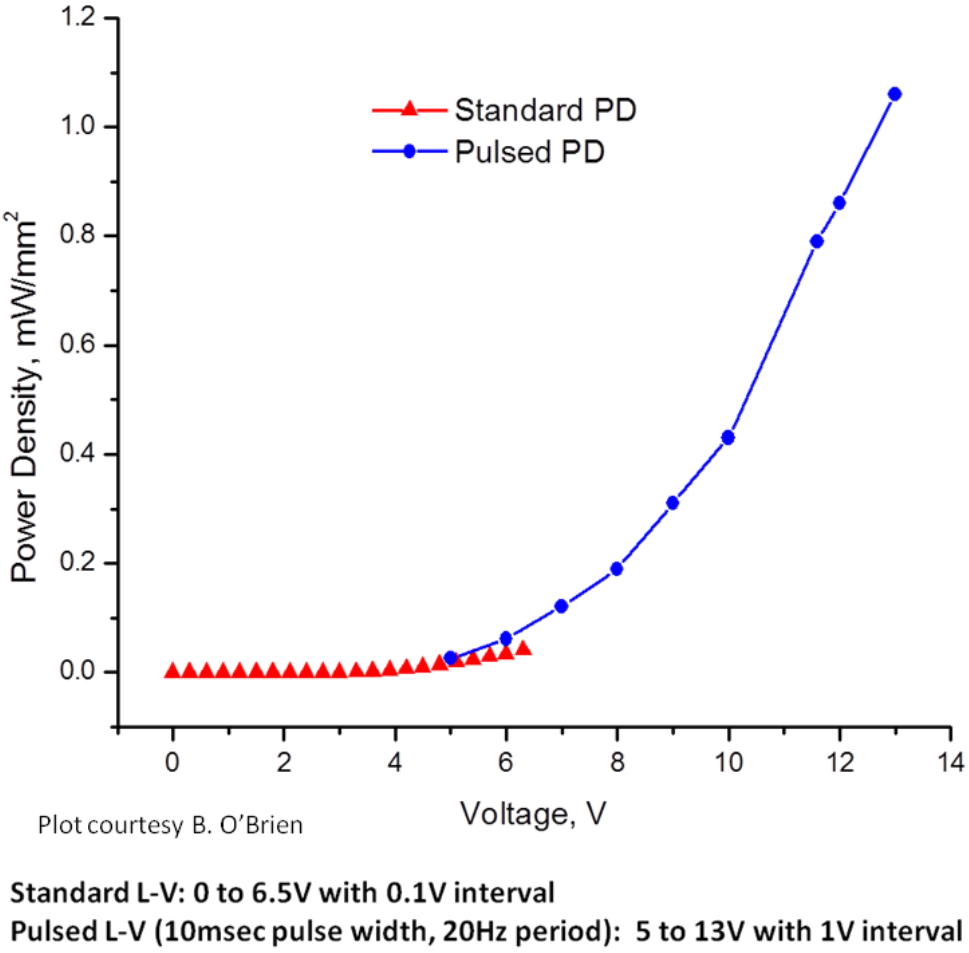

Figure 60. 455 nm Blue OLED optical power density as a function of forward bias. Optical power density - Luminance vs. Voltage (L-V) plot - under continuous DC (Standard) and pulsed mode operation, demonstrating 1mw/mm2 of light intensity for pulsed mode operation.

Referring to Figure 60, the required instantaneous light intensity of 1 mW/mm^2 is approximately 10X greater than the intensity of 0.1 mW/mm^2 observed from an existing bottom-emitting 455 nm blue OLED using a typical bias condition of 7 volts DC, common to commercial flat-panel OLED displays. This is the standard power density (PD) luminance vs. voltage (L-V) curve in Figure 60. Similar to a semiconductor diode, increasing the voltage across an OLED will exponentially increase the current through the OLED, which will significantly increase the OLED brightness. However, increasing the DC bias above 7 volts to obtain a higher instantaneous light intensity was shown to degrade the organic emission layers in the OLED due to current-induced, localized joule heating in the OLED organic layers (Wilkinson et al. 2001). As shown in the figure, the (diode) current increases exponentially with voltage. Fortunately, we discovered that by pulsing the OLED power supply (E. Bawolek, B. O'Brien, and Y.K. Lee), the OLED operating voltage can be significantly increased and subsequently increase the instantaneous light intensity without degrading or damaging the OLED organic layers (Pulsed PD curve in Figure 60).

Nakanotoni et al. reported high current densities of over 1000 A/cm^2 using pulsed operation (Nakanotani et al. 2005), but noted that a substrate with high thermal conductivity was required. Unlike glass, PEN plastic substrates have an inherently low thermal conductivity, and another method for thermal control was required. We found that using a thin, conformal heat sink—in our case, a thin 30μm flexible metal foil bonded to the back of the reflective cathode—will keep the OLED device temperature low while still preserving device flexibility. Keeping the pulse width short and operating at a low frequency also appears to give the organic layers in the OLED a chance to

recover and cool down before applying a voltage bias in the next period. Essentially, the OLED for this particular biophotonic application is only operated until it starts to heat up; then it is turned off and given a chance to cool before being turned on again.

Referring again to Figure 60, the required 1 mW/mm^2 of instantaneous light intensity was achieved using a 13 volt, 20 Hz pulse with a 10 msec pulse width. Because pulsing the supply voltage (Vdd) on a flat-panel display will induce undesirable flicker in the displayed image on an OLED display, it is not used in commercial displays to increase the emitted light intensity. Hence, for this application, pulsing the OLED display at lower frequencies is not an issue (a human doesn't need to look at it), and also aligns well with the reported 20 Hz pulsed operation conditions used to drive discrete LEDs in optogenetic applications (Kim et al. 2013).

Pulsed Mode OLED Display Architecture

Clearly, pulsed-mode operation of an OLED array is required for this particular application. However, the active-matrix OLED pixel circuit used in conventional flat-panel displays is designed to only operate correctly under static DC biasing; it will not work correctly in the required pulsed mode. A solution required the design of a new OLED pixel circuit, shown in Figure 61, in which the OLED supply voltage Vdd is now pulsed on and off, as opposed to being held at a static DC bias as in conventional emissive OLED displays. The revised pulse-mode OLED pixel circuit again includes an access transistor TFT1, source-follower transistor TFT2, and storage capacitor Cs, similar to a conventional OLED display (Sarma 2003) in Figure 58. But in the new Figure 61 configuration, Cs is now connected to ground instead of Vdd. This prevents the stored Cs

voltage from being bootstrapped up to Vdd (and turning the OLED on) when 0 volts is stored on Cs, and Vdd is pulsed high.

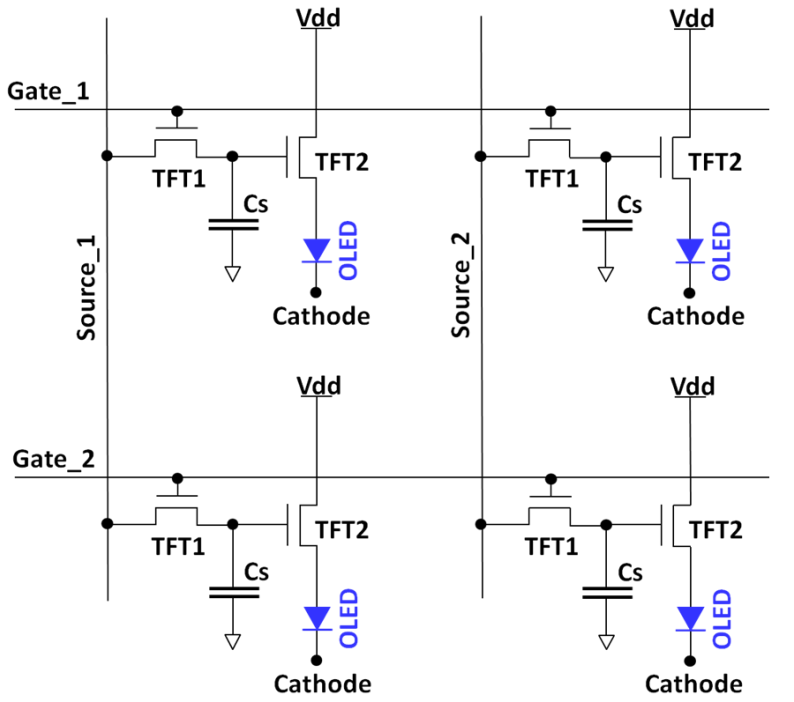

(a)

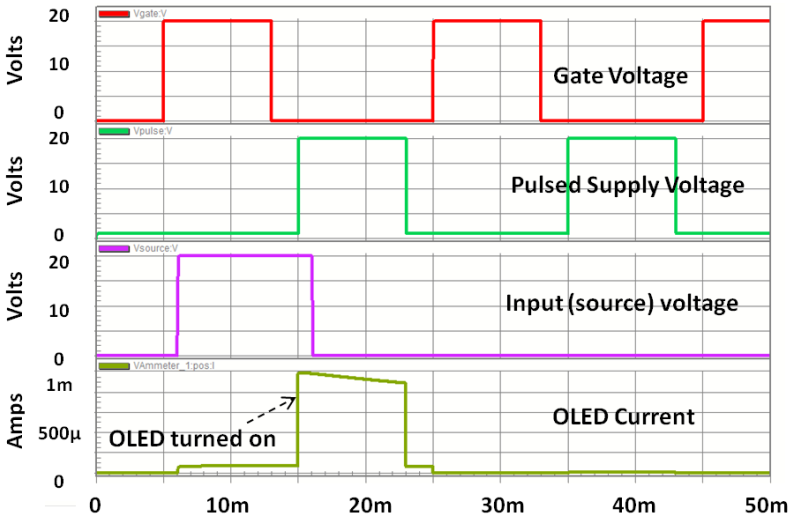

(b)

Figure 61. Active-matrix-array circuit for pulsed operation. (a) Active matrix array 2T1C pixel circuit for pulsed Vdd supply voltage operation, and (b) corresponding timing diagram from circuit SPICE simulation for pulsed mode OLED operation.

Functionality in pulsed-mode OLED operation is illustrated by the timing diagram (Figure 61b) generated from a SPICE simulation of the OLED pixel circuit (Figure 61a). To start, a positive gate voltage is first applied to the gate electrode of TFT1, turning TFT1 on. This transfers the input voltage from the source line, where it is then stored on capacitor Cs. TFT1 is then switched off (gate line goes low at 13 ms in figure 5b), and the signal voltage stored on storage capacitor Cs is now available to the gate of source follower TFT2.

A key feature of the new pulsed-mode circuit is that while writing the entire active-matrix array, the supply voltage Vdd is turned off. This is necessary to turn off source follower TFT2, which correspondingly keeps the OLED from turning on and emitting light. After the entire active-matrix array is written by sequentially addressing all of the gate lines, Vdd is now turned on (at 15 ms), as shown in the timing diagram. OLEDs in pixels with a voltage stored on Cs are also turned on at 15 ms, and those without a voltage stored on Cs (0 volts) are not. This sequential operation provides the ability to individually address (write to) all pixels in the array, as well as support the required pulsed-mode operation. Referring again to the pulsed-operation timing diagram (Figure 61b), at 23 ms the OLED turns off a second time after Vdd is turned off. At an array level, this would be the start of another write cycle to the entire array. The timing sequence is repeated, but with 0 volts (off state) from the source line written onto Cs the next time the gate is pulsed on. When the Vdd is pulsed on again at 35 ms, there is no current flowing through the OLED (it is off and doesn't light up). To illustrate the array-level connections, a small 2 x 2 resolution active matrix pulsed OLED array schematic

diagram is provided in the same figure. In practice, much higher-resolution addressable arrays are envisioned or assumed.

Flexible OLED Display Biocompatibility

In parallel with the pulsed-mode operation development work, flexible OLED display biocompatibility, and long-term in vitro durability were also evaluated for use in this application. As illustrated in Figure 62, biocompatibility was successfully demonstrated by the ability to grow immortalized human epithelial cells on the surface of a full TFT process-flow PEN flexible-display substrate (Blain Christen). For in vitro durability, we discovered that EtOH sterilization was required for the blue OLEDs, as opposed to a more conventional 121°C autoclave steam sterilization, which was observed to damage the OLED organic layers and subsequently degrade optical performance.

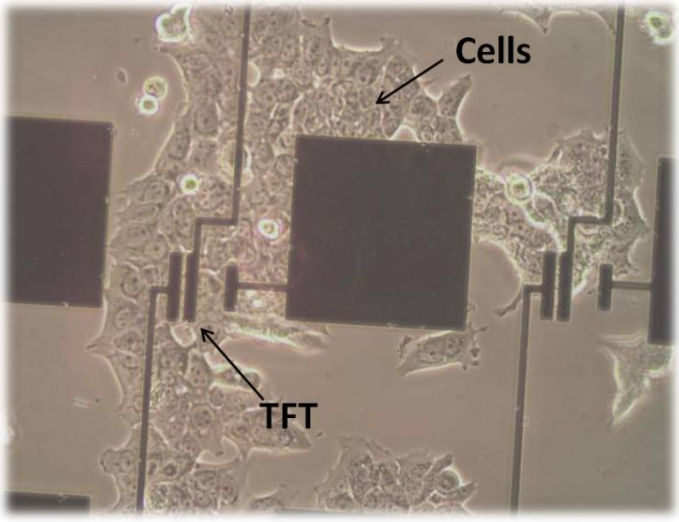

Photo provided by J. Blain Christen

Figure 62. Flexible OLED display biocompatibility. Human breast cancer cells (SKBR3) growing on flexible plastic TFT substrate to demonstrate biocompatibility and durability for in vitro culture studies.

This effect of autoclave sterilization on OLED performance is shown in Figure 63.

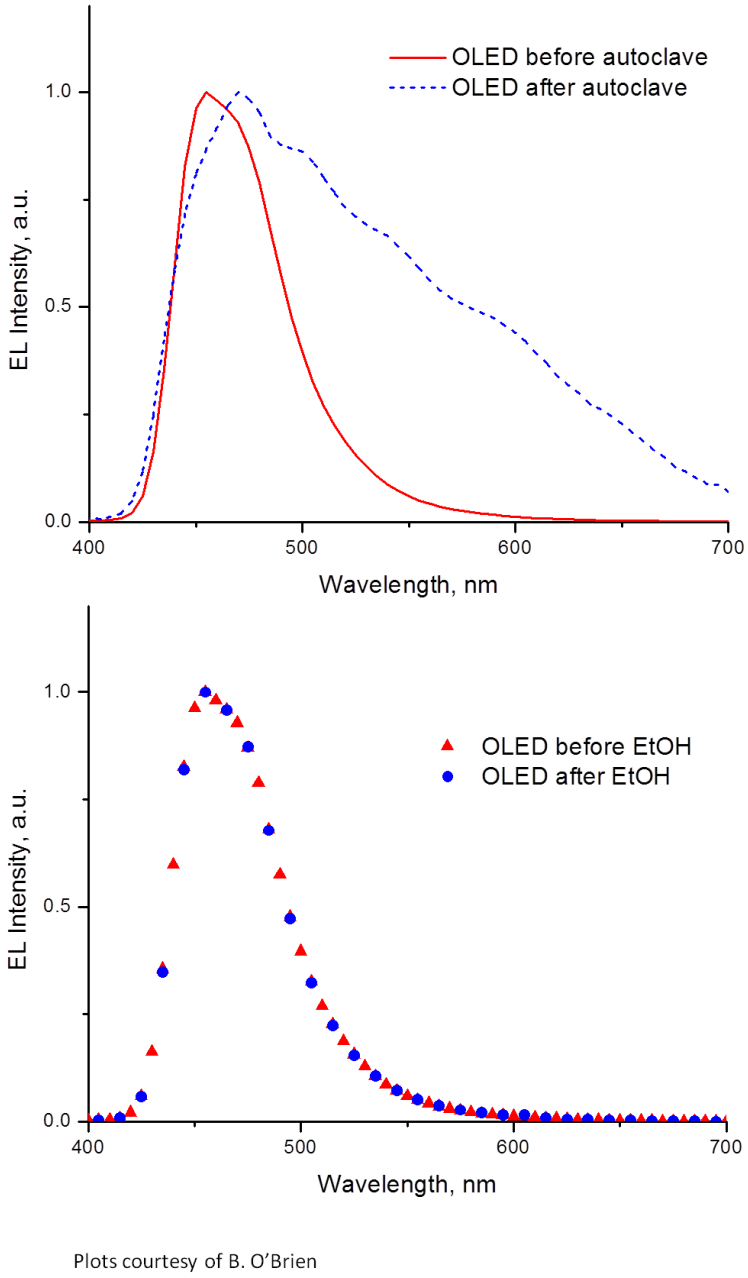

Figure 63. OLED biological durability after sterilization. 455 nm Blue OLED electroluminescence before and after 121°C autoclave sterilization. Blue OLED damaged, with color changed to white after the autoclave (top). Electroluminescence before and after EtOH treatment followed by one week in 37°C incubator, while immersed in cell culture media (bottom). No change observed.

Interestingly, after autoclave sterilization, the blue OLED was essentially turned into a white OLED, as shown by the spread in the OLED emission spectrum after sterilization. The assumption is that the 121°C autoclave temperature is damaging the OLED organic layers. As a solution, in vitro durability tests of the blue OLED test structure were repeated, but using EtOH sterilization instead. The OLED test structure was then immersed in cell culture media and placed in a 37°C incubator for one week. Optical characterization tests immediately after removal from the incubator showed OLED optical EL performance unaffected.

The other key issue for biocompatibility is ensuring that the operating temperature at the surface of the blue optical emitter under 1mW/mm^2 pulsed mode is compatible with living brain tissue. As reported by Kim (Kim et al. 2013), reducing the individual emitter area to cellular scale dimensions results in a rapid drop off in device operating temperature thanks to heat sinking by the surrounding biological tissue and fluids. For a 25 µm x 25 µm sized cellular scale LED emitter operating at a blue light intensity of approximately 18mW/mm^2, the reported temperature rise was approximately 0.3°C at 10Hz (Kim et al. 2013). This is well below the 1 to 2°C increase in temperature required to create a physiological response in neural tissue (Elwassif et al. 2006). Substituting the reported cellular scale 25 µm x 25 µm LED emitter with a similar sized blue OLED pixel, but now operating at only 1 mW/mm^2, the predicted temperature rise is also expected to be low and estimated to be less than 0.3°C. This also accounts for the approximately 6X lower conversion efficiency in our blue OLEDs as compared to reported blue micro-LEDs used by Kim (Kim 2012).

Clinical Impact

The technology for optogenetics as a future chronic treatment in humans is severely lacking, given the reported inability to selectively optically excite or silence individual neurons using a large, high-resolution emissive array. While smaller arrays for optical stimulation (Kim et al. 2013) have been demonstrated, they have been created in technologies that do not allow for low-power brain-scale implementation. The integration of flexible OLED display technology with biological systems is designed to offer a viable avenue for future chronic in vivo implantation of the latest optogenetics therapies, which could lead to treatments for epilepsy, stroke, seizures, paralysis, depression, schizophrenia, Parkinson's disease, and Alzheimer's disease. Seizure control and suppression provides one particularly illustrative application for this new approach.

Conceptually, a portion of the cortical surface would be covered with the dual-mode flexible OLED optogenetics implant illustrated in Figure 64. At the onset of a seizure, the precise location or origin of the seizure on the cortical surface would be detected by a co-axial pitch-matched flexible integrated microelectrode array (MEA) pressed against the cortical surface. Signal processing would then identify the location and sequence of individual OLED pixels to activate, followed by initiation of the spatiotemporal optical stimulation sequence to quiet the affected neurological regions before the incipient seizure can spread to a larger portion of the cortex.

Conceptual Dual-Mode Flexible Electronics Optogenetics Pixel

Since applying pulsed blue light activates only cells expressing ChR2, an enhanced configuration would also supply pulsed yellow light to cells that express

Halorhodospin to quiet or silence them. This leads to an alternate conceptual optogenetics pixel configuration, in which a multi-color pixel, instead of just a monochromatic blue OLED pixel array, is provided to enable both localized and addressable optical activation using blue light, as well as silencing of neural activity using yellow light (Figure 64).

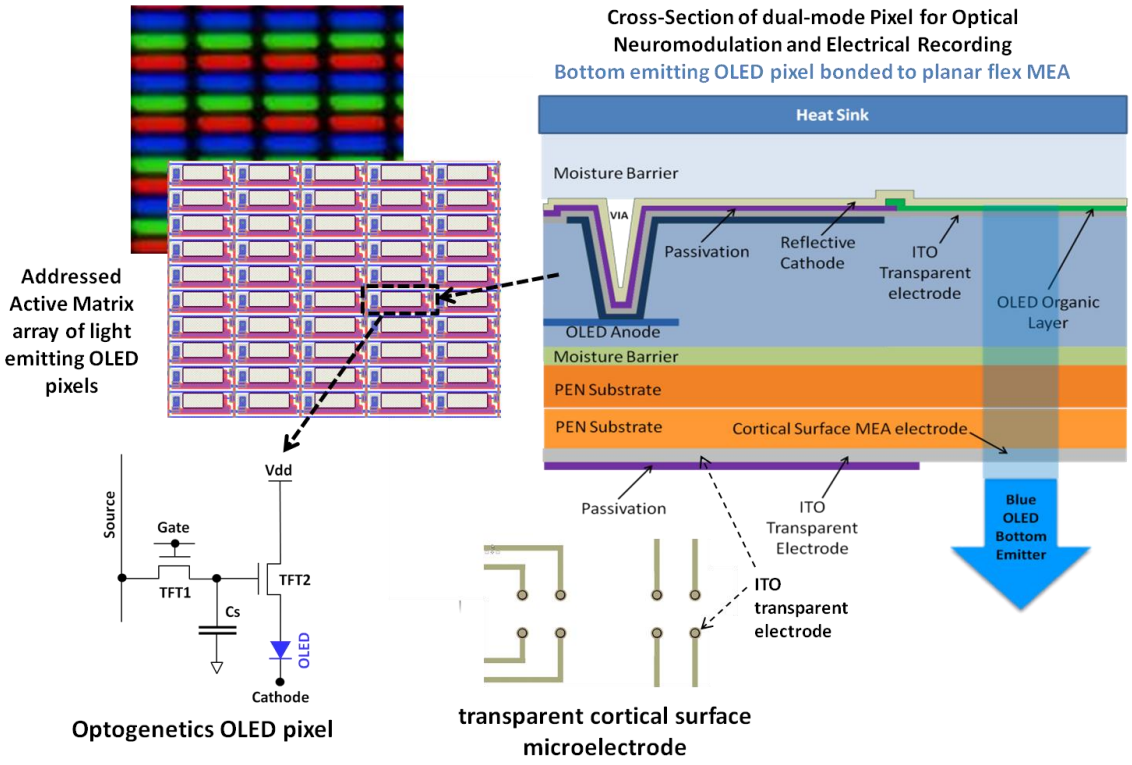

Figure 64. Multicolor dual-mode optogenetics pixel.

To add the ability to detect electrical activity, a bottom-emitting, flexible OLED pixel is bonded, using optically clear adhesive, to a pitch-matched, transparent ITO microelectrode which then mates to the cortical surface. This dual-mode concept delivers light simultaneously with the electrophysiological detection of biopotentials from optically stimulated neural tissue. Since light delivery can be localized by just turning on

individual pixels in the array for precise spatial and temporal control, isolated neurological effects can now be monitored and recorded while being optically stimulated.

Summary

The initial viability of applying flexible color OLED display technology using pulsed-mode operation for an emissive high-resolution array on a thin, mechanically compliant, biocompatible plastic substrate to selectively stimulate and/or silence small groups of neurons for chronic optogenetic applications was demonstrated. Envisioned future research would first verify whether 1 mW/mm^2 of pulsed blue light from the simple OLED test structure shown in Figure 59 can optically stimulate or excite neurons in vitro using neural tissue expressing ChR2. Based on earlier research (Kim et al. 2013), the demonstrated pulsed OLED intensity of 1 mW/mm^2 is expected to be sufficient, but the assumption is that a laboratory trial is required to demonstrate the early viability of applying flexible OLED display technology for future low-cost, minimally invasive chronic optogenetics applications.

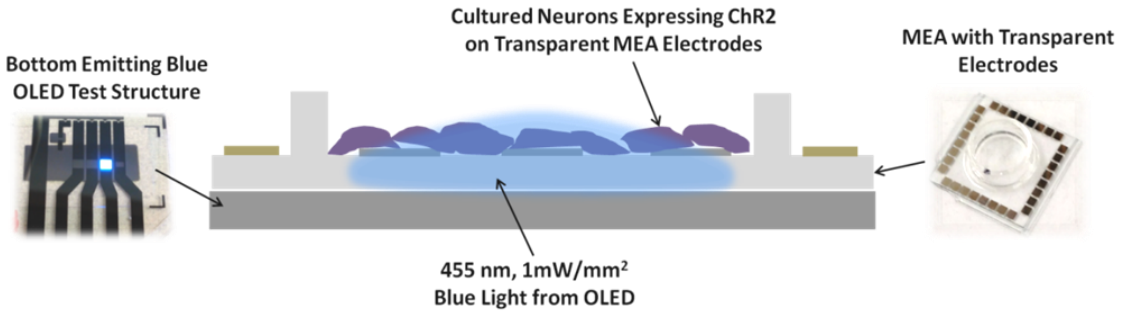

Figure 65. Optogenetics microelectrode array (MEA) test configuration.

As illustrated in Figure 65, ChR2-expressing cells would be cultured on the surface of a conventional transparent MEA. A bottom-emitting blue OLED test structure with 4 mm^2 emissive elements would then be positioned directly underneath the MEA, and then activated to optically stimulate the cultured neurons using 5 to 20 Hz, 1 mW/mm^2 pulsed blue light. Electrical activity of the blue OLED optically stimulated neurons would then be monitored from the transparent MEA electrodes and evaluated for correlation with the incident light pulse from the OLED emitter.

CHAPTER 7

DISPOSABLE POINT-OF-USE OPTICAL BIOSENSOR

Don’t just go for safe projects. Take on the really tough problems

Warren Buffet

This work reports on a new point-of-use optical biosensor designed to detect multiple biomarkers at the point-of-use. The concept leverages fluorescence measurement-based biorecognition in combination with OLED display and a-Si:H PiN photodiode active matrix array technology to provide diagnostic laboratory sensitivity for multiple pathogen or disease detection in a compact configuration that is inexpensive to manufacture and disposable after one use, similar to a home pregnancy test kit. Sensor feasibility and optical performance were evaluated using a 0.3mW/mm^2, 455nm blue OLED emitter configured first with orthogonally crossed linear polarizing film; and second, with band-pass and long-pass optical filters. Measurements indicated that the sensor requires the optical filters to approach the sensitivity of diagnostic laboratory fluorescence measurement-based instrumentation.

Fluorescence-Based Biorecognition

Biorecognition using fluorescence measurement-based detection is a high sensitivity diagnostic technique that typically looks for antibody biomarkers in blood serum specific to particular diseases or pathogens. For example, dengue virus (DENV) infections can be diagnosed by detecting specific IgM antibodies in blood serum

(Emmerich, Mika, and Schmitz 2013). In a typical fluorescence-based biorecognition process, antibodies in a sample are first chemically labeled (tagged) with a fluorophore and are then allowed to dock or bind with a target antigen immobilized on the surface of a downstream detection chamber. The binding of an antibody with its target antigen results in a structure referred to as an immunocomplex or immune complex. This technique is typically called an immunoassay and enables specific antibodies to be detected in the sample by using an immobilized antigen targeted specifically for only the corresponding antibody (2010) (Ferrari 2007). Selectivity to specific antibodies in the sample is provided by the labeled antibodies only binding with a specific antigen (Figure 66).

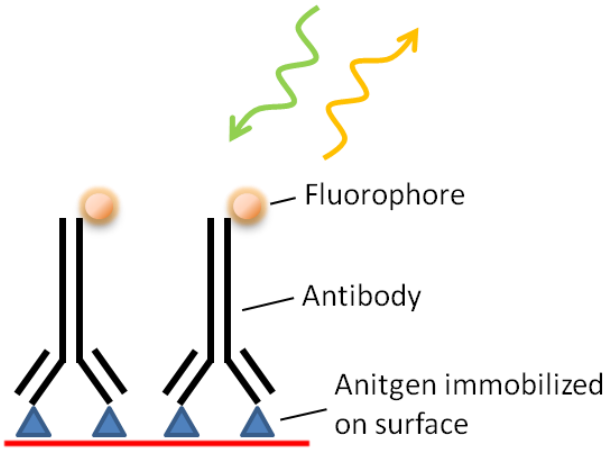

Figure 66. Antibody/Antigen immunocomplex tagged with fluorophore.

The immune complex, formed by the paired antibodies and antigens, is now proportional to the concentration of the antibodies of interest in the original sample. After allowing time for binding, the detection chamber containing the bound antigen/antibody pairs is then illuminated with light of a specific wavelength. The fluorophore labels attached to the antibodies are excited the incident light and then re-emit light (i.e.,

fluoresce) at a slightly longer wavelength, typically about 30 to 50 nm longer. Fluorescence occurs when the fluorophore tag absorbs photons from the excitation light source. This causes a transition to a higher energy state. Light is then emitted by the fluorophore when the absorbed photons return or relax to a lower energy initial state, in typically less than one nanosecond. The intensity of the light emitted, F is dependent on the material properties of the fluorophore, as well as the intensity of the incident light and fluorophore concentration, and is described by the following relationship.

$$F = \varphi I_0(1 - e^{-\varepsilon bc}) \tag{33}$$

Where φ is the quantum (conversion) efficiency, I_0 is the incident light intensity, ε is the fluorophore absorptivity, b is the path length through the fluorophore, and c is the concentration of the fluorophore (Guilbault 1990).

For example, a fluorophore illuminated with green light would typically emit longer wavelength yellow-orange light (Figure 66). The re-emitted light intensity can then be measured using a photodetector to determine the antibody concentration in the sample. Higher emitted light intensity generated by more docked antibody/antigen pairs with fluorophore tags corresponds to a higher antibody biomarker concentration in the original sample.

Related Optical Biosensor Research

Low cost point-of-use disposable biosensors that test for individual biomarkers in biofluid samples, such as blood or urine, are now commercially available. The individual

biomarkers are analyzed to provide an indicator of the disease or physiological state present in the sample, or whether a foreign substance has been introduced. One familiar example are home pregnancy test kits, which detect for the presence of the human chorionic gonadotropin (hCG) hormone biomarker in women's urine (Canfield et al. 1987). Typically these disposable point-of-use biosensors can only test for a very limited number of biomarkers and are not especially sensitive. More complex sample analysis that requires multiple biomarkers, such as testing for multiple diseases or pathogens, or high sensitivity, requires transporting the sample to a diagnostic laboratory for analysis using fluorescent microscopy-based techniques. Recent research has explored methods to miniaturize these more complex diagnostic tests, which would allow them to be moved from the laboratory to the point-of-use (Ligler 2008). These miniaturized medical diagnostic laboratories are traditionally called a lab-on-a-chip (LOC), in deference to their use of manufacturing technology from the semiconductor (chip) industry. Because fluorescence measurement-based analytical methods are widely used in diagnostic laboratories and offer both high sensitivity and selectivity, much of the reported research has focused on miniaturizing the functional equivalent of a fluorescent microscopy lab into a small disposable form factor (Pais et al. 2008). Fluorescence analysis also offers the advantage of applying multiple biological techniques, such as traditional antibody recognitions or quantitative polymerase chain reactions, to identify multiple diseases and pathogens. Since laboratory fluorescent measurement equipment typically uses quite large and expensive optical components such as optical microscopes, lasers, optical filters, and digital cameras, much of the LOC optical biosensor research has concentrated on miniaturizing these particular optical components.

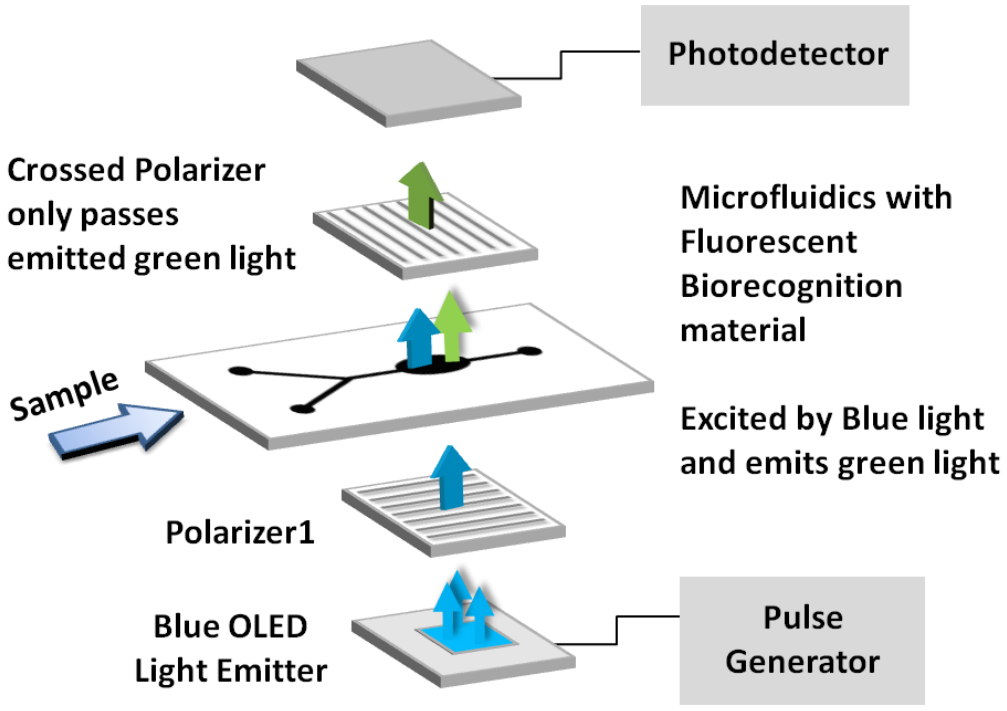

Figure 67. Exploded view of miniaturized face-to-face planar optical biosensor, with integrated OLED light excitation and photodetector for fluorescence analysis

Multiple researchers have reported on a compact configuration using a microfluidic detection chamber sandwiched between a paired organic light emitting diode (OLED) emitter and solid state photodetector (Pais et al. 2008, Ryu et al. 2011, Dixit et al. 2013, Banerjee et al. , George G. Malliaras and Owens 2008). The OLED emitter is used to replace the laser light source, while the photodetector replaces the digital camera. This simple and low cost face-to-face configuration, illustrated Figure 67, also eliminates the need for expensive and bulky microscope optics by mating the photodetector, OLED, and linear polarizers directly to the surface of the transparent microfluidic chamber. In one configuration, blue light from the OLED emitter is first passed through a linear

polarizer (Polarizer1). The polarized blue light then illuminates a small sample detection chamber with a spot of biorecognition material immobilized on its surface.

As shown in Figure 67, a microfluidic assembly with Y-shaped fluid microfluidic channels is positioned directly between the two crossed polarizers. The sample enters a microfluidic channel at one of the legs in the Y, while the other leg of the Y supplies the fluorescent reagents for tagging. The two liquid components are then mixed via diffusion at the intersection (top) of the Y prior to entering the downstream oval shaped detection chamber. Any fluorescent tagged material that binds to the biorecogntion site or spot in the detection chamber is now excited by the incident blue light and then (weakly) re-emits longer wavelength green light. The emitted green light passes through the top linear (crossed) polarizer and is detected by a solid-state photodetector. Polarized blue light from the OLED that passes through the transparent reaction chamber is blocked from reaching the photodiode by the top orthogonally crossed polarizer. This is designed to prevent the weak (green) fluorescence signal from being swamped out by the blue OLED light at the photodetector.

The magnitude of light attenuation through ideal crossed linear polarizers is calculated using Malus' Law (David Halliday 2013):

$$I(\theta) = \frac{I}{2} cos^2\,\theta \tag{34}$$

Where I is the incident light intensity, θ is the angle between the crossed linear polarizers, and I(θ) is the output light intensity after passing through the two crossed

(ideal) linear polarizers, as a function of θ. If the two linear polarizers are orthogonally crossed (90° angle), the predicted amplitude for the transmitted light is zero. For analysis, the detected intensity of the re-emitted (green) light from the fluorophore is now proportional to the concentration of the detected biomarker in the sample, and is ideally not affected or influenced by the light from the source (blue OLED).

However, with only one paired OLED and photodetection, a key limitation of the Figure 67 configuration is the inability to detect the fluorescent signal emitted from more than a single biomarker, which prevents this configuration from detecting more than one disease or pathogen. Additionally, a small fraction of patients tested will present only a specific antigen. Hence, a biomarker diagnostic test based on just one antigen can demonstrate poor sensitivity. To improve the predictive value, testing multiple combinations of biomarkers in parallel is typically required. As also will be shown, the crossed linear polarizer configuration is not particularly sensitive.

New Approach Using Active Matrix TFT Technology

One conceptually straightforward approach to increase the number of detectable biomarkers from a single sample is to increase the number of paired light sources and photodetectors. For example, an 8 x 8 array of individual light sources paired with an 8 x 8 array of photodetectors could theoretically detect 64 individual biomarkers, in combination with a microarray using 64 separate biorecognition sites. However, arrays using conventional discrete components can quickly get quite large, which is an issue for low cost disposable applications. For example, an 8 x 8 array of Vishay TEMD6010FX01 discrete surface mount PiN photodiodes, each of which has a footprint of 4 x 2 x 1.5 mm

(L x W x H), would require a multi-layer printed circuit board (PCB) between one and two inches in diameter, and a similarly sized microfluidic detection chamber. This in an order of magnitude larger in fluid volume than typical low cost disposable microfluidics and is expected to be problematic for analyzing small sample volumes, such as a small drop of blood from a single finger stick.

To address this limitation, active matrix, thin-film transistor (TFT) array technology, from the flat panel display and digital x-ray imager industry is one new approach which can be applied to extend earlier work on single biomarker disposable biosensors to enable low cost multi-biomarker detection. For example, a typical flat panel display or PiN photodiode pixel size is approximately 200 ums (O'Brien et al. 2013, Smith, Marrs, et al. 2013, Marrs, Bawolek, O'Brian, et al. 2013). Hence, an 8 x 8 array of 64 pixels using flat panel active matrix technology is now less than 2 mm. Paired and pitch matched to the light emitter and photodiode active matrix arrays would be an 8 x 8 microarray of fluorescent biorecognition sites deposited on the surface of the microfluidic detection chamber. This new microarray-based fluorescent-based optical biosensor configuration is now small enough to work with the <100uL limited biofluid sample volumes available from a typical finger stick.

For this work, organic light emitting diode (OLED) display technology was selected for the emissive light source. As illustrated in Figure 68, an OLED active matrix display consists of an array of emissive light emitting elements (pixels). The OLED pixel shown includes two thin film transistors (TFTs) and a capacitor, which are used to individually address (i.e., turn on) each OLED pixel in the array (Sarma 2003). The thin OLED organic layer emits a bright light when a forward voltage bias is applied across the

transparent anode and reflective cathode terminal, with the color of the emitted light emitted a function of the materials in the OLED organic layer, and the light intensity a function of the OLED forward bias current.

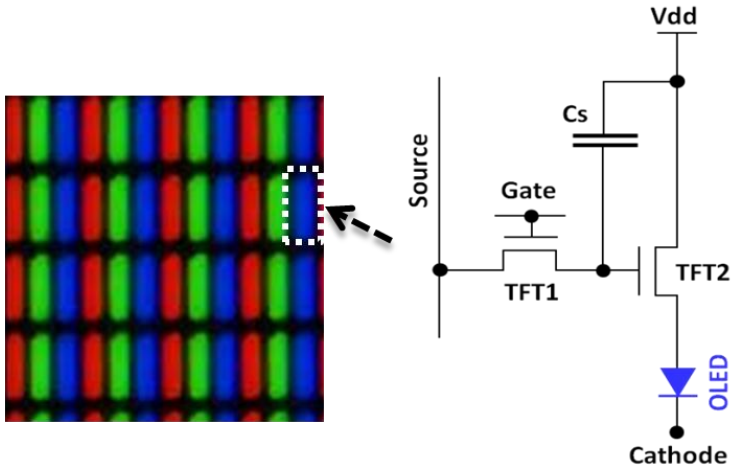

Figure 68. OLED display pixel, with a region magnified to highlight one of the individual three color OLED pixels along with the two TFT, 1 capacitor (2T1C) circuit schematic.

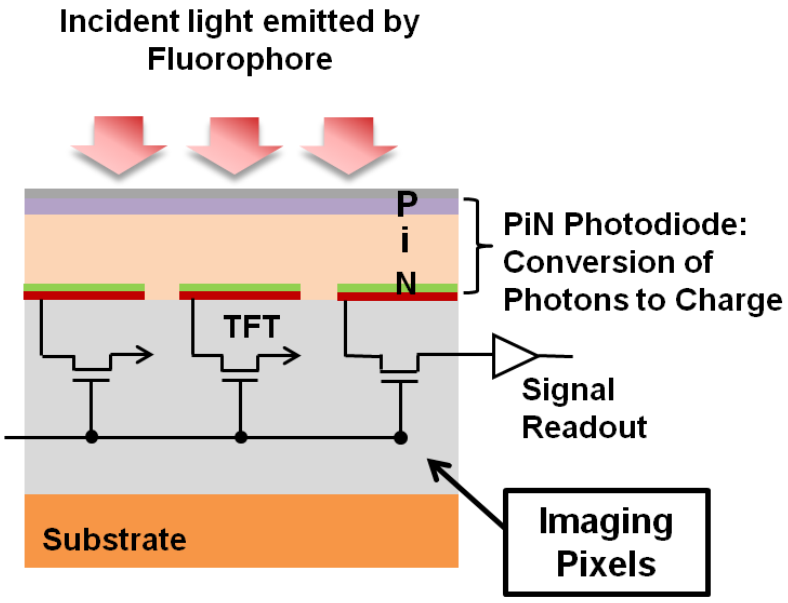

Figure 69. Photodiode detector active matrix array architecture

For the opposing and pitch matched PiN photodiode active matrix sensor array, each pixel in the array has one TFT transistor and a PiN photodiode (Figure 69). The TFT functions as an on/off switch that electrically connects the PiN photodiode to the signal readout when a positive voltage is applied to the gate electrode of the TFT.

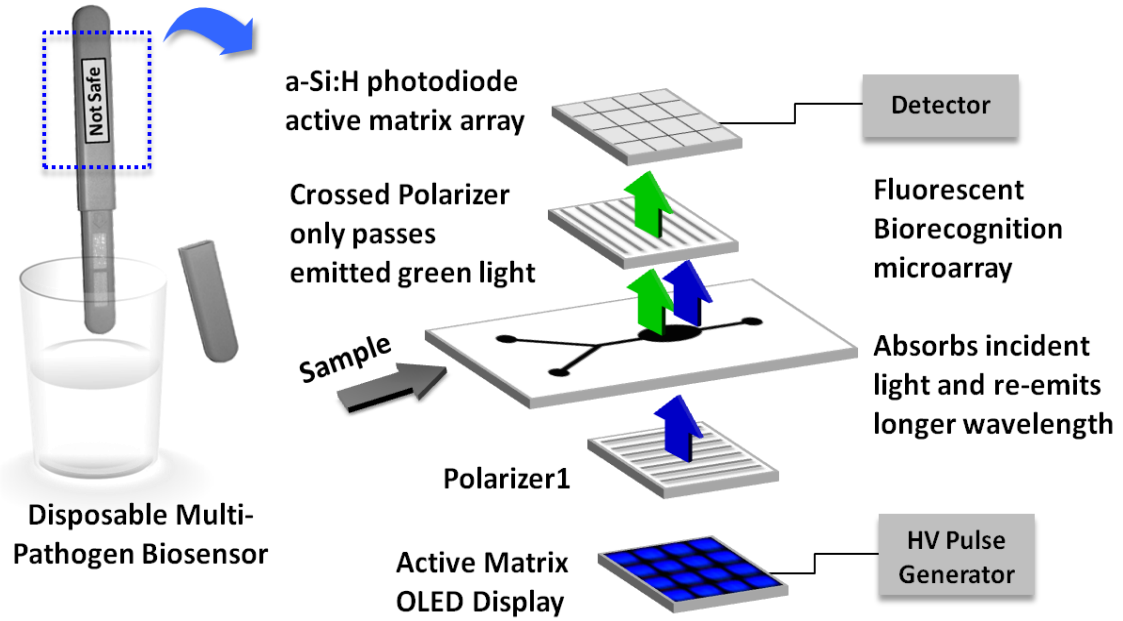

Figure 70. Exploded view of Lab-on-a-chip concept configuration using OLED display for optical excitation and a-Si:H PiN photodiode detector 4 x 4 active matrix array for fluorescence analysis of multiple (16) biomarkers.

At the same time each of the OLED pixels is activated sequentially, opposing PiN photodiode pixels in the separate photodiode active matrix sensor array will also be sequentially selected and the detected optical signal from each individual photodiode would be read out and recorded using an external CMOS integrated circuit. In operation, the OLED pixels in an active matrix array will be activated (turned on) sequentially to illuminate the individual immobilized fluorescent biorecognition sites in the microfluidic detection chamber (Figure 70).

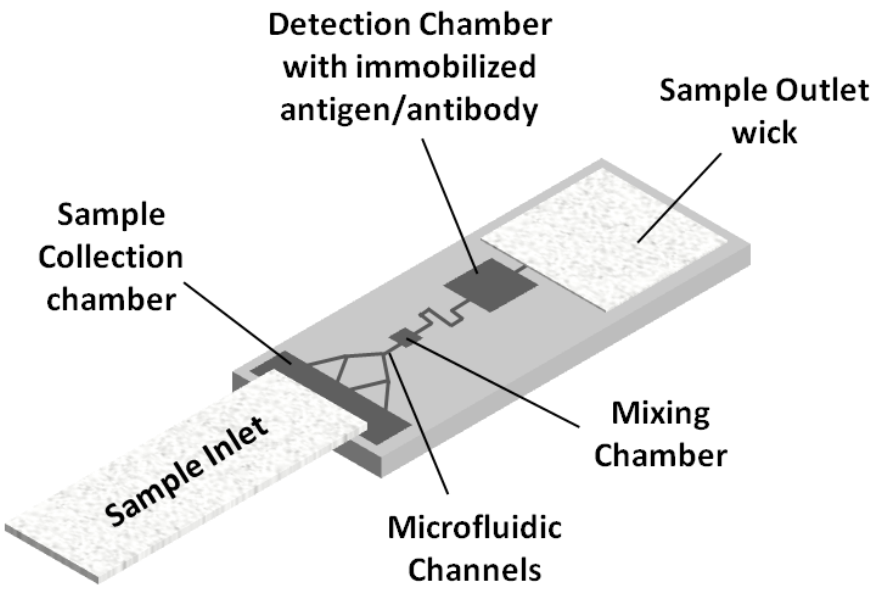

Figure 71. Concept for production version of the disposable microfluidic assembly.

Instead of the Y-shaped fluid channel for the microfluidic assembly, which uses separate sample inlet and reagent chambers, a production injection molded plastic version would likely use a simplified and low cost disposable microfluidic configuration similar to Figure 71. In this simplified configuration, the starting (liquid) sample is collected using a highly absorbent piece of blotter paper that is attached to sample collection chamber at the inlet of the microfluidic assembly. In operation, the user would place the blotter paper in the sample of interest, such as a glass of water. The water is then absorbed by the blotter paper and collected in the integrated microfluidic sample collection chamber to start the diagnostic process sequence. Passive capillary action draws the fluid sample from the collection chamber through the microfluidic channels towards the down steam detection chamber. As shown in the figure, after the collection

chamber, the starting sample then enters a mixing chamber, where the liquid sample could reconstitute dried fluorescent-labeled antibody or antigen beads (Ryu et al. 2011).

A serpentine channel, immediately down steam from the mixing chamber, is then used to delay the sample and provide enough time for the antigen/antibody reaction between the sample and the dried fluorescent labeled material to complete before reaching the downstream detection chamber. When the now fluorescently labeled sample reaches the detection chamber, it is captured by a second antibody or antigen immobilized on the surface of the detection chamber to complete the identification of the biomarkers or pathogens in the starting sample. A downstream sample outlet wick, which is a large and thick piece of blotter paper, is then used to draw off any excess liquid as well as clear the detection chamber of un-reacted material. As described previously, the detection chamber is now sequentially illuminated by each OLED pixel in the array and the concentration of each antigen or antibody present in the sample is proportional to the intensity of light emitted from the labeled antibody/antigen immunocomplex that is detected by the opposing PiN photodiode pixel.

In terms of cost as a function of display size, commercial OLED display technology currently costs about 80 cents/cm^2 (2014c). Even with the addition of peripheral circuitry, input/outputs (I/O's), plus the opposing PiN photodiode array - less than a few square centimeters of display substrate area will be required for each multi-pathogen disposable sensor. This keeps the projected sensor component cost for the integrated OLED display and photodiode active matrix array on the flexible electronics substrate to less than 2 dollars, which is estimated to be more than an order of magnitude cheaper than using discrete components.

Preliminary Experimental Results and Discussion

To evaluate the initial viability of the concept, the single OLED emitter configuration using orthogonally crossed linear polarizing film was first mocked up using a 2 x 2 mm 455 nm blue OLED emitter manufactured at the ASU Flexible Electronics and Display Center. The OLED was operated in 6 Hz pulsed mode, with a 9 volt bias. This provides an instantaneous illumination intensity of 0.3 mW/mm^2, which is approximately 300X brighter than the OLEDs used in previously reported crossed polarizer optical biosensor configurations [6]. As discussed in the earlier Optogenetics chapter, pulsing the power supply allows the OLED operating voltage to be increased. This significantly increases the instantaneous light intensity from the OLED without degrading or damaging the OLED organic layers (Wilkinson et al. 2001, Smith et al. 2014).

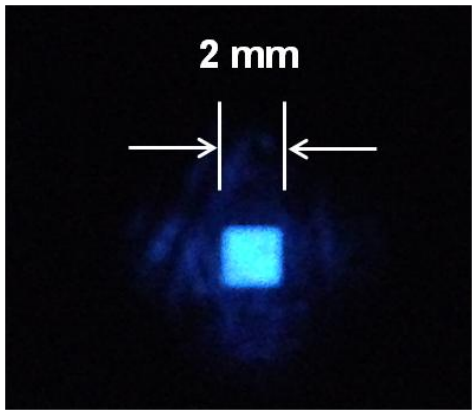

Figure 72. Optical photographs demonstrating the approximately 10^4 of optical attenuation from two sheets of orthogonally crossed linear polarizing film placed on top a bright 0.3mW/mm2, 2 x 2 mm blue OLED emitter.

Optical performance using orthogonally crossed linear polarizers placed on top of the 2 x 2 mm blue OLED is shown in Figure 72. As evident in the low magnification

optical photograph, the crossed linear polarizers did not completely block the blue light from the 2 x 2 mm OLED, with quite a bit of blue light from the OLED readily visible.

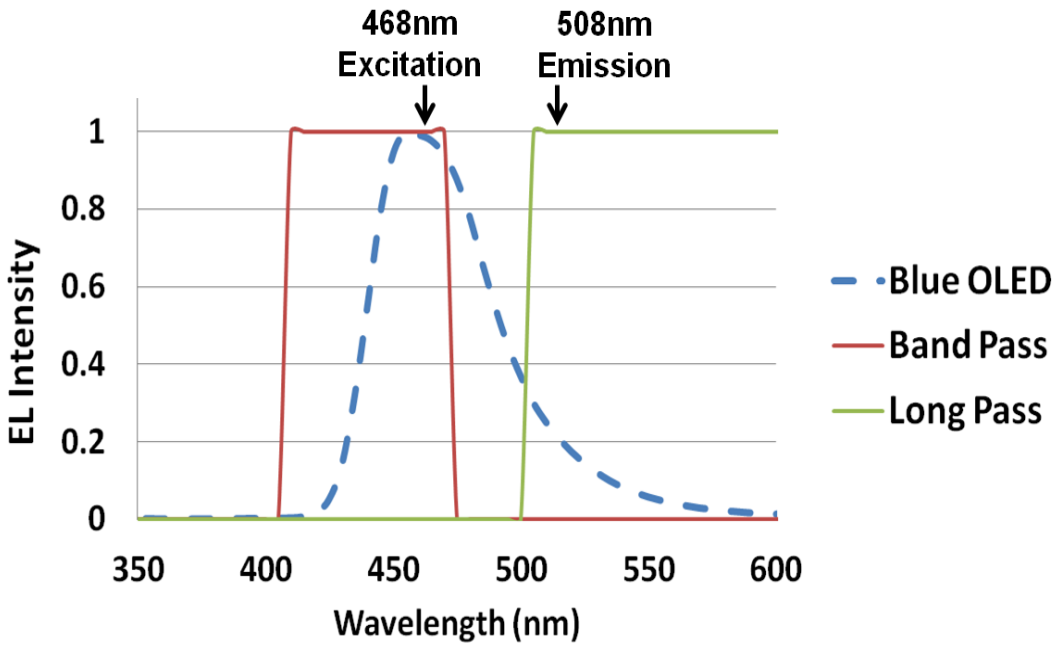

Figure 73. 455nm blue OLED Electroluminescence (EL) optical spectra taken using Ocean Optics HR4000CG spectrometer (YK Lee).

Unlike the predicted 100% or perfect attenuation though ideal orthogonally crossed polarizers, the maximum light attenuation through actual commercial linear polarizers is limited to approximately 10^4 (2014d). To emulate the performance of diagnostic laboratory instrumentation, which is designed to detect minute amounts of fluorescent material, light attenuation levels may instead need to approach 10^9 (Reichman 2000), which is 5 orders of magnitude more sensitive than what is possible using crossed linear polarizers. This indicates that high performance optical filters are required instead of the crossed linear polarizers to reduce the percentage of light from the source (blue

OLED) that reaches the photodetector for high sensitivity detection. Additionally, electroluminescence (EL) measurements for the 455 nm blue OLED emitter showed that the light intensity at 490 nm is still ~40% of the peak intensity (Figure 73).

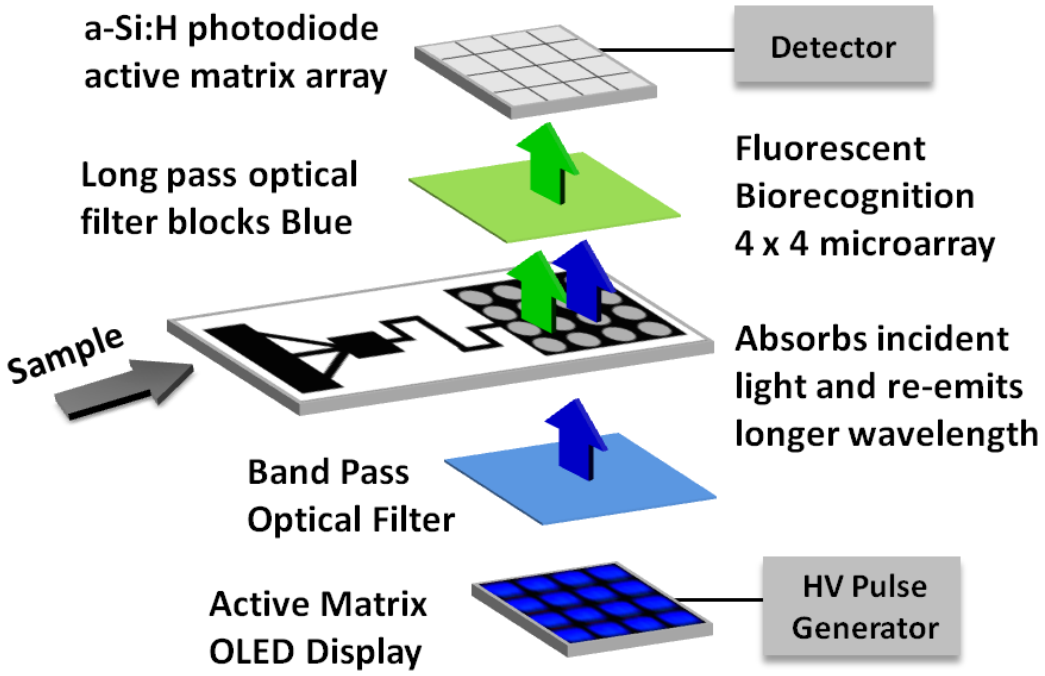

Figure 74. Exploded view of Lab-on-a-chip concept configuration using OLED display for optical excitation and a-Si:H PiN photodiode detector 4 x 4 active matrix array, in combination with optical filters for fluorescence analysis of multiple (16) biomarkers.

Assuming a typical fluorophore Stokes Shifts of ~40nm (excitation/emission delta wavelength), the observed wide emission spectrum for the blue OLED revealed that for high sensitivity applications, a long pass optical filter alone will be ineffective and must be combined with a band pass optical filter to block all of the emitted light from the blue OLED. Based on both of these observations, the crossed linear polarizers were replaced

with Chroma long pass and band pass optical filters, using the configuration illustrated in Figure 74.

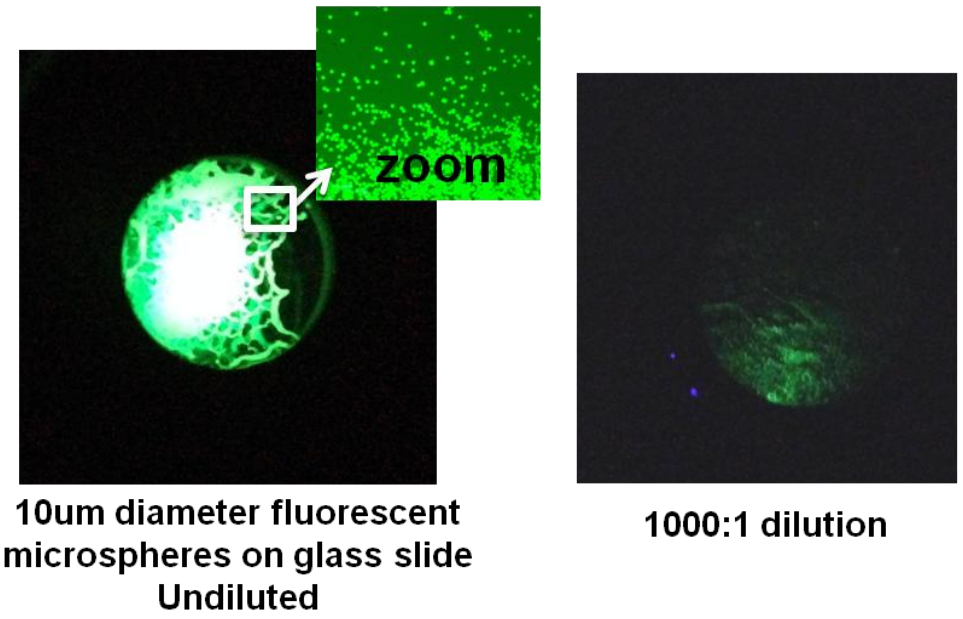

Figure 75. Optical photographs of fluorescing Thermo Scientific™ Fluoro-Max green 10um diameter microspheres immobilized on a glass slide, and placed between high performance Chroma band pass and long pass optical filters, and excited by a bright 0.3mW/mm2 2 x 2 mm, 455nm blue OLED emitter.

A 440nm/60nm band pass Chroma optical filter was positioned on top of the blue OLED emitter and Chroma long pass optical filter with a 505 nm cut-on was placed on top of the band pass optical filter. The long pass optical filter only transmits the emitted light from a green fluorophore and blocks light from the blue OLED. The band pass optical filter limits or narrows the spectrum of emitted light from the blue OLED to block transmission of the longer emitted wavelengths from the OLED by the long pass optical filter. Under controlled lighting conditions in a dark room, there was now zero (visual)

evidence of any light from the 0.3 mW/mm2 blue OLED exiting from the long pass optical filter using this new optical filter-based configuration.

To evaluate the ability to detect fluorescent biorecognition material, fluorescent green microspheres (468 nm excitation/508 nm emission) were immobilized on glass microscope slides, and then placed between the two optical filters. As shown in Figure 75, the observed (green) fluorescence from a drop of the undiluted microspheres (1% solids in an aqueous suspension) was extremely bright and bloomed the digital camera. Samples with the microspheres diluted in water 100:1 and 1000:1 were also visible.

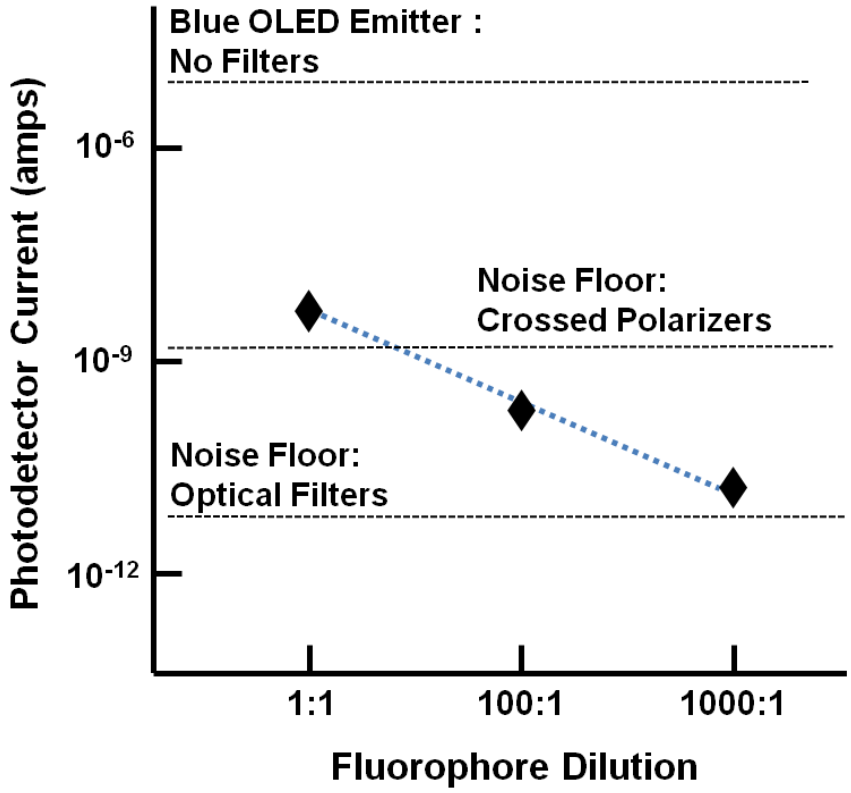

Figure 76. Photodetector current vs. concentration of fluorophore microspheres on glass slide using blue OLED with band pass and long pass optical filters, measured using UDT S380 Optometer and UDT 221 Silicon Sensor.

Optical measurements using a silicon photodetector (Figure 76) confirmed the ~10^4 of light attenuation for the crossed polarizer optics configuration. As shown in the same figure, switching to the optical filters improved OLED light attenuation by approximately three more orders of magnitude, providing a picoamp-level noise floor as opposed to the nanoamp noise floor for the crossed polarizers.

Of note, the detected light intensity for the undiluted (1:1) microspheres is only slightly above the noise floor for the crossed linear polarizers, while fluorophore dilutions down to 1000:1 can now be detected using the optical filters. Interestingly, the ability of the optical filter-based configuration to detect approximately 10^3 lower fluorophore concentrations also approximately scales with the 10^3 lower noise floor for the optical filter-based configuration. Guilbault reported that for these dilute fluorophore concentrations (Guilbault 1990), the earlier exponential relationship for emitted light intensity from the excited fluorophore reduces to the following approximation:

$$F = \varphi I_0(\varepsilon bc) \tag{35}$$

Hence, if φ, I_0, ε and b are kept constant, the relationship between the intensity of emitted light from the fluorophore is now linearly proportional to the fluorophore concentration (Guilbault 1990). However, as illustrated in Figure 77 plot, the observed mathematical relation for the light intensity as a function of fluorophore dilution more closely approximates a power law as opposed to the expected linear relationship for the two dilute 10 um green fluorophore microsphere solutions (100:1 and 1000:1). For a

linear relationship, the predicted sensor current should have been close to16 pA for the 1000:1 dilution, which would have been very close to the observed 15 pA optical filter noise floor. Instead, a current of 67 pA was measured for the 1000:1 dilution sample, which using the relationship from Figure 77, predicts that the sample could be further diluted down to approximately 10000:1, and still be detectable.

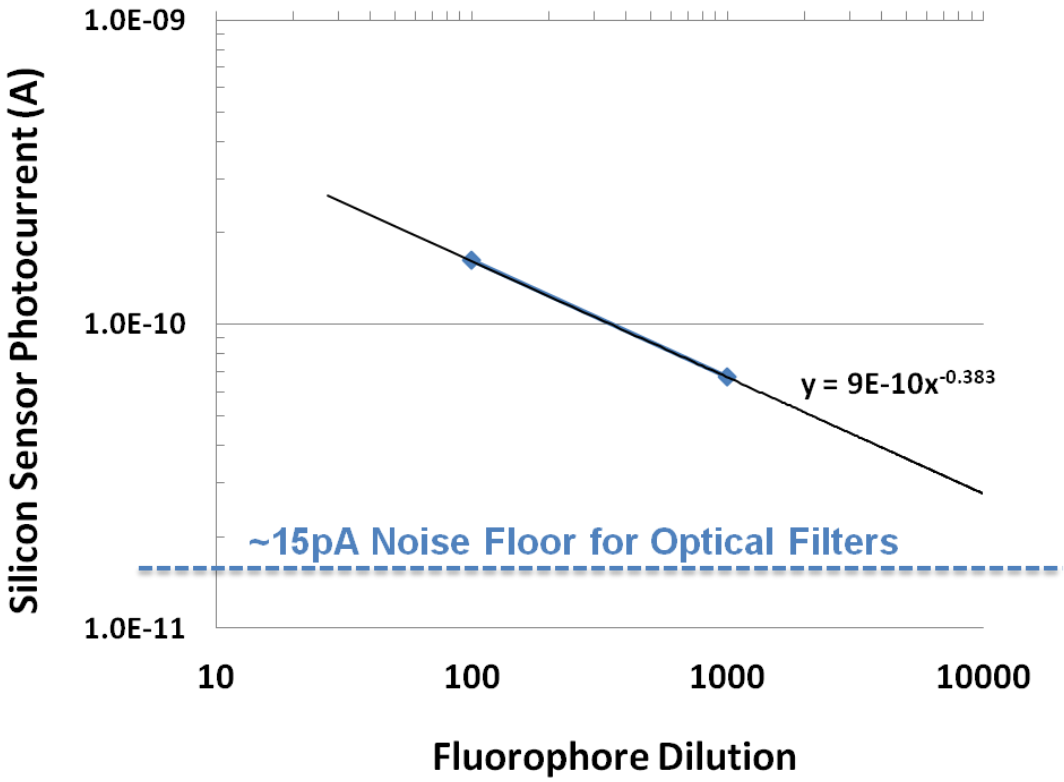

Figure 77. Modeling of Photodetector current vs. concentration of fluorophore microspheres on glass slide using blue OLED with band pass and long pass optical filters.

One explanation is that the linear relationship defined by Guilbault is still valid and the immobilization process reported above is ineffective at providing uniform microsphere dispersal. The belief is that during the drying portion of the immobilization

process, the 10 um fluorescent green microspheres are clumping. The result is a slightly higher localized concentration of fluorescent microspheres than predicted, which results in slightly more observed emitted light than expected or predicted for the 1000:1 dilution.

Given the poor predictive ability of the linear model, the measured data was then compared against predicted intensities using the original exponential model. An assumption was made that the undiluted 1:1 fluorophore measurements can be used to calculate an *ebc* factor in the exponential relationship for flurophore light intensity F as a function of the incident light intensity I_0 and conversion factor φ. Substituting the measured light intensity of the undiluted fluorophore and the incident light intensity I_0, combined with a conservative conversion efficiency of 0.3 for the fluorophore into the exponential relationship gives a calcuated *ebc* factor of 0.002384. As shown in the revised exponential relationship equation below, the calculated *ebc* factor divided by the fluorophore dilution d was then substituted for *ebc* in the original equation. This approach appears reasonable since dilution is one of the factors in the original *ebc* exponential relationship.

$$F = \varphi I_0(1 - e^{-0.002384/d}) \tag{36}$$

Using this revised exponential model, the fluorophore light intensity was plotted for all three of the dilutions (Figure 78), and compared to the actual measured intensity (photodiode current). Again, the actual (measured) fluorophore light intensity at 100:1 and 1000:1 is higher than predicted by the exponential model.

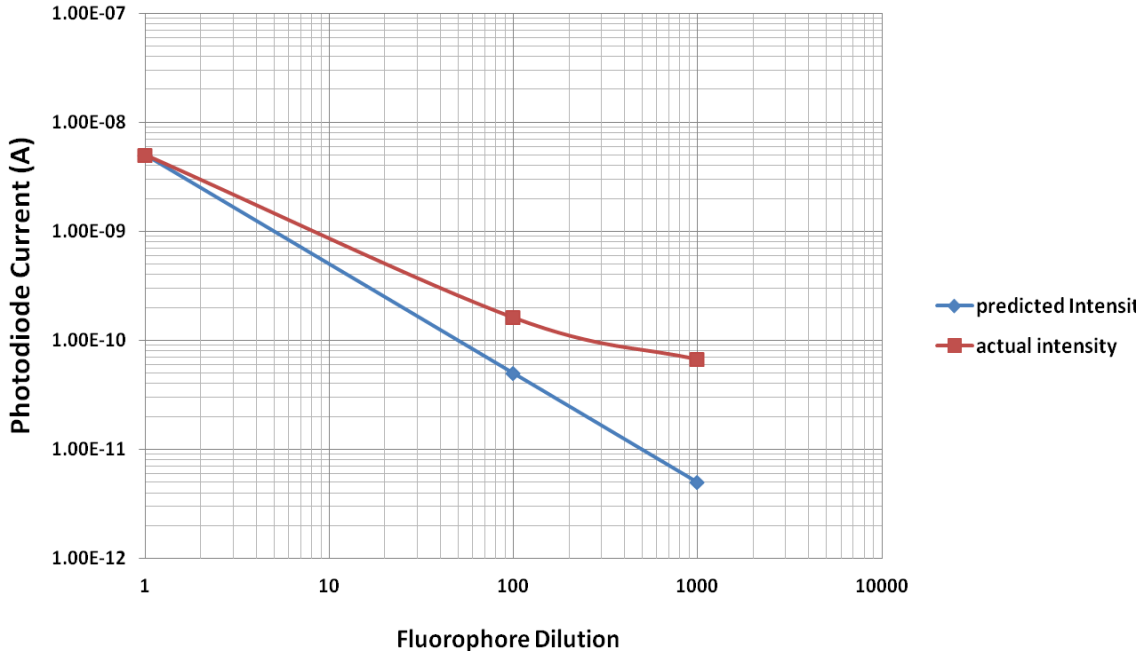

Figure 78. Calculated and actual photodetector current vs. concentration of fluorophore microspheres on glass slide using blue OLED with band pass and long pass optical filters using revised exponential model.

While the reported simple microsphere immobilization method appears valid to provide a reasonable or rough order of magnitude level sensitivity analysis, the method is ineffective at accurately determining a precise value for the sensor sensitivity. The assumption is that fluorophore tagged immune complexes generated using different concentrations (dilutions) of antibodies are required to accurately determine the actual sensor sensitivity.

Summary

This work explored initial viability of a new miniaturized fluorescence-based lab on a chip concept using OLED display and photodiode active matrix technology for point-of-use diagnosis of multiple disease or pathogen markers using a low cost

disposable configuration. Preliminary measurements indicated that the concept biosensor configuration requires optical filters to approach the sensitivity of laboratory fluorescence-based medical measurement instrumentation.

In addition to monitoring blood serum for multiple diseases, another potential commercial application is to determine if the local water is safe to drink. A low cost and point-of-use method to quickly detect multiple water borne pathogens can be of immediate use because "people suffering from waterborne illnesses occupy over half of all hospital beds globally (Peters 2014), and in addition to the lives lost, the total economic losses associated with inadequate clean water supply and sanitation is estimated at more than $250 billion annually (Colglazier 2013)."

CHAPTER 8

SUMMARY AND CONCLUSIONS

Facts are meaningless. You can use facts to prove anything that's even remotely true.

Homer Simpson

This study set out to explore how flexible electronics and display technology can be applied to develop new biomedical devices for medical, biological, and life science applications. New methods were developed to make digital x-ray detectors unbreakable, conformable, significantly larger, and more sensitive for medical and industrial imaging. The world's first 100% plastic flexible ISFET biosensor was developed for low-cost, disposable, shatter-resistant, and large-area applications, such as smart bandages to monitor human physiological conditions. Also explored was a new Optogenetics technique using flexible OLED display technology to selectively stimulate and/or silence neural activity, along with a new optical biosensor concept designed to detect multiple biomarkers at the point-of-use using OLED display and PiN photodiode active matrix arrays in a low cost compact disposable configuration.

Flexible Digital X-Ray Detectors: Using a new a-Si:H PiN photodiode process to personalize the superstructure of a flexible display active matrix array, a 7.9″ diagonal flexible digital x-ray was designed and developed. At the time of writing, this is the world's largest flexible digital x-ray detector. These new flexible digital x-ray detectors are designed to be more durable than conventional glass-substrate detectors for medical

and industrial imaging applications, as well as adding the ability to conform to the surface of whatever is being x-ray imaged.

Seamless Tiling of Flexible Active-Matrix Arrays for Very-Large-Area X-Ray Imagers: The flexible digital x-ray detector technology was then extended to demonstrate the viability of a new electronics assembly technique to seamlessly combine or tile individual flexible x-ray detectors into a single very large, ultimately human-sized, composite x-ray detector for new medical imaging applications such as single exposure, low-dose, full-body digital radiography or potentially for 3-D digital tomosynthesis imaging. Feasibility and preliminary imaging performance was demonstrated by tiling several 16 x 16 pixel resolution prototype flexible x-ray detector test structures. Optical losses under digital radiography conditions were measured by overlapping a plastic substrate flexible x-ray detector onto a commercial glass substrate digital x-ray imaging array. Approximately 5% signal loss was observed in the transparent plastic overlap region, and the seam-edge imaging artifact was demonstrated to be correctable using commercial gain calibration.

Improving Digital X-Ray Detector Sensitivity using Adaptive Imaging: A new approach to increase the sensitivity of digital x-ray detectors was then explored, which increases the detector signal-to-noise ratio by selectively disabling rows in an active matrix array that are not part of the region that needs to be imaged. The new method recognizes that in some medical imaging scenarios, what needs to be x-rayed may only cover a fraction or small portion of the entire x-ray detector array. However, the detected

signal during charge readout also includes undesired noise from TFTs in the unused portion of the x-ray detector array. It was shown that is possible to improve the detected image sensitivity by selectively disabling rows in the TFT active matrix array. The modeled detector-sensitivity improvement was shown to be a function of the percentage of the rows disabled.

Flexible ISFET Biosensors: The fabrication details and measured performance of the first 100% plastic, flexible, extended-gate, ISFET biosensor, manufactured using an IGZO TFT and an ITO sensing layer on a flexible PEN plastic substrate was explored. Flex ISFET drain current was shown to respond correctly to the pH buffer concentration with repeatable pH sensitivity observed over multiple cycles. The described new technique applies commercial flat panel display technology to make very large area active matrix TFT sensor arrays, which are more than 10X less expensive to manufacture than comparable CMOS-based ISFETs and provide a sensing area that is orders of magnitude larger than CMOS-based ISFETs. These new larger TFT display technology-based ISFETs also allow for much easier integration with area intensive chemical and biological recognition material as well as allow for a larger number of unique recognition sites to be incorporated on the individual ISFET sensor arrays for low cost multiple disease and pathogen detection.

Flexible Biophotonics: The initial viability of extending flexible OLED display technology to selectively stimulate and/or silence small groups of neurons for chronic optogenetic applications was demonstrated. Optical measurements from a 455 nm blue

flexible OLED test structure demonstrated the ability to emit 1 mW/mm^2 of instantaneous light intensity at 455 nm, which meets the minimum reported intensity to induce optical stimulation in genetically modified neural tissue. Biocompatibility was successfully demonstrated by the ability to grow human epithelial cells on the surface of a full TFT process-flow, plastic, flexible display substrate. Additionally, a new TFT active matrix array display (backplane) architecture was designed to support pulsed mode OLED operation.

Disposable Optical Biosensor for Multiple Biomarker Detection: This work explored viability of a new miniaturized fluorescence measurement-based concept using flexible OLED display and flexible a-Si:H PiN photodiode active matrix array technology for point-of-use or care diagnosis of multiple disease or pathogen markers in a low cost disposable configuration. Preliminary measurements indicated that the concept biosensor configuration requires optical filters to approach the sensitivity of laboratory fluorescence-based medical measurement instrumentation.

Selected Publications

In addition to the details presented in the previous chapters, the majority of the original contributions from this work were also captured in the following publications.

Smith, J., S. Shah, M. Goryll, J. Stowell, and D. Allee, “Flexible ISFET Biosensor Using IGZO Metal Oxide TFTs and an ITO Sensing Layer”. IEEE Sensors Journal, Volume: 14, Issue: 4, April 2014.

Smith, J, M Marrs, M Strnad, R Apte, J Bert, D Allee, N Colaneri, E Forsythe, and D Morton, “Flexible Digital x-ray technology for far-forward remote diagnostic and conformal x-ray imaging applications”. Proc. SPIE 8730, Flexible Electronics, 2013.

Smith, J., A. Couture, and D. Allee.. “Charge Emission Induced Transient Leakage Currents of a-Si:H and IGZO TFTs on Flexible Plastic Substrates”. Electronics Letters, Volume: 50, Issue: 2, January 16 2014.

Smith, J.T.; O'Brien, B.; Lee, Y.-K.; Bawolek, E.J.; Christen, J.B., "Application of Flexible OLED Display Technology for Electro-Optical Stimulation and/or Silencing of Neural Activity," IEEE Journal of Display Technology, vol.10, no.6, pp.514,520, June 2014.

Smith, J.T.; Couture, A.J.; Stowell, J.R.; Allee, D.R., “Optically Seamless Flexible Electronic Tiles for Ultra Large-Area Digital X-Ray Imaging”, IEEE Transactions on Components, Packaging and Manufacturing Technology, vol.4, no.6, pp.1109, June 2014.

Smith, J., Katchman, B., O’Brien, B, Lee, YK, Bawolek, E., Shah, S., and Blain Christen, J., “Disposable Point-of-Use Optical Biosensor for Multiple Biomarker Detection,” 2014 IEEE Biomedical Circuits and Systems Conference (BioCAS), Accepted for publication.

O'Brien, B, YK Lee, M Marrs, J Smith, M Strnad, E Forsythe, and D Morton, 2013. “14.7" Active Matrix PHOLED Displays on Temporary Bonded PEN Substrates with Low Temperature IGZO TFTs.” SID Symposium Digest of Technical Papers 70-2L:447.

Marrs, M, E Bawolek, B O'Brien, J Smith, M Strnad, and D Morton. 2013. “Flexible Amorphous Silicon PIN Diode Sensor Array Process Compatible with Indium Gallium Zinc Oxide Transistors.” SID Symposium Digest of Technical Papers, 44: 455-457.

Marrs, M. E. Bawolek, J. Smith, G. Raupp, D. Morton, “Flexible amorphous silicon PIN diode x-ray detectors. Proc. SPIE 8730, Flexible Electronics”, 87300C (May 29, 2013).

Recommendations for Future Work

For the flexible digital x-ray detectors described in Chapter 2, it would be interesting to develop a functional curved version of a digital x-ray detector and then investigate, using real-world examples, whether this new conformable version improves

x-ray imaging resolution. In addition to the looking for finer cracks in pipelines, one potential medical imaging application or test could be using a curved x-ray detector for cervical spine (c-spine) imaging. The curved x-ray imager could wrap around the back of the neck instead of having to lay flat. It would be interesting to find out whether using a curved detector, which can be positioned closer to the object being x-rayed, can detect more subtle injuries of the vertebrae and adjacent structures.

For the discussed flexible x-ray detector tiling concept, the next step would be to move beyond the small test structures used to demonstrate the viability of the concept and fabricate a functional, tiled, composite array with at least two—preferably more—overlapping flexible x-ray detector tiles to evaluate its medical imaging performance. With positive results, this could set the stage for building the first human-sized x-ray detector for low-dose, single-exposure x-ray imaging, or using the very large seamless x-ray imager for large-format industrial-imaging applications, such cargo container inspection.

For the adaptive x-ray imaging concept, an interim next step could be to design new external row-driver interface electronics that allows selected rows to be turned off (disabled) on an existing x-ray imager. While likely not a production configuration, this approach would allow the viability of the adaptive-imaging concept to detect lower-level signals to be evaluated using an actual x-ray imager, as opposed to the simple test structures used for this work.

One next step in the flexible ISFET biosensor development effort would be to functionalize a device with a bio-recognition material or a pH sensitive enzyme, such as glucose oxidase, to evaluate biosensing performance, with a focus on selectivity and

sensitivity. If the results are favorable, larger biosensing arrays with multianalyte recognition could be then designed, fabricated, and tested. Additionally, because results indicated that an ITO sensor electrode may be problematic for very high sensitivity applications, alternatives to the ITO sensor layer, such as Ta_2O_5 could be evaluated. The tradeoff is somewhat higher manufacturing cost from the one additional process layer.

As outlined at the end of the biophotonics chapter, future optogenetics of flex research could first verify whether the reported 1 mW/mm^2 of pulsed blue light from a simple OLED test structure can optically stimulate or excite neurons *in vitro* using neural tissue expressing ChR2. This would validate the viability of concept and set the stage for future chronic *in vivo* optogenetics research using animal models.

For the optical biosensor, results so far only demonstrate optoelectronic using a configuration that mimics the biology. A key next step would be to demonstrate actual biological functionality, with an emphasis on demonstrating optical biosensor sensitivity and selectivity to a major disease(s).

REFERENCES

17 December 2010. "Insights of the Decade." *Science* no. 330:1612.

2010. *Biophotonics (Biological and Medical Physics, Biomedical Engineering)*. Edited by Lorenzo Pavesi and Philippe M. Fauchet: Springer.

DRZ Screens 2013a. Available from http://www.mcio.com/Products/drz-screens.aspx.

DuPont Teijin Films Teonex® PEN Film for Flexible Displays and Electronics 2013b. Available from http://www2.dupont.com/Displays/en_US/products_services/films/PEN_film.html.

Frontiers | Emerging Technologies that will change the world 2013c. Available from http://www.frontiersin.org/news/communitynewsdetails.aspx?cid=177&cname=Emerging_Technologies_that_will_change_the_world.

2013. *Here's the flexible E Ink screen that could be in the 2014 Kindle* 2013d2013]. Available from http://reviews.cnet.com/8301-18438_7-57592886-82/heres-the-flexible-e-ink-screen-that-could-be-in-the-2014-kindle/.

Meet The Researchers: Aaron Couture 2013e. Available from http://ge.geglobalresearch.com/meettheresearchers/genius/2011/10/11.

Printed electronics sector takes hard look at the flexible future | Solid State Technology 2013f [cited 12/28. Available from http://electroiq.com/blog/2013/03/printed-electronics-sector-takes-hard-look-at-the-flexible-futur/.

Rogers Research Group - University of Illinois 2013g. Available from http://rogers.matse.illinois.edu/.

ASU center produces new largest color flex display 2014a. Available from https://asunews.asu.edu/20130716_oled.

ASU center, PARC produce world's largest flexible X-ray detector 2014b. Available from https://asunews.asu.edu/20130318_flexiblexraydetector.

OLED Mobile Phones Market Research and Analysis Report - DolceraWiki. DisplaySearch 2014c. Available from http://www.dolcera.com/wiki/index.php?title=OLED_Mobile_Phones_Market_Research_and_Analysis_Report.

2014d. "Visible Linear Polarizing Laminated Film | Edmund Optics."

Oct 2011. Global Health and Aging. World Health Organization, National Institute on Aging, US Dept. of Health and Human Services.

Abbazadeh, S, S Majid, N Allec, and K Karim. 2012. "Amorphous Selenium photodetector on a flexible substrate for indirect conversion medical imaging." *Proceedings of SPIE, Physics of Medical Imaging* no. 8313 (Medical Imaging 2012).

Allee, D, L Clark, R Shringarpure, S Venugopal, Z Li, and E Bawolek. 2008. Degradation Effects in a-Si:H Thin Film Transistors and Their Impact on Circuit Performance. Paper read at IEEE 46th, Annual International Reliability Physics Symposium.

Banerjee, Ansuman, Yun Shuai, Rahul Dixit, Ian Papautsky, and David Klotzkin. "Concentration dependence of fluorescence signal in a microfluidic fluorescence detector." *Journal of Luminescence* no. 130 (6):1095-1100. doi: 10.1016/j.jlumin.2010.02.002.

Berglund, C. Neil. 1996. "A unified yield model incorporating both defect and parametric effects." *Semiconductor Manufacturing, IEEE Transactions on* no. 9 (3):447-454. doi: 10.1109/66.536115.

Bergveld, P. 2003a. "Thirty years of ISFETOLOGY: What happened in the past 30 years and what may happen in the next 30 years." *Sensors and Actuators B: Chemical* no. 88 (1):1-20. doi: http://dx.doi.org/10.1016/S0925-4005(02)00301-5.

Bergveld, Piet. 2003b. ISFET, theory and practice. Paper read at IEEE Sensor Conference, Toronto.

Boudry, J. M., and L. E. Antonuk. 1994. "Current noise power spectra of amorphous silicon thin film transistors." *Journal of Applied Physics* no. 76 (4):2529-2534. doi: 10.1063/1.357614.

Brody, T. P., Luo Fang-Chen, Z. P. Szepesi, and D. H. Davies. 1975. "A 6 × 6-in 20-lpi electroluminescent display panel." *Electron Devices, IEEE Transactions on* no. 22 (9):739-748. doi: 10.1109/T-ED.1975.18214.

Brotherton, S.D. 2013. *Introduction to Thin Film Transistors*: Springer.

Bushberg, J, J. Seibert, E Leidholdt, and J. Boone. 2002. *The Essential Physics of Medical Imaging*. Philadelphia: Lippincott Williams & Wilkins.

Canfield, R. E., J. F. O'Connor, S. Birken, A. Krichevsky, and A. J. Wilcox. 1987. "Development of an assay for a biomarker of pregnancy and early fetal loss." *Environ Health Perspect* no. 74:57-66.

Chiang, Jung-Lung, Syun-Sheng Jhan, Shu-Chen Hsieh, and An-Li Huang. 2009. "Hydrogen ion sensors based on indium tin oxide thin film using radio frequency sputtering system." *Thin Solid Films* no. 517 (17):4805-4809. doi: http://dx.doi.org/10.1016/j.tsf.2009.03.050.

Colglazier, E. 2013. "Remarks on Global Water Security." *46th Session of the Erice International Seminars: Role of Science in the Third Millenium* (August 19).

Couture, A, D Albagli, G Possin, H Hudspeth, P Janiszewski, and M Zoeller. 2005. "Performance Tests on a-Si TFT Arrays for Flat Panel Digital X-Ray Detectors." *Proceedings of SPIE, Physics of Medical Imaging* no. 5745 (Medical Imaging 2005):243.

David Halliday, Robert Resnick, Jearl Walker. 2013. *Fundamentals of Physics Extended, 10th Edition*.

Degenaar, P, B McGovern, R Berlinguer-Palmini, N Vysokov, N Grossman, V Pohrer, E Drakakis, and M Neil. 2010. "Individually addressable optoelectronic arrays for optogenetic neural stimulation." *IEEE Biomedical Circuits and Systems Conference (BioCAS)*.

Deisseroth, K. 2010. "Controlling the Brain with Light." *Scientific American* no. 303:48-55.

Deisseroth, Karl. January 2011. "Optogenetics." *Nature Methods* no. 8 (1):26-29.

Derbyshire. *A thin, flexible and fully integrated biosensor for the detection of lactate in human sweat* 2013. Available from http://elsevier.conference-services.net/resources/247/2514/pdf/BITE2011_0381.pdf.

Dixit, R., Shen Li, M. Ratterman, I. Papautsky, and D. Klotzkin. 2013. "Simultaneous Single Detector Measurement of Multiple Fluorescent Sources." *Sensors Journal, IEEE* no. 13 (5):1965-1971. doi: 10.1109/JSEN.2013.2239285.

Dobbins, J. June 2009. "Tomosynthesis Imaging: At a translational crossroads." *Medical Physics, Am. Assoc. Phys. Med.* no. 35 (No. 6):1956.

Elwassif, M. M., Q. Kong, M. Vazquez, and M. Bikson. 2006. Bio-Heat Transfer Model of Deep Brain Stimulation Induced Temperature changes. Paper read at Engineering in Medicine and Biology Society, 2006. EMBS '06. 28th Annual International Conference of the IEEE, Aug. 30 2006-Sept. 3 2006.

Emmerich, P., A. Mika, and H. Schmitz. 2013. "Detection of Serotype-Specific Antibodies to the Four Dengue Viruses Using an Immune Complex Binding (ICB) ELISA." *PLoS Negl Trop Dis* no. 7 (12). doi: 10.1371/journal.pntd.0002580.

Estrela, P., S. Keighley, P. Li, and P. Migliorato. 2008. Application of thin film transistors to label-free electrical biosensors. Paper read at IEEE International Sym. on Industrial Electronics, at Cambridge.

Feili, D, M Schuettler, and T Stieglitz. 2004. "Flexible microelectrode arrays with integrated organic semiconductors." *9th Annual conference of the the International FES Society*.

Ferrari. 2007. *BioMEMS and Biomedical Nanotechnology - Volume IV: Biomolecular Sensing, Processing and Analysis*. Edited by Bashir. Vol. XXII: Springer.

Forrest, S., D. Bradley, and M. Thompson. 2003. Measuring the Efficiencies of Organic Light Emitting Devices. Advanced Materials.

Foutz, T, R Arlow, and C McIntyre. 2012. "Theoretical principles underlying optical stimulation of a channelphodopsin-2 positive pyramidal neuron." *J. Neurophysiol* no. 107:3235-3245.

George G. Malliaras, Daniel A. Bernards, and Róisín M. Owens. 2008. *Organic Semiconductors in Sensor Applications (Springer Series in Materials Science)*. Edited by Daniel A. Bernards Malliaras, M. Owens Róisín and G. George: Springer.

Georgiou, Pantelis, and Christofer Toumazou. 2009. "ISFET characteristics in CMOS and their application to weak inversion operation." *Sensors and Actuators B: Chemical* no. 143 (1):211-217. doi: http://dx.doi.org/10.1016/j.snb.2009.09.018.

Gonçalves, D., D. M. F. Prazeres, V. Chu, and J. P. Conde. 2008. "Detection of DNA and proteins using amorphous silicon ion-sensitive thin-film field effect transistors." *Biosensors and Bioelectronics* no. 24 (4):545-551. doi: http://dx.doi.org/10.1016/j.bios.2008.05.006.

Guilbault, George. 1990. *Practical Fluorescence, Second Edition*: CRC Press.

Han, X, and E Boyden. 2007. Multiple Color Optical Activation, Silencing, and Desynchronization of Neural Activity with Single Spike Temporal Resolution. *PLoS One*, March, 1.

Haq, J., S. Ageno, G. Raupp, B. Vogt, and D. Loy. 2010. "Temporary Bond Debond Process for Manufacture of Flexible Electronics: Impact of Adhesive and Carrier Properties on Performance." *Journal of Applied Physics* no. 108 (11):114917.

Hosono, Toshio Kamiya, Nomura Kenji, and Hideo. 2010. "Present status of amorphous In–Ga–Zn–O thin-film transistors." doi: doi:10.1088/1468-6996/11/4/044305.

Ito, Manabu, Christian Koch, Vlado Svrcek, Markus B. Schubert, and Jürgen H. Werner. 2001. "Silicon thin film solar cells deposited under 80°C." *Thin Solid Films* no. 383 (1–2):129-131. doi: http://dx.doi.org/10.1016/S0040-6090(00)01590-X.

Jamasb, S., S. Collins, and R. L. Smith. 1998. "A physical model for drift in pH ISFETs." *Sensors and Actuators B: Chemical* no. 49 (1):146-155. doi: 10.1016/S0925-4005(98)00040-9.

Jonsson, Orri. 2013. "QEX10-XP Feature Rich QE System | QEX10 Cell QE/IPCE/Spectral Response Measurement System | Quantum Efficiency Measurements | Products."

Kaftanoglu, K, S Venugopal, M Marrs, A Dey, E Bawolek, D Allee, and D Loy. June 2011. "Stability of IZO and a-Si:H TFTs Processed at Low Temperature (200C)." *Journal of Display Technology* no. 7 (No. 6):339.

Karim, K., G. Sanaie-Fard, T. Ottaviani, M. Izadi, and F. Taghibakhsh. January 2006. "Amplified Pixel Architectures in Amorphous Silicon Technology for Large Area Digital Imaging Applications." *Journal of the Korean Physical Society* no. 48:S85.

Kim, Dae-Hyeong, Nanshu Lu, Roozbeh Ghaffari, Yun-Soung Kim, Stephen P. Lee, Lizhi Xu, Jian Wu, Rak-Hwan Kim, Jizhou Song, Zhuangjian Liu, Jonathan Viventi, Bassel de Graff, Brian Elolampi, Moussa Mansour, Marvin J. Slepian, Sukwon Hwang, Joshua D. Moss, Sang-Min Won, Younggang Huang, Brian Litt, and John A. Rogers. 2011. "Materials for multifunctional balloon catheters with capabilities in cardiac electrophysiological mapping and ablation therapy." *Nat Mater* no. 10 (4):316-323. doi: http://www.nature.com/nmat/journal/v10/n4/abs/nmat2971.html#supplementary-information.

Kim, R, D Kim, J Xiao, B Kim, S Park, B Panilaitis, R Ghaffari, J Yao, M Li, Z Liu, V Malyarchuk, D Kim, A Le, R Nuzzo, D Kaplan, F Omenetto, Y Huang, Z Kang, and J Rogers. 2010. "Waterproof AlInGaP Optoelectronics on stretchable substrates with applications in biomedicine and robotics." *Nature Materials* no. 9:929-937.

Kim, T, J McCall, Y Jung, X Huang, E Siuada, Y Li, J Song, H Pao, R Kim, C Lu, S Lee, I Song, G Shin, R Al-Hasani, S Kim, M Tan, Y Huang, F Omenetto, J Rogers, and M Bruchas. 2013. "Injectable, Cellular Scale Optoelectronics with Applications for Wireless Optogenetics." *Science* no. 340:211-216.

Kim, T.-i., Jung, Y. H., Song, J., Kim, D., Li, Y., Kim, H.-s., Song, I.-S., Wierer, J. J., Pao, H. A., Huang, Y. and Rogers, J. A. 2012. "High-Efficiency, Microscale GaN Light-Emitting Diodes and Their Thermal Properties on Unusual Substrates." *Small* no. 8 (11):1643-1649. doi: 10.1002/smll.201200382.

Knight, S. L., R. P. Taylor, A. A. Polliack, and D. L. Bader. 2001. "Establishing predictive indicators for the status of loaded soft tissues." *J Appl Physiol (1985)* no. 90 (6):2231-7.

Lee, Chang-Soo, Sang Kim, and Moonil Kim. 2009. "Ion-Sensitive Field-Effect Transistor for Biological Sensing." *Sensors* no. 9 (9):7111-7131.

Lemmi, F, and R Street. 2000. "The Leakage Currents of Amorphous Silicon Thin-Film Transistors: Channel Charge Emission." *IEEE Transactions on Electron Devices* no. 47 (12):2399-2402.

Ligler, Frances S. 2008. "Perspective on Optical Biosensors and Integrated Sensor Systems." *Analytical Chemistry* no. 81 (2):519-526. doi: 10.1021/ac8016289.

Lujan, R, and R Street. May 2012. "Flexible X-Ray Detector Array Fabricated with Oxide Thin Film Transistors." *IEEE Electron Device Letters* no. 33 (No. 5):688.

Marrs, M. June 1, 2014.

Marrs, M, E Bawolek, B O'Brian, J Smith, M Strnad, and D Morton. 2013. Flexible Amorphous Silicon PIN Diode Sensor Array Process Compatible with Indium Gallium Zinc Oxide Transistors. Paper read at SID Symposium Digest of Technical Papers, 44: 455-457.

Marrs, M, E Bawolek, B O'Brien, J Smith, M Strnad, and D Morton. 2013. "Flexible Amorphous Silicon PIN Diode Sensor Array Process Compatible with Indium Gallium Zinc Oxide Transistors." *SID Symposium Digest of Technical Papers, 44: 455-457*.

Marrs, M, C Moyer, E Bawolek, R Cordova, J Trujillow, G Raupp, and B Vogt. Oct 2011. "Control of Threshold Voltage and Saturation Mobility Using Dual Active Layer Device Based on Amorphous Mixed Metal Oxide Semiconductor on Flexible Substrate." *IEEE Transactions on Electron Devices* no. 58 (No. 10).

Marrs, Michael, Edward Bawolek, Joseph T. Smith, Gregory B. Raupp, and David Morton. 2013. Flexible amorphous silicon PIN diode x-ray detectors.

Mattis, J., K. M. Tye, E. A. Ferenczi, C. Ramakrishnan, D. J. O'Shea, R. Prakash, L. A. Gunaydin, M. Hyun, L. E. Fenno, V. Gradinaru, O. Yizhar, and K. Deisseroth. 2012. "Principles for applying optogenetic tools derived from direct comparative analysis of microbial opsins." *Nat Methods* no. 9 (2):159-72. doi: 10.1038/nmeth.1808.

McCall, Jordan G., Tae-il Kim, Gunchul Shin, Xian Huang, Yei Hwan Jung, Ream Al-Hasani, Fiorenzo G. Omenetto, Michael R. Bruchas, and John A. Rogers. 2013. "Fabrication and application of flexible, multimodal light-emitting devices for wireless optogenetics." *Nat. Protocols* no. 8 (12):2413-2428. doi: 10.1038/nprot.2013.158
http://www.nature.com/nprot/journal/v8/n12/abs/nprot.2013.158.html#supplementary-information.

Merriman, B. 2012. "Progress in Ion Torrent semiconductor chip based sequencing." *Electrophoresis* no. 33:3397-3417.

Meyburg, S., M. Goryll, J. Moers, S. Ingelbrandt, S. Bocker-Meffert, H. Luth, and A. Offenhausser. 2006. "N-Channel field effect transistors with floating gates for extracellular recordings." *Biosensors and Bioelectronics* no. 21:1037-1044.

Migliorato, P, Pedro Estrela, S D Keighley, and P Li. 2008. "Label-Free Biosensor Micro-Arrays: A New Challenge for TFT Technology?" *15th International Workshop on Active-Matrix Flatpanel Displays and Devices (AM-FPD-08),*.

Moy, J. P. 1999. "Large area X-ray detectors based on amorphous silicon technology." *Thin Solid Films* no. 337 (1):213-221. doi: 10.1016/S0040-6090(98)01179-1.

Nakanotani, H, T Oyamada, Y Kawamura, H Sasabe, and C Adachi. 2005. "Injection and Transport of High Current Density over 1000 A/cm2 in Organic Light Emitting Diodes Under Pulsed Excitation." *Japanese Journal of Applied Physics* no. 44 (6A):3659.

Nakazato, Kazuo. 2009. "An Integrated ISFET Sensor Array." *Sensors* no. 9 (11):8831-8851.

Nathan, A., A. Ahnood, Matthew T. Cole, Lee Sungsik, Y. Suzuki, P. Hiralal, F. Bonaccorso, T. Hasan, L. Garcia-Gancedo, A. Dyadyusha, S. Haque, P. Andrew, S. Hofmann, J. Moultrie, Chu Daping, A. J. Flewitt, A. C. Ferrari, M. J. Kelly, J. Robertson, G. Amaratunga, and William I. Milne. 2012. "Flexible Electronics: The Next Ubiquitous Platform." *Proceedings of the IEEE* no. 100 (Special Centennial Issue):1486-1517. doi: 10.1109/JPROC.2012.2190168.

Nguyen, T. N. T., Y. G. Seol, and N. E. Lee. 2011. "Organic field-effect transistor with extended indium tin oxide gate structure for selective pH sensing." *Organic Electronics* no. 12 (11):1815-1821. doi: http://dx.doi.org/10.1016/j.orgel.2011.07.009.

O'Brien, B, YK Lee, M Marrs, J Smith, M Strnad, E Forsythe, and D Morton. 2013. "14.7" Active Matrix PHOLED Displays on Temporary Bonded PEN Substrates with Low Temperature IGZO TFTs." *SID Symposium Digest of Technical Papers* no. 70-2L:447.

Pais, A., A. Banerjee, D. Klotzkin, and I. Papautsky. 2008. "High-sensitivity, disposable lab-on-a-chip with thin-film organic electronics for fluorescence detection." *Lab Chip* no. 8 (5):794-800. doi: 10.1039/b715143h.

Peters, Rebecca. 2014. "Water rights." *The Daily Californian* (May 13, 2013).

Pinto, J., R. Branquinho, E. Alves, R. Martins, and E. Fortunato. 2012. "Extended -Gate ISFETs Based on Sputtered Amorphous Oxides." *IEEE Journal of Display Technology* no. 1551.

Platoni, K. 2010. New Light on the Brain. *Stanford Magazine*, November/December.

Powell, M. 1989. "The Physics of Amorphous-Silicon Thin-Film Transistors." *IEEE Transactions on Electron Devices* no. 36 (12):2753-2763.

Powell, M, J Hughes, N Bird, C Glasse, and T King. 1998. "Seamless Tiling of Amorphous Silicon Photodiode TFT Arrays for Very Large Area X-Ray Image Sensors." *IEEE Transactions on Medical Imaging* no. 17 (No. 6):1080.

Rahn, J, F Lemmi, P Lu, P Mei, R Apte, R Street, R Lujan, R Weisfield, and J Heanue. June 1999. "High Resolution x-ray imaging using amorphous silicon flat panel arrays." *IEEE Transactions on Nuclear Science* no. 46 (3):457.

Raupp, G, S O'Rourke, B O'Brien, S Ageno, D Loy, E Bawolek, D Allee, S Venugopal, J Kaminski, D Bottesch, J Dailey, K Long, M Marrs, N Munizza, H Haverin, and N Colaneri. 2007. "Low Temperature Amorphous Silicon Backplane technology development for Flexible display in a Manufacturing Pilot line environment." *JSID* no. 15 (7):445-454.

Raupp, G., S. O'Rourke, B. O'Brian, S. Ageno, D. Loy, E. Bawolek, D. Allee, S. Venugopal, J. Kaminski, D. Bottesch, J. Dailey, K. Long, M. Marrs, N. Munizza, H. Haverinen, and N. Colaneri. 2007. "Low Temperature Amorphous Silicon Backplane technology Development for Flexible Display in a Manufacturing Pilot Line Environment." *JSID* no. 15 (7):445-454.

Reichman, Jay. 2000. "Handbook of optical filters for fluorescence microscopy." *Chroma Technology Corporation*.

Rothberg, Jonathan M., Wolfgang Hinz, Todd M. Rearick, Jonathan Schultz, William Mileski, Mel Davey, John H. Leamon, Kim Johnson, Mark J. Milgrew, Matthew Edwards, Jeremy Hoon, Jan F. Simons, David Marran, Jason W. Myers, John F. Davidson, Annika Branting, John R. Nobile, Bernard P. Puc, David Light, Travis A. Clark, Martin Huber, Jeffrey T. Branciforte, Isaac B. Stoner, Simon E. Cawley, Michael Lyons, Yutao Fu, Nils Homer, Marina Sedova, Xin Miao, Brian Reed, Jeffrey Sabina, Erika Feierstein, Michelle Schorn, Mohammad Alanjary, Eileen Dimalanta, Devin Dressman, Rachel Kasinskas, Tanya Sokolsky, Jacqueline A. Fidanza, Eugeni Namsaraev, Kevin J. McKernan, Alan Williams, G. Thomas Roth, and James Bustillo. 2011. "An integrated semiconductor device enabling non-optical genome sequencing." *Nature* no. 475 (7356):348-352. doi: http://www.nature.com/nature/journal/v475/n7356/abs/nature10242.html#supplementary-information.

Rowlands. Flat Panel Detectors for Medical X-Ray: Physics and Technology. http://hepwww.rl.ac.uk/Vertex03/Talks/Row/Rolands.pdf.

Ryu, G., J. Huang, O. Hofmann, C. A. Walshe, J. Y. Sze, G. D. McClean, A. Mosley, S. J. Rattle, J. C. deMello, A. J. deMello, and D. D. Bradley. 2011. "Highly sensitive fluorescence detection system for microfluidic lab-on-a-chip." *Lab Chip* no. 11 (9):1664-70. doi: 10.1039/c0lc00586j.

Sarma, K R. 2003. "Active Matrix OLED Using 150C a-Si TFT Backplane Built on Flexible Plastic Substrate." *SPIE Symp. on Aerospace/Defense Sensing* no. 580:180.

Schoning, Michael J., and Arshak Poghossian. 2002. "Recent advances in biologically sensitive field-effect transistors (BioFETs)." *Analyst* no. 127 (9):1137-1151. doi: 10.1039/B204444G.

Schöning, Michael J, and Arshak Poghossian. 2006. "Bio FEDs (Field-Effect Devices): State-of-the-Art and New Directions." *Electroanalysis* no. 18 (19-20):1893-1900. doi: 10.1002/elan.200603609.

Schoonover, C, and A Rabinowitz. 2011. Control Desk for Neural Switchboard. *The New York Times*, May 16.

Smith, J, M Marrs, M Strnad, R Apte, J Bert, D Allee, N Colaneri, E Forsythe, and D Morton. 2013. "Flexible Digital x-ray technology for far-forward remote diagnostic and conformal x-ray imaging applications." *Proc. SPIE 8730, Flexible Electronics*.

Smith, J., S. Shah, M. Goryll, J. Stowell, and D. Allee. 2013. "Flexible ISFET Biosensor Using IGZO Metal Oxide TFTs and an ITO Sensing Layer." *Sensors Journal, IEEE* no. PP (99):1-1. doi: 10.1109/JSEN.2013.2295057.

Smith, J., and J. Stowell. 2012. Imaging System and Methods of Manufacturing and Using the Same. USA.

Smith, J. T., B. O. O'Brien, Yong-Kyun Lee, E. Bawolek, and J. Blain Christen. 2014. "Application of Flexible OLED Display Technology for Electro-Optical Stimulation and/or Silencing of Neural Activity." *Display Technology, Journal of* no. PP (99):1-1. doi: 10.1109/JDT.2014.2308436.

Street, R. 2009. "Thin Film Transistors." *Advanced Materials, Wiley Inter-Science* no. 21 (1-16).

Street, R, W Wong, T Ng, and R Lujan. 2009. Amorphous silicon thin film transistor image sensors. *Philosophical Magazine*, October Vol. Nos 28-30, 1-21, 2687-2697.

Street, R. 1999. "Large Area Image Sensor Arrays." In *Technology and applications of amorphous silicon*, 147-218. NY: Springer.

Street, R. A., and L. E. Antonuk. 1993. "Amorphous silicon arrays develop a medical image." *Circuits and Devices Magazine, IEEE* no. 9 (4):38-42. doi: 10.1109/101.250233.

Street, R. A., J. P. Lu, and S. R. Ready. 2003. "New materials and processes for flat panel X-ray detectors." *Circuits, Devices and Systems, IEE Proceedings* - no. 150 (4):250-7. doi: 10.1049/ip-cds:20030555.

Street, R.A. 2000. *Technology and Applications of Amorphous Silicon*: Springer.

Taghibakhsh, F. 2008. Active Pixel Sensor Architectures for High Resolution Large Area Digital Imaging. Waterloo, Ontario, Canada: A thesis presented to the University of Waterloo in fulfillment of the thesis requirement for the degree of Doctor of Philosophy in Electrical and Computer Engineering.

Taghibakhsh, F, and K Karim. 2008. "High Resolution Amplified Pixel Sensor Architectures for Large Area Digital Mamography Tomosynthesis." *Medical Imaging 2008: Physics of Medical Imaging, Proc. of SPIE* no. 6913 (69133R-1).

Thevenot, D. R., K. Toth, R. A. Durst, and G. S. Wilson. 2001. "Electrochemical biosensors: recommended definitions and classification." *Biosens Bioelectron* no. 16 (1-2):121-31.

Toumazou, Christofer, Leila M. Shepherd, Samuel C. Reed, Ginny I. Chen, Alpesh Patel, David M. Garner, Chan-Ju A. Wang, Chung-Pei Ou, Krishna Amin-Desai, Panteleimon Athanasiou, Hua Bai, Ines M. Q. Brizido, Benjamin Caldwell, Daniel Coomber-Alford, Pantelis Georgiou, Karen S. Jordan, John C. Joyce, Maurizio La Mura, Daniel Morley, Sreekala Sathyavruthan, Sara Temelso, Risha E. Thomas, and Linglan Zhang. 2013. "Simultaneous DNA amplification and detection using a pH-sensing semiconductor system." *Nat Meth* no. 10 (7):641-646. doi: 10.1038/nmeth.2520
http://www.nature.com/nmeth/journal/v10/n7/abs/nmeth.2520.html#supplementary-information.

Tredwell, T, J Chang, J Lai, G Heiler, and J Yorkson. June 22-28, 2009. Flat Panel Imaging Arrays for Digital Radiography. Paper read at Proc. of 2009 International Imager Sensor Workshop, at Bergen, Norway.

Venugopal, S, D Allee, M Quevedo-Lopez, B Gnade, E Forsythe, and D Morton. May 2010. "Flexible Electronics: What can it do? What should it do?" *Reliability Physics Symposium (IRPS)* no. 2010 IEEE International:644-649.

Viventi, Jonathan, Dae-Hyeong Kim, Leif Vigeland, Eric S. Frechette, Justin A. Blanco, Yun-Soung Kim, Andrew E. Avrin, Vineet R. Tiruvadi, Suk-Won Hwang, Ann C. Vanleer, Drausin F. Wulsin, Kathryn Davis, Casey E. Gelber, Larry Palmer, Jan Van der Spiegel, Jian Wu, Jianliang Xiao, Yonggang Huang, Diego Contreras, John A. Rogers, and Brian Litt. 2011. "Flexible, foldable, actively multiplexed, high-density electrode array for mapping brain activity in vivo." *Nat Neurosci* no. 14 (12):1599-1605. doi: http://www.nature.com/neuro/journal/v14/n12/abs/nn.2973.html#supplementary-information.

Wang, J, F Wagner, D Borton, J Zhang, I Ozden, R Burwell, A Nurmikko, R Wagenen, I Diester, and K Deisseroth. 2012. "Integrated Device for combined optical neuromodulation and electrical recording for chronic in vivo applications." *Journal of Neural Engineering* no. 9:1-14.

Weisfield, R, W Yao, T Speaker, K Zhou, R Colbeth, and C Proano. 2004. "Performance Analysis of 127 micron pixel large area TFT/photodiode array with boosted fill factor." *Proceedings of SPIE, Medical Imaging* no. 5368:338.

Weisfield, R. 1998. "Amorphous silicon TFT X-ray image sensors." *IEDM '98. Technical Digest., International*:21-24.

Weisfield, Richard L., and N. Robert Bennett. 2001. "Electronic noise analysis of a 127-μm pixel TFT/photodiode array." *Proc. SPIE Medical Imaging 2001: Physics of Medical Imaging* no. 4320:209-218.

Weisfield, Richard L., Mark A. Hartney, Roger Schneider, Koorosh Aflatooni, and Rene Lujan. 1999. High-performance amorphous silicon image sensor for x-ray diagnostic medical imaging applications.

Weisfield, Richard L., Mark A. Hartney, Robert A. Street, and Raj B. Apte. 1998. New amorphous-silicon image sensor for x-ray diagnostic medical imaging applications.

Wen-Yaw, Chung, Chang Kuo-Chung, Hong Da-You, Cheng Cheanyeh, F. Cruza, Liu Tai Sung, D. G. Pijanowska, M. Dawgul, W. Torbicz, Yang Chung-Huang, P. B. Grabiec, B. Jarosewicz, and Jung-Lung Chiang. 2008. An Electronic Tongue System Design Using Ion Sensitive Field Effect Transistors and Their Interfacing Circuit Techniques. Paper read at University/Government/Industry Micro/Nano Symposium, 2008. UGIM 2008. 17th Biennial, 13-16 July 2008.

Wilkinson, C, D Lidzey, L Palilis, R Fletcher, S Martin, X Wang, and D Bradley. 2001. "Enhanced performance of pulse driven small area polyfluorene light emitting diodes." *Applied Physics Letters* no. 79:171.

Wong, W, and A Salleo. 2009. *Flexible Electronics, Materials and Applications*. New York: Springer Science and Business Media.

Wong, W., T. Ng, S. Sambandan, and M. Chabinyc. Nov-Dec, 2011. "Materials, Processing, and Testing of Flexible Image Sensor Arrays." *Design & Test of Computers, IEEE* no. 28 (6):16-23.

Yeo, W. H., Y. S. Kim, J. Lee, A. Ameen, L. Shi, M. Li, S. Wang, R. Ma, S. H. Jin, Z. Kang, Y. Huang, and J. A. Rogers. 2013. "Multifunctional epidermal electronics printed directly onto the skin." *Adv Mater* no. 25 (20):2773-8. doi: 10.1002/adma.201204426.

Yin, L., J. Chou, W. Chung, T. Sun, and S. Hsiung. 2000. "Separate structure extended gate H+ -ion sensitive field effect transistor on a glass substrate." *Sensors and Actuators* no. 71:106-111.

Zelakiewicz, S., A. Couture, S. Bogdanovich, G. Possin, and D. Albagli. 2005. "Evolution of charge emission for amorphous silicon FETs exposed to radiation." *Nucl Instrum Methods Phys Res A* no. 546 (1-2):4-4. doi: 10.1016/j.nima.2005.03.052.

Zhang, F, L Wang, M Brauner, J Liewald, K Kay, N Watzke, P Wood, E Bamberg, G Nagel, A Gottschalk, and K Deisseroth. 2007. "Multimodal fast optical interrogation of neural circuitry." *Nature* no. 446:633.